西 安 交 通 大 学

系 （专业）0926 理科试验班（物理 H）
系 (专业) 主任 左兆宇
批 准 日 期 2020-11-11

毕业设计(论文)任务书

物理学院 学院 0926 理科试验班（物理 H） 专业 物理试验班 72 班 学生 宋昊天

毕业设计(论文)课题 极亮 X 射线源的星族合成研究

毕业设计(论文)工作自 2020 年 10 月 9 日起至 2021 年 6 月 23 日止

毕业设计(论文)进行地点：基础学科大楼

课题的背景、意义及培养目标

极亮 X 射线源是天体物理研究的热点。通过对极亮 X 射线源的星族合成研究，对了解超新星爆发机制，大质量单双星演化，极亮 X 射线源的诞生和演化等问题都有重要的意义。宋昊天同学通过这次的本科毕设，一方面将能提高其搜集、阅读外文科技文献的能力，另一方面通过对本课题的研究将能使其熟悉科研工作的方法，利于其未来的研究工作。在这个过程中，主要培养其科研的态度，培养其将理论知识用于实际的能力，培养其理论数据推演能力。

设计(论文)的原始数据与资料

此毕业设计主要进行观测资料整理和理论方面的调研及研究，研究资料主要来源于国际天文专业网站（如美国天体物理杂志等），可以通过国际互联网获得。后期的理论计算主要采用英国剑桥大学恒星组开发的恒星（双星）演化程序，也可以通过国际互联网获得。

课题的主要任务

本课题主要要求学生通过查阅相关书籍及外文文献，了解极亮 X 射线源相关课题的最新进展和新动向，通过观测资料的收集，理论模型的调研，进一步分析极亮 X 射线源的形成和演化等。主要研究超新星爆发机制、金属丰度、大质量恒星星风对诞生极亮 X 射线源的影响等。由此需要其寻找相关天体原始数据及熟悉相关专业软件的应用。在前期工作完成后，严格、准时按照学校对本科毕设的统一要求进行毕业论文的撰写和相应的答辩工作。

课题的基本要求(工程设计类题应有技术经济分析要求)

2020/11/25—2021/3/14：阅读相关文献和书籍，弄清课题相关的知识理论体系和前沿

2021/3/15—2021/4/5 ：开始撰写论文大纲和初稿，并积极准备中期答辩

2021/4/6—2021/4/30：反复修改论文，并进入数据分析处理阶段，以便最后定稿

2021/5/1—2021/5/25：最后修订论文，并准备和进行毕业答辩

完成任务后提交的书面材料要求(图纸规格、数量，论文字数，外文翻译字数等)

1、 书面材料装订成册的论文要求字数不少于 15，000 字

2、 附注参考文献不少于 20 个，其中英文参考文献不少于 10 个

3、 论文体系完整，结构合理，符合本科生的论文规范化要求

4、 资料详实，论据可靠，论证充分，外文文献翻译不少于 3，000 字

主要参考文献

1、Wolter, A. et al., 2018, ApJ, 863, 43

2、El Mellah, I. et al., 2019, A&A, 622, L3

3、Hurley J. R., Pols O. R., Tout C. A., 2000, MNRAS, 315, 543

4、Hurley J. R., Tout C. A., Pols O. R., 2002, MNRAS, 329, 897

指导教师：左兆宇

接受设计(论文)任务日期：2020-11-11

（注：由指导教师填写）　　学生签名：

西 安 交 通 大 学

毕业设计(论文)考核评议书

物理学院 学院 0926 理科试验班（物理 H） 专业 物理试验班 72 班

指导教师对学生 宋昊天 所完成的课题为 极亮 X 射线源的星族合成研究

的毕业设计(论文)进行的情况，完成的质量及评分的意见： 宋昊天同学主要研究了极亮 X 射线源的星族问题。论文主要介绍了极亮 X 射线源研究进展，并创新性的研究了风洛希瓣流吸积在极亮 X 射线源中的贡献，得到了一批有意义的结果。论文内容丰富，结构合理，逻辑清晰，是一篇优秀的本科毕业论文。

指导教师建议成绩： A+

指导教师 左兆宇

2021 年 6 月 21 日

毕业设计(论文)评审意见书

评审意见： 极亮 X 射线源是目前高能天体物理的热点。宋昊天同学以极亮 X 射线源为研究对象，考虑风洛希瓣流吸积机制，计算了脉冲极亮 X 射线源的星族问题；模拟了环状星系的光度函数问题，得到了有意义的结果。论文具有一定创新性，工作量大，论述清晰，是一篇优秀的本科毕业论文。

评阅教师建议成绩： A+

评阅人 钟渊 职称 副教授

2021 年 6 月 21 日

毕业设计(论文)答辩结果

物理学院 学院

0926 理科试验班（物理 H） 专业

毕业设计(论文)答辩组对学生 宋昊天 所完成的课题为 极亮 X 射线源的星族合成研究

的毕业设计(论文)经过答辩,其意见为 该本科毕设论文工作量大，高质量的完成了全部研究工作，研究方案合理，数据准确可靠，论文结构严谨，逻辑性强，文字流畅，图表规范，对结果的分析讨论准确且深入，对研究的问题有独特见解，成果突出；答辩中能够重点突出地阐述论文主要内容，回答问题准确流利。

并确定成绩为 A+

毕业设计(论文)答辩组负责人 高博

答辩组成员 张磊 冯雪红

陈海霞 郭永利

王喆 高博

2021 年 6 月 23 日

摘 要

对于 X 射线光度超过$10^{39} erg/s$的极亮 X 射线源，已有诸多天文观测样例，但是其形成机理以及星族构成仍未确定，近年来不同极亮 X 射线源的相关研究逐渐深入，现普遍认为其为双星系统中吸积物质所引发的强 X 射线辐射，洛希瓣吸积被认为是形成极亮 X 射线源的主要途径，后发现风吸积模型在特定条件下也能达到极亮 X 射线源的标准。

本文基于 EI Mellah 数值模拟洛希瓣式风吸积模型，运用星族合成方法，结合 BSE 和 MESA 恒星演化软件，在不同的风吸积效率和金属丰度条件下，给出了预测的伴星质量-轨道周期分布和有效温度-光学光度分布规律[1]。结合极亮源 NGC 7793 P13 和 PULX NGC 300 ULX-1 的观测数据，预测该源可以在洛希瓣星风吸积下形成极亮 X 射线源。其中长周期双星系统零龄主序星质量较小，而短周期系统主要是分布在由公共包层产生的 He 燃烧的伴星上。

本文还针对环状星系进行了极亮 X 射线源的光度函数模拟处理，其与数个环状星系的光度函数基本吻合。其中，黑洞洛希瓣系统仍占据主要部分，因为其高物质传输率和稳定的物质传输效率使其更易达到极亮 X 射线源的条件，中子星洛希瓣吸积在高光度时数目更多，是由于其高 beaming 而导致的各向异性辐射，洛希瓣式风吸积系统也在其中占据了一部分比例。大部分极亮 X 射线源的伴星以氢燃烧为主，并且处于演化的前期阶段。

关 键 词：X 射线双星；恒星演化；极亮源；中子星；黑洞

ABSTRACT

For ultra-luminous X-ray sources with X-ray luminosity exceeding 10^39 erg/s, there have been many astronomical observation examples, but the formation mechanism and population composition have not yet been determined. In recent years, related research on different ultra-luminous X-ray sources has gradually drawn attention. it is now generally believed that it is the strong X-ray radiation caused by the accretion in the binary star system. The Roche lobe accretion is considered to be the main way to form the extremely bright X-ray source. However, it was found that the wind accretion model also works under certain conditions which can reach the standard of extremely bright X-ray source.

In this paper, based on the EI Mellah numerical simulation of the Roche lobe wind accretion model, using the stellar synthesis method, combined with the BSE and MESA stellar evolution software, the predicted companion star masses-Orbital period distribution and effective temperature-Optical luminosity distribution are given under different wind accretion efficiencies and metallic abundance conditions,. Combining the observation data of the extremely bright source NGC 7793 P13 and PULX NGC 300 ULX-1, it is predicted that these sources can form an extremely bright X-ray source under the Roche lobe wind accretion. And the zero-age main sequence stars of the long-period binary system are relatively small, while the short-period systems are mainly distributed on the He burning companion stars produced by the common envelope.

In this paper, the X-ray luminosity function of the ultra-luminous X-ray sources is simulated for ring galaxies, which is basically consistent with the observation luminosity function of several ring galaxies. Among them, the black hole Roche lobe system still occupies the main part. Its high material transmission rate and stable material transmission efficiency make it easier to reach the conditions of ultra-luminous X-ray sources, and the neutron star Roche lobe accretion occupy at high luminosity. It is the anisotropic radiation caused by its high beaming, and the Roche lobe wind accretion system also contributes to a part of it. The companion stars of most ultra-luminous X-ray sources are dominated by hydrogen combustion and are in the early stages of evolution.

KEY WORDS: X-ray binaries; Stellar evolution; Ultraluminous X-ray sources; Neutron star; Black hole

目 录

1 绪论

1.1 星族合成方法概述

星族合成方法（Evolution Population Synthesis，EPS）是指利用现阶段已有的恒星演化模型，根据所掌握的基本恒星形成环境和初始质量函数（Initial Mass Function，IMF）等条件，对目标星族进行相关观测特征的拟合，比对的方法[2]。例如本文中目标星族为极亮 X 射线源（Ultra-luminous X-ray Source，ULX）[3]，所采用的观测特征量有轨道周期，伴星质量，光度函数等。本文采用了两种恒星演化软件分别进行星族合成模拟。

1.1.1 BSE

由剑桥大学的 J. Hurly 在 2002 年开发的双星模拟演化软件（Binary Stellar Evolution，BSE）[4,5]，主要针对星族合成方法，提供了一种在牺牲小部分的计算精度的情况下，计算速度更快，计算的范围更广，可以进行批量平行运算的恒星演化程序①。针对于单个恒星的演化[4]，他给出了具体的可能演化路径，如图 1-1。该程序计算精度相比于更精确的恒星演化程序（例如下小节介绍的 MESA）结果相差不会超过 5%，由此可见其精确性。恒星从零龄主序星（Zero Age Main Sequence，ZAMS）开始，经历主序阶段（Main Sequence），部分可能经历超巨星阶段，最后经过超新星爆发，根据恒星质量分别塌缩成白矮星（White Dwarf），中子星（Neutron Star，NS）以及黑洞（Black Hole，BH）。由于白矮星质量较小，很难形成高强度稳定吸积，所以不在本文的讨论范围之内。主要的吸积过程中的主星都是指黑洞以及中子星。此外，BSE 也描述了在恒星演化过程中，恒星内部核燃烧的机制，从 H 核燃烧再到 He 核燃烧，由于金属丰度的不同，恒星在不同核燃烧的阶段所处时间，演化状态也有很大差异，其对中子星风吸积模型的影响十分显著，这一部分在后续章节中也会进一步讨论。

针对恒星的双星演化，除了单星演化的所有内容外，包括物质传输，吸积盘的形成，公共包层演化，双星并合，超新星爆发和角动量损失等机制也被囊括在双星演化程序之中。本文也基本上采用双星演化的程序，并且根据观测结果适当调整理论模型，进一步完善了恒星演化的各个过程的研究。

但是，由于程序开发时间较早，部分模型现在已经有很多变更，也有了更为贴近真实恒星演化的拟合结果，所以我们针对多个可能影响极亮 X 射线源的过程给出了优化后的版本，具体改动囊括了风吸积模型，洛希瓣吸积模型以及公共包层演化等多个方面，会在后文中一一介绍。

① J. Hurly 的恒星演化程序在他的个人主页中提供了演化样板：http://astronomy.swin.edu.au/~jhurley/binary.html

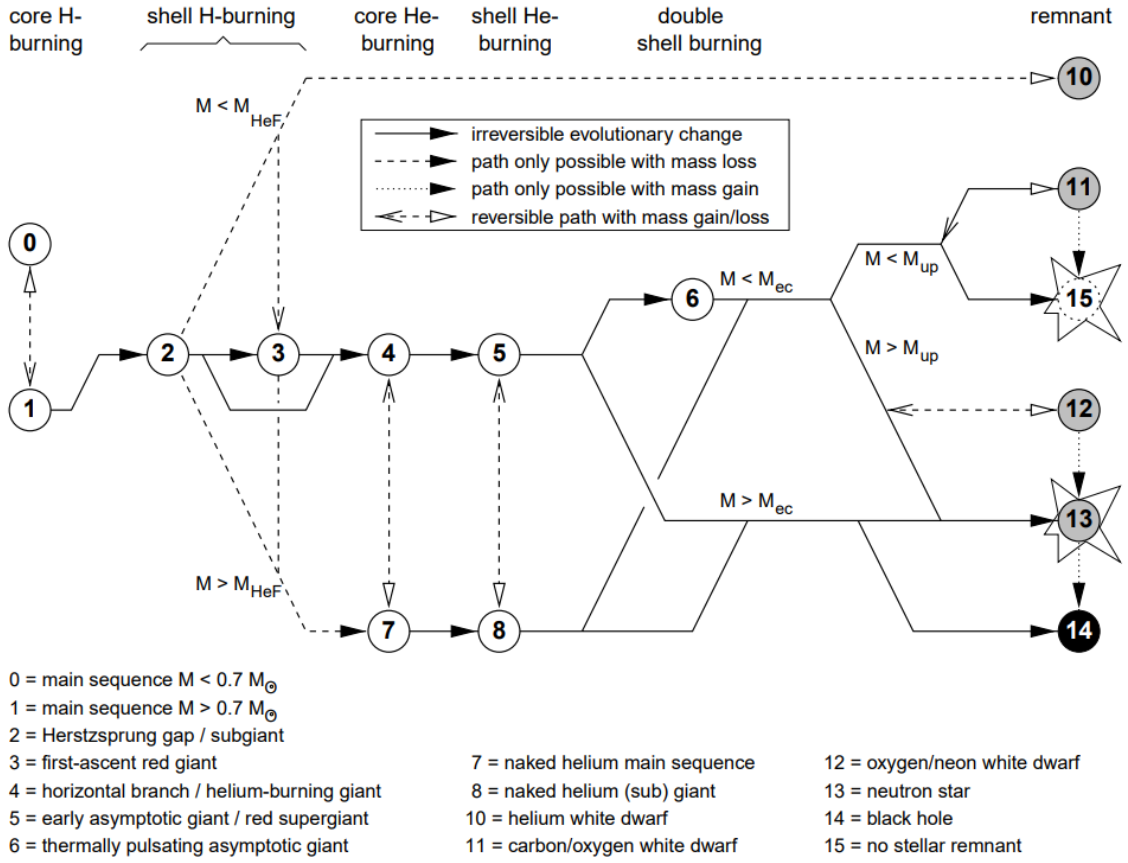

图 1-1 单个恒星可能的演化路径及不同的演化过程中相应的恒星状态[4]

1.1.2 MESA

开源软件 MESA（Modules for Experiments in Stellar Astrophysics）②是由多个理论和计算天体物理学家历时六年完成，并根据最新研究进展持续更新。MESA 作为一个相比于 BSE 更为详细的恒星演化工具，用更短的演化时间步长，更细致的恒星参量来进行恒星演化模拟。其中应用了诸多学科的前沿内容，例如：星震学，核物理，银河化学演化，星族合成。最新的观测结果也加入其中来给出关于星体演化对于金属丰度和年龄的依赖性。

1.2 ULX 的研究进展

极亮 X 射线源（Ultra-luminous X-ray Source，ULX）作为一种点状的，非核的 X 射线源，可以达到$10^{39} erg/s$ 的亮度，现在基本上认定为在双星系统中，形成了稳定的吸积过程，主星持续性大量的吸积伴星损失的物质导致 X 射线辐射。因为其 X 射线亮度超过了中子星甚至黑洞的爱丁顿亮度，所以近些年来引起了广泛关注[6]。针对极亮 X 射线源的环境的研究也在多方面展开，例如 X 射线光谱，在极亮 X 射线源中脉冲星频率的探测，伴星光学波段的观测，超爱丁顿吸积的机制，中等质量黑洞的研究。本文从星族合成的角度，以部分领域较为详实的数据为基础开展研究。

1.2.1 ULX 的观测统计

极亮 X 射线源的观测主要集中在 X 射线波段[7]，目前对于伴星的光学波段的探测还比较欠缺。

② 具体代码和更为详细的介绍可以参见 MESA 官网：http://mesa.sourceforge.net/，相关问题及各种最新模型可以参见 MESA 社区：http://cococubed.asu.edu/mesa_market/。

针对 X 射线源的观测统计已经较为成熟。首先，Swartz 在 2011 年针对距离观测 14.5Mpc 以内的 127 个极亮 X 射线源在 0.3-10.0keV 的光度进行了统计工作，从中可以看出极亮 X 射线源的数目和恒星生成率（Star Forming Rate，SFR）有正比关系[8]，此外，他还对 X 射线的光度函数进行了拟合，给出了最佳拟合公式$N(>L_{sp})=CL_X^{-\alpha}\exp(-L_X/L_c)$，在文中给出了相关拟合系数并画出了光度函数的图像。而后 Song Wang 根据 Chandra/ACIS 的最新观测结果给出了在不同观测的参数和模型的条件下，极亮 X 射线源现阶段的近邻星系的观测结果[9]。其中囊括了 343 个不同谱线的星系，并且根据恒星生成率进行了分类。针对不同的统计采用的模式进行了详细的讨论，并且给出了相应的光度函数以及大致的拟合结果。最近的关于极亮 X 射线源的统计研究是 Kovlakas 等人进行的[10]。他们采用了 Chandra Source Catalog 2.0 软件并且根据当前宇宙的最新编排的星系表来进行了统计分析工作，其中包括了 629 个极亮 X 射线源，309 个在 40Mpc 以内的星系，给出了部分上篇统计性文章中在统计时忽略的极亮 X 射线源，创新性的给出了平均星系内 ULX 的数目为$0.45^{+0.06}_{-0.09}\times\frac{\mathrm{SFR}}{M_\odot \mathrm{yr}^{-1}}+3.3^{+3.8}_{-3.2}\times\frac{M_\star}{M_\odot}$，以及对金属丰度[11]，伴星质量，星系类型等多个特征进行了详尽的统计分析，下文中还会针对此部分进行讨论说明。

1.2.2 针对 ULX 的理论研究

在极亮 X 射线源第一次被发现时，因为其高亮度，所以主星一直被认为是中等质量黑洞（Intermediate-mass Black Hole, IMBH），后来随着各向异性吸积模型的出现，极亮 X 射线源在未达到爱丁顿亮度的前提下也认为是可能存在的。随着脉冲信号在极亮 X 射线源被发现[12]，中子星极亮 X 射线源被证实，人们也开始将目光投入到中子星上。

针对于极亮 X 射线源的星族合成研究也有许多。在中子星极亮 X 射线源刚被发现时，Shao Yong 等就针对中子星各向异性的洛希瓣吸积模型进行了星族合成模拟[13]，采用 BSE 和 MESA 相结合的方式，给出了预测的伴星的轨道参量和光度函数，为未来的工作提供了参考。近些年来，Wiktorowicz 等人利用恒星演化软件 StarTrack[14]进行了较为详细的星族合成模拟工作[15,16]，依托于 Beaming 模型，针对洛希瓣吸积在 ULX 中的影响给出了相应的演化时间，典型演化路径，极亮 X 射线源星族构成，其还给出了当初始参量轨道周期和离心率等变化时，如果按照统计规律来选取，则这些结果相较于通常的固定做法的影响。Shao Yong 在 2019 年给出了针对中子星极亮 X 射线源的分析[17]。主要针对于刚经历完公共包层演化的 He 星与其他种类的星的差别，并且推测了具体的星族内所占比例以及相关的特征轨道参量。针对于风吸积的理论研究模型近日也有相关工作[18]，但是其采用的风吸积模型不同，我们会在下文中具体阐述。

2 研究模型

2.1 洛希瓣吸积

洛希瓣吸积在双星系统的物质传输之中一直占据着重要的地位，因为其形成了稳定的吸积盘，吸积效率相对于风吸积显著提高。吸积盘形成的研究已经较为成熟，即双星系统等势面从球形逐渐演化至相交，形成一个无穷大符号的形状，称为洛希瓣面，中间相交的点为第一拉格朗日点。其中我们采用了 Eggleton 在 1983 年提出的洛希瓣半径的计算公式[19]：

$$\frac{R_{L1}}{a}=\frac{0.49q^{\frac{2}{3}}}{0.6q^{\frac{2}{3}}+ln\left(1+q^{\frac{1}{3}}\right)} \tag{2-1}$$

其中q为双星质量比（Mass Ratio），a是双星之间的距离，R_{L1}为计算出的洛希瓣半径。洛希瓣提供了高效快速的物质传输渠道，现阶段该机制也被认为是大部分极亮 X 射线源产生的主要原因，在后文中我们会对此具体分析。

2.1.1 Beaming 模型

King 在 2008 年提出了 Beaming 模型来解释各向异性的洛希瓣吸积[20]，此模型“突破”了爱丁顿亮度，并且在众多星族合成的模拟中也进一步证实了该模型的可靠性。本小节就简要介绍一下 beaming 模型的原理以及涉及到的模型中具体的计算。

根据 Shakura 和 Syunyaev 在 1973 年提出的关于洛希瓣吸积的理论推导，

$$R_{\mathrm{sph}}=\frac{27}{4}\frac{\dot{M}}{\dot{M}_E}R_s \tag{2-2}$$

式中：R_{sph}——是当物质传输过程中首次达到爱丁顿亮度时的特征长度；$\dot{M}$——是物质传输率；$\dot{M}_E$——是爱丁顿亮度下的物质传输率；R_s——是 Schwarzschild 半径，可由$R_s=2GM_1/c^2=3\times10^5m_1$算得。

在物质传输过程中，在 Schwarzschild 半径内部和外部的物质传输机制差异很大。对于外部的区域，辐射仍旧按照爱丁顿光度计算，对于内部的，由于辐射压的作用，物质十分接近于爱丁顿亮度进行辐射，然而是以一种双锥形的几何特征进行辐射，这一区域释放 X 射线的能量用以下公式

$$L_{\mathrm{acc}}\simeq L_E\left[1+ln\left(\frac{\dot{M}}{\dot{M}_E}\right)\right] \tag{2-3}$$

式中：L_{acc}——实际释放的 X 射线光度。如果考虑到各向异性的辐射机制，那么在观测者看来，这种释放的能量是按双锥形辐射的，那么最终的亮度应该乘以一个 Beaming 系数b，其中$1/b>1$。应用到上式，则最终观测到的亮度为

$$L\simeq\frac{L_E}{b}\left[1+ln\left(\frac{\dot{M}}{\dot{M}_E}\right)\right] \tag{2-4}$$

针对 Beaming 系数的取值，在 Wiktorowicz 等人 2019 年的星族合成模拟中给出了较为普遍的定义[15]：$b=P_{\mathrm{obs}}(\theta)=1-cos\,\theta\,/2$。其中$\theta$是指辐射时所成的角度大小，角度越大，beaming 现象

越明显。当然这种几何上的定义很难在星族演化的过程中去衡量具体的系数大小。King 等人也在一直尝试着理论上的探索。King 和 Puchnarewicz 在 2002 年根据黑洞附近处的黑体辐射[21]，得出了一套比较普适性的几何上的 X 射线辐射公式（2-1）：

$$L_{\mathrm{sph}} = 2.3 \times 10^{44} T_{0.1\mathrm{keV}}^{-4} \frac{l^2}{pbr^2} \mathrm{ergs}^{-1} \tag{2-5}$$

式中：L_{sph}——基于各向同性辐射计算的观测者看到的黑体辐射亮度；l——是固有的 X 射线亮度和爱丁顿亮度L_E的比例；p——是根据各向同性辐射计算出的偏差（即观察者的视线方向与辐射平面的角度）；r——是以 Schwarzschild 半径为单位的黑体辐射半径$r = R/R_s$。

这个结果清晰的表明了，达到极亮 X 射线源的光度，至少需要满足下列条件中的一个：（1）$l > 1$，即针对于当前主星的质量，X 射线辐射为超爱丁顿吸积，这种吸积模式带来的超爱丁顿吸积很难维持较长时间，与观测到的稳定的极亮 X 射线源的观测特征不相符；（2）在小于 Schwarzschild 半径内部辐射，即$r < 1$；（3）$pb < 1$，即非均匀的辐射。

为了佐证以上猜测，需要相关的观测证据来说明。根据 Feng 和 Kaaret 在 2007 年对软 X 射线波段的黑体辐射的观测分析[22]，他们主要分析了 NGC 1313 X−2 的光谱特征，得出了软 X 射线和温度之间的关系$L_{\mathrm{soft}} \propto T^{-n}, n = -3.1 \pm 0.5$。这种幂次关系反应了一定光度和温度之间的关系。如果把这个关系带入到上式，则会得到 Beaming 系数和黑体辐射半径以及温度的关系$b \propto T^{4-n} r^{-2} \sim T^{0.9} r^{-2}$。后来，在 2008 年 Kajava 和 Poutanen 扩展了这个观测结果，分析比较了包括 NGC 1313 X−2 在内的九个极亮 X 射线源，给出了软 X 射线波段更为精准的幂次拟合公式，并且严格限制了 X 射线光度必须达到现用的标准$3 \times 10^{39}\, erg\, s^{-1}$。最后他们得出的最新的软 X 射线波段的观测结果为$L_{\mathrm{soft}} = 7 \times 10^{40} T_{0.1\mathrm{keV}}^{-4} \mathrm{ergs}^{-1}$。其中$T_{0.1keV}$为以 0.1KeV 为单位的温度。需要注意的是这种软 X 射线的关系可能在比较明亮的或者温度较低的区域会受到硬 X 射线不同程度的影响，但是整体上的趋势还是如此[23]。介于此，这种四次方的反比规律也表明了，在l和p确定的情况下，我们主要的影响因素只剩下 Beaming 系数和半径因素r。

针对半径因素r，根据式（2-5），我们可以近似得到$r = 27\dot{M}/4\dot{M}_E \tilde{r}$，其中$\tilde{r}$是黑体辐射半径与$R_{\mathrm{sph}}$的比例，通常情况下可以近似为 1。如果把软 X 射线的光度的观测拟合公式带入到理论计算中，我们可以大致得到：

$$b \sim \frac{73}{\dot{m}^2} x \tag{2-6}$$

式中：$x = l^2/p\tilde{r}^2$——各种对结果影响不大的常量，$\dot{m}$——物质传输率与爱丁顿物质传输率之比。这种基于极亮 X 射线源的天文软 X 射线观测给出的 Beaming 因子更具可信度，也为后续的理论模拟研究提供了非常有价值的帮助和指导作用。后续的星族合成模拟也都以此为基础进行 Beaming 模型的构建。此外，King 等人在后续也讨论了该模型在黑洞和中子星上的应用合理性与具有此特征的例子[20]，充分论证了 Beaming 模型对于极亮 X 射线源的贡献，我们针对洛希瓣吸积的 X 射线辐射研究，也基于他的工作，尽可能的给出真实的极亮 X 射线源的星族构成。

2.1.2 X 射线光度计算

针对洛希瓣吸积的光度，我们采用了现阶段较为通用的一些公式来计算具体的洛希瓣光度。首先，针对于爱丁顿亮度的计算有多种，我们采取如下的爱丁顿亮度进行计算：

$$L_{\mathrm{Edd}} = 2.6 \times 10^{38} \frac{1}{1+X} \frac{M_{\mathrm{acc}}}{M_{\odot}} \left[\frac{\mathrm{erg}}{s}\right] \tag{2-7}$$

式中：$M_{\rm acc}$——吸积天体的质量；$M_{\odot}$——太阳质量；X——在吸积物质中的氢丰度。传输物质所释放的 X 射线的能量，我们采取$\dot{m}_{\rm Edd}=L_{\rm Edd}/\eta c^2$来确定爱丁顿亮度下的物质损失率，其中我们采用的比较通用的物质能量转化率$\eta=0.1$，这种传化率可能会随着吸积机制改变，未来可以进一步调节来研究此效率对光度函数等方面的影响。

对于没有超过爱丁顿亮度的星，我们采用了$L_X=\eta\dot{M}c^2$来计算光度，采用同上文的η来衡量光度大小。这种源也是在其他星族模拟中普遍采用的方法[24]。对于超过爱丁顿亮度的源，因为这类源在极亮 X 射线源中占主导地位，所以我们采用了现在被证明造成极亮 X 射线源的主要原因的源来进行研究。总结起来如下式：

$$L_{app}=\begin{cases}\dfrac{L_{\rm Edd}}{b}\left(1+\ln\left(\dfrac{\dot{m}}{\dot{m}_{Edd}}\right)\right) & \dfrac{\dot{m}}{\dot{m}_{Edd}}>1\\ \dfrac{L_{\rm Edd}}{b}\dfrac{\dot{m}}{\dot{m}_{Edd}} & \dfrac{\dot{m}}{\dot{m}_{Edd}}\leqslant 1\end{cases} \tag{2-8}$$

其中L_{app} 为观测到的 X 射线亮度。

2.2 风吸积

2.2.1 传统 BHL 风吸积模型

传统的风吸积模型基本上都是采用邦迪（Bondi-Hoyle-Lyttleton，BHL）物质吸积模型[25]，这种各向同性的物质吸积也是导致之前各种星族合成模拟都未给出风吸积的理论预测的原因。该模型主要应用了理论上风吸积的动力学特征来给出物质传输率的近似，现简要介绍如下：

BHL 给出的邦迪吸积模式下物质传输率（mass accretion rate）可以由下式表示：

$$\dot{M}_{\rm BHL}=\pi R_{\rm BHL}^2 v_{\rm rel}\rho_{\bullet} \tag{2-9}$$

式中：R_{BHL}——修改后的吸积半径，由$R_{BHL}=2GM_{\bullet}/v_{\rm rel}^2$给出，该吸积半径相较于之前的半径在绝大多数情况下更大，也更符合吸积的实际情况；$v_{\rm rel}$——星风和致密天体的相对速度，可由速度合成公式$v_{\rm rel}=\sqrt{v_{\beta}^2+v_{\bullet}^2}$给出，其中$v_{\bullet}=v_{\rm orb}\,[q/(1+q)]$是指双星运动时的相对速度；$v_{\beta}$——在$\beta$模式下的风速，与此相关的调整可见后续的其他模型参量设置小节；$\rho_{\bullet}$——在主星附近的风吸积的密度，这种吸积密度是由根据各向同性的假设条件，在风传播的过程中，密度随距离逐渐降低得到的。这种假设显然不能符合正常的风吸积过程，尤其是在双星质量比相差大的时候，比如中子星与超巨星，黑洞与部分质量偏小的主序星。此外，这种模型也未考虑双星之间的轨道角动量造成的吸积物质各项异性的特征，这种各向异性也会导致最终 X 射线辐射时未球形辐射进而光度超过爱丁顿光度。

最终，邦迪吸积模式给出了物质传输效率（the fraction of wind captured）：

$$\mu_{\rm BHL}=\frac{(1+q)/q^3}{\eta(1-f\mathcal{E})^{\beta}[1+(\eta(1+q)(1-f\mathcal{E})^{\beta}/q)]^{\frac{3}{2}}} \tag{2-10}$$

式中：$\mu_{\rm BHL}$——$\dot{M}_{\rm BHL}/\dot{M}_{\star}$表示物质传输效率，即主星单位时间内吸积到的物质与伴星损失物质质量之比，一般情况下单位采用太阳质量每年；q——主星与伴星的质量比，本文中q均为此含义，后文不再赘述。$\mathcal{E}$——仅与q有关，具体是指洛希瓣半径与轨道半径之比，其中洛希瓣半径可以参见 Eggleton 的计算方法[19]；η——$v_{\infty}/v_{\rm orb}$，是终止速度（terminal speed）与轨道速度之比，用于衡量双星系统中的轨道参量。此模型在η较低的时候，恒星风和轨道角动量的相互作用不是很明显，吸积效率与实际情况相差不大。但是，如果恒星风速度较快，或者双星运动较慢，这种忽略致密星对

于星风的引力作用就会与实际情况产生巨大差别。

2.2.2 各向异性的风吸积模型

各向异性的星风模型的前身，首先是由 Mohamed, S 和 Podsiadlowski, P 在 2007 年提出的洛希瓣式风吸积模型（Wind Roche-lobe Overflow，WRLOF）[26]。他首次采用了数值模拟的方法，对 Mira-like 类型的恒星进行了数值模拟，并给出相应的结论[27]，这种物质传输模式会比传统的邦迪吸积效率提升 1.2 到 1.8 倍，这也是在研究中引起广泛关注的原因。进一步的，Abate 在 2013 年进一步的运用此模型来研究碳加速的低金属丰度的双星模型[28]，运用了星族合成的方法，进一步讨论了这种洛希瓣式风吸积模型对于各种情况下的对比，如图 2-1。由图可见，新型的洛希瓣式风吸积模型对风吸积效率有了明显提高。

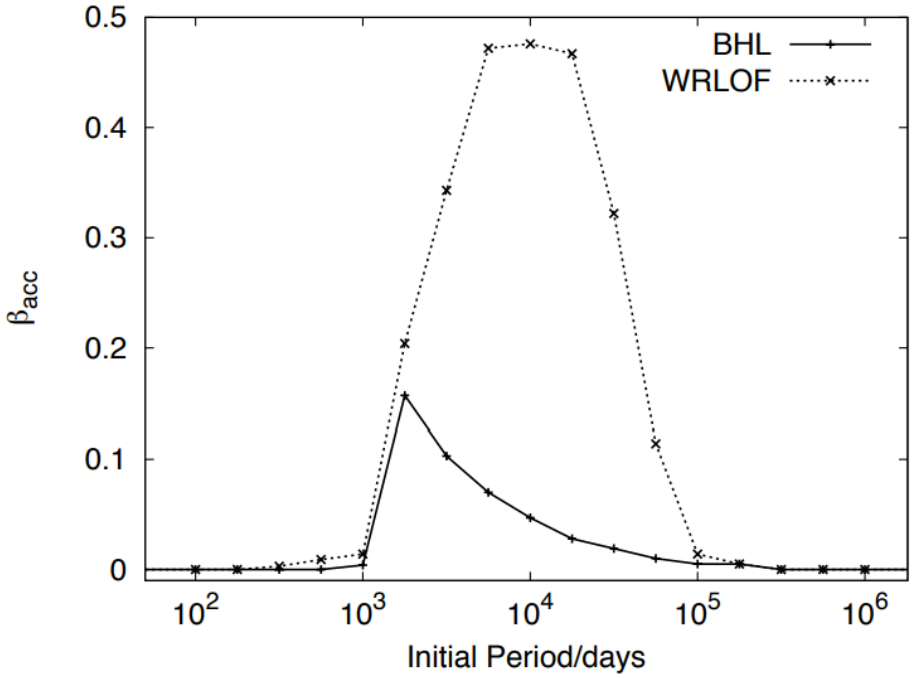

图 2-1 风吸积物质传输效率在不同初始轨道参量下的对比[28]，其中实线为传统的邦迪吸积模型，虚线为洛希瓣式风吸积模型，本图是针对于双星系统初始质量分别为 1.0 和 0.6 倍太阳质量下所做的对比。

首先，仅考虑在伴星与致密星的连线上，现假设星风受到辐射压的的作用加速，进而在逃逸半径R_d处达到了逃逸速度，假设逃逸半径远远大于伴星的半径，并且与洛希瓣半径相当或者略大，则根据 Höfner 的 2007 年研究成果[29]，可以得出与温度相关的逃逸半径表达式：

$$R_{\mathrm{d}} = \frac{1}{2} R_{\mathrm{don}} \left(\frac{T_{\mathrm{eff}}}{T_{\mathrm{cond}}} \right)^{\frac{4p}{2}} \tag{2-11}$$

式中：R_{don}——伴星的半径，T_{eff}——伴星的有效温度，T_{cond}——指星风的冷凝温度（condensation temperature）。p是一个拟合参量。由于研究是针对富含碳的星风，所以$T_{\mathrm{cond}} = 1500K$，$p = 1$。运用星族合成模拟的方法，将最终物质传输效率进行了二次多项式拟合，为后续的相关模拟工作提供了便捷，其拟合公式如下：

$$\mu_{\mathrm{acc}} = \min\left(\frac{25}{9} q^2 [c_1 x^2 + c_2 x + c_3], \mu_{\mathrm{acc},max} \right) \tag{2-12}$$

其中x是逃逸半径R_{d}与针对于伴星的洛希瓣半径之比，相应的拟合参量分别为$c_1 =$

$-0.284, c_2 = 0.918$,and$c_3 = -0.234$。此后，Wiktorowicz 在 2021 年针对于红超巨星进行了星族合成的计算[18]，并且提出红超巨星应该在极亮 X 射线源数目中占主导，并且在所有的极亮 X 射线源中，洛希瓣式风吸积模式占据绝大部分，最高可以达到 94%。然而，此结果与前面所做的绝大多数针对于极亮 X 射线源的模拟结果不符合，具体情况我们在后续章节会讨论。

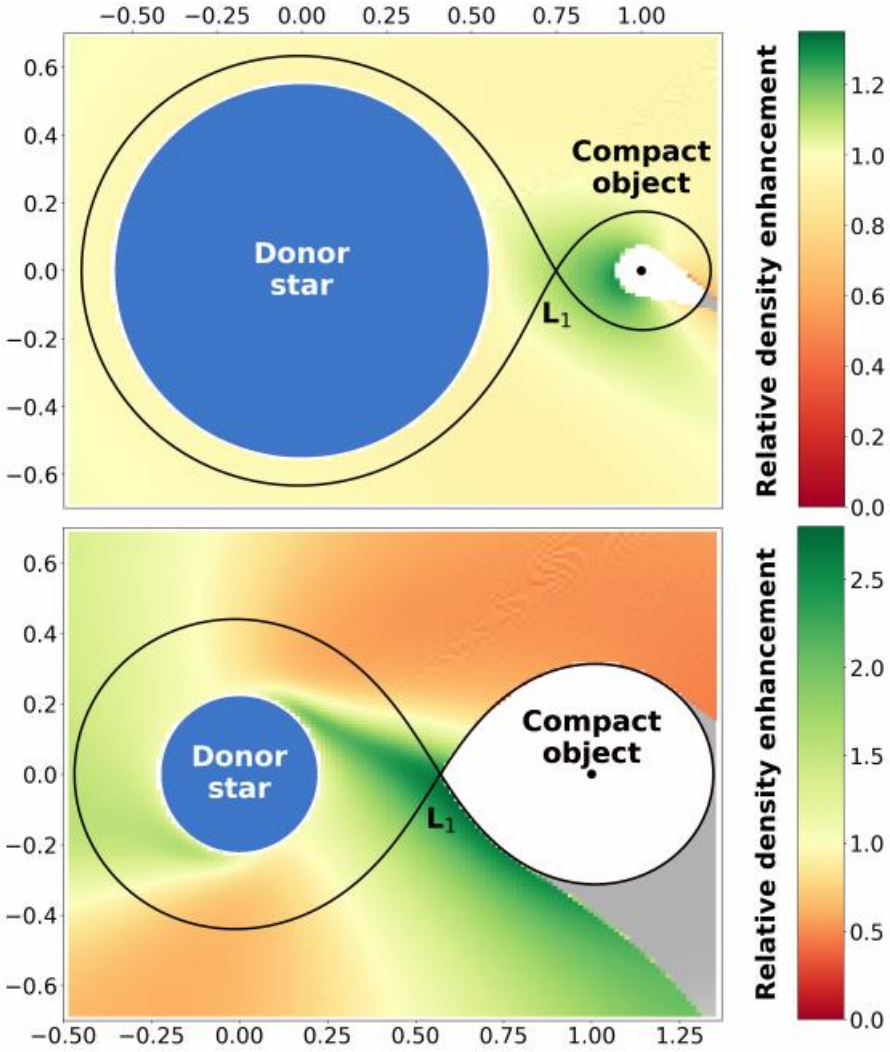

图 2-2 在轨道平面上的切面[30]。其中黑实线为洛希瓣的轮廓 ，中间交点为第一拉格朗日点。图中颜色表示的是星风密度与各向同性的星风密度之比。其中各向同性的星风密度随距离衰减，在同一距离上的积分与此模型计算的星风密度始终保持相等。上图为代表性的以中子星为主星的双星系统 Vela X-1（也可表示 P13）物质传输过程，下图为以黑洞为主星的 M101 双星系统示例。白色区域为风吸积物质的捕获区域，即速度小于该星的逃逸速度，由R_d计算可得。灰色区域为星风不能到达的区域。

上述所说的针对洛希瓣式风吸积模型的模拟基本上都局限于单一的双星模型，比如 Abate（2013 年）的工作只针对于碳占主导的伴星，这也就意味着伴星质量不能超过 8 倍太阳质量，对于型组合成模拟的情况，也很难给出风吸积模型的全貌，仅能分析局部特征。此外，由于技术和时间的限制，他们的数值模拟结果精度并不高，部分模型还是建立在经典的假设下完成的，这就导致了最终结果相较于传统的邦迪吸积模型提升并不大。

直到 2021 年，I. El Mellah 针对于极亮 X 射线源的研究给出了洛希瓣式风吸积的模拟结果，如图 2-2 所示。其中上图给出了典型中子星的模拟结果，下图给出了典型黑洞的模拟结果。由图可知，在黑洞（或者质量比更大）的情况下，物质传输效率的提升相较于传统的各向同性吸积提升更为明

显。甚至达到了两倍多，比之前的模拟计算更为显著，也为极亮 X 射线源的洛希瓣式风吸积模型提供了充实的证据。

不仅如此，I. El Mellah 还提供了不同参量空间下的物质传输效率，如图 2-3 所示。其中恒星占有率（filling factor）为伴星半径与洛希瓣半径之比，这是决定双星轨道的主要参量，速率比（Speed ratio）是终止速率和轨道速率之比，此参量衡量了星风的相关速率参量，为数值模拟计算的基础。

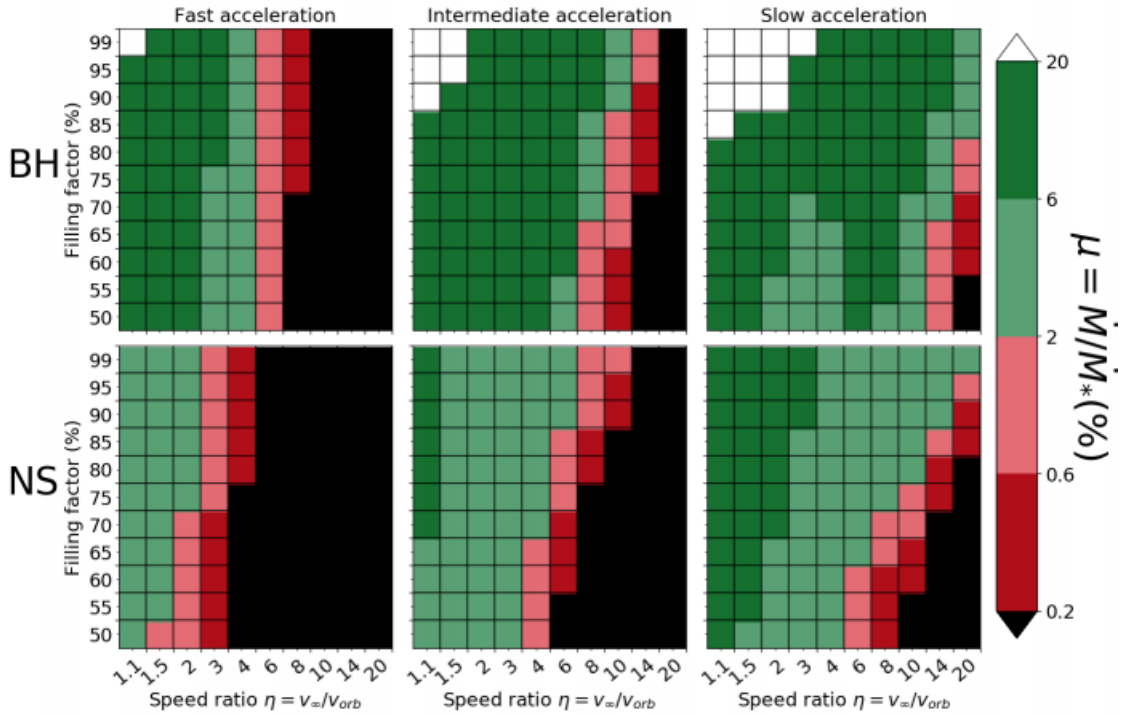

图 2-3 数值模拟结果展示[1]。图中颜色是根据物质传输效率 μ 的对数分布，其中横坐标为速率比，为终止速率和轨道速率之比；纵坐标是恒星占有率，为伴星半径与洛希瓣半径之比。第一行为黑洞为致密天体的双星系统的模拟结果；第二行为中子星为致密天体的双星系统的模拟结果。三列从左到右分别是 $\beta = 1,2,3$ 的数值模拟结果，其中 β 是风吸积速率的指数因子。

此模拟计算结果还给出了不同β对于风吸积的影响，我们也针对不同的风吸积效率进行了模拟计算。其提出的理论计算模型相较于之前的参量空间更广，星风吸积过程计算更为细致。针对于更广泛的极亮 X 射线源的星族合成有很强的借鉴作用。此模型相较于传统的邦迪吸积，在部分情况下，吸积效率提高了一个量级，这也为极亮 X 射线源的主星在风吸积的 X 射线辐射中提供了充足的“燃料”。

我们在速率较快的风吸积中采用了各项异性的洛希瓣式风吸积模型，针对于速率较慢的风吸积情形，相应的模拟计算不是很详细，以往的邦迪吸积与实际情况在此条件下相差不大，所以继续沿用了邦迪吸积模型。由于其对于风吸积的模拟计算只考虑了典型的中子星和黑洞系统（双星质量比分别为 2 和 15），针对于星族合成模拟中存在不同质量比的问题，我们采取了 El Mellah 的建议对中间区域进行线性插值计算，最终的风吸积效率由两种模拟结果共同决定。

2.3 恒星演化参量

2.3.1 初始质量函数

恒星演化的初始质量函数（Initial Mass Function，IMF）是指在零龄主序星时或者恒星诞生时，恒星的质量的概率分布。这种概率分布针对于大量的观测统计研究，现阶段的研究已经较为成熟，

我们此处采用了经典的 Kroupa 等人提出的初始质量函数用于我们星族合成的计算之中[31]。总体上是采用初始质量为 2 倍到 150 倍太阳质量，其中概率密度$\xi(m)$为幂指数分布：

$$\xi(m) \propto m^{-\alpha} \tag{2-13}$$

上式中α为系数，具体系数为

$$\alpha(m) = \begin{cases} +0.3 \pm 0.7 & 0.01 \leqslant m < 0.08 \\ +1.3 \pm 0.5 & 0.08 \leqslant m < 0.50 \\ +2.3 \pm 0.3 & 0.50 \leqslant m < 1.00 \\ +2.3 \pm 0.7 & 1.00 \leqslant m \end{cases} \tag{2-14}$$

上式中系数经过归一化处理后即为我们采用的初始质量函数，也就是得到不同质量的概率分布。虽然不同初始质量函数有部分差异，但是最终差别不是很大，因为我们的研究主要集中在高质量的初始质量函数上，不同函数在高质量端概率都很小，分布差异并不大。

2.3.2 风吸积指数β_{wind}

我们在计算中采用的风吸积指数β_{wind}是参照于 Lamers 在 1995 年基于被吸积天体的光谱类型得出的[32]，在双星演化中具有普适价值。针对于高质量的主序星，本文采用$\beta_{wind} = 7$，对于低质量的$\beta_{wind} = 0.5$，并使用线性插值的方法针对中等质量恒星进行拟合处理。富含氦的超巨星同样采用高质量恒星$\beta_{wind} = 7$，低质量恒星$\beta_{wind} = 0.13$，并在中间部分插值。富含氢的伴星一般都是速率较低的风吸积，所以采用$\beta_{wind} = 0.125$。

2.4 星族数目计算

2.4.1 恒星生成率

恒星生成率（Star Forming Rate，SFR）是指单位时间内零龄主序星生成的质量，其中可以按照单星和双星进行分解：

$$S_b \int_{M_{\text{low}}}^{M_{\text{up}}} m_1 \epsilon(m_1) dm_1 + S_b \int_{M_{\text{low}}}^{M_{\text{up}}} \epsilon(m_1) m_1 \bar{q} dm_1 + S_s \int_{M_{\text{low}}}^{M_{\text{up}}} m\epsilon(m) dm = SFR \tag{2-15}$$

式中：S_b——双星的恒星生成率；S_s——单星的恒星生成率；M_{low}和M_{up}——恒星生成的质量下限和质量上限。因为很多情况下较小质量的恒星很难进行全面的观测统计，所以恒星生成率内部不包括他们，此外，对于质量较大的恒星，根据初始质量函数计算的生成概率极小，这样统计和模拟计算上质量取更高上限也没有必要。q为双星质量比，在本模型中，我们采用了根据质量的平均分布，因为我们考虑的是极亮 X 射线源，小质量天体不足以维持高强度的物质传输。所以大质量物质的吸积模型是我们主要考察对象，将质量大于一倍太阳质量的初始质量函数带入，可简化为：

$$SFR = (S_b(1 + \bar{q}) + S_s) a \frac{M_{\text{low}}^{2-\alpha}}{\alpha - 2} \tag{2-16}$$

式中：a——归一化常量，可由初始质量函数算得。

2.4.2 星系预测数目计算

根据 Hurly 提出的星族合成计算公式[5]，最终特定演化状态下的数目δN为：

$$\delta N = S_b M_1 \epsilon(m_1) \delta \ln M_1 k_q \delta q \dot{k}_a \delta \ln a \delta T \tag{2-17}$$

式中：$k_q \delta q$——双星质量比所贡献的概率比重，如果我们采用均匀分布来表示双星质量比，则$k_q =$

$1/N_q$，其中N_q是指模拟计算中所取质量比的数目，$\dot{k}_a \delta \ln\ a$同理，只不过公认的使用$\ln\ a$为平均分布来进行计算。S_b是指上文提到的双星的恒星生成率，δT是指星族合成模拟中处于极亮 X 射线源的时间。

针对于中子星 ULX 的研究，我们需要探究不同的风吸积模型，金属丰度对结果产生的影响，先采用 BSE 计算不同金属丰度下中子星的诞生概率，而后选择不同的初始伴星质量，金属丰度，和轨道周期运用 MESA 进行细致的双星演化过程。最终得到的结果分别乘以 BSE 算得的不同系统的诞生概率，再乘以恒星生成率，即最终的星族合成结果，可以预测不同轨道参量下的双星系统的星族分布，具体讨论见下一节。

针对于环形星系的极亮 X 射线源的星族分析，我们在中子星为主星的系统中采取同上文中的方法，因为对于黑洞的模拟 MESA 相关的研究相较来说不是很成熟，所以我们继续沿用了 BSE 的程序模拟结果并给出相应分布和数目统计。

3 中子星 ULX 的研究

3.1 中子星 ULX 观测样例

3.1.1 NGC 7793 P13

NGC 7793 P13 最先被爱因斯坦卫星观测到，判断为星系 NGC 7793 极亮 X 射线源[33]，其高亮度的 X 射线辐射引起了广泛关注。而后，ROSAT 在 0.3-10keV 波段观测了此源，并给出亮度修正为大约$3.5 \times 10^{39}\mathrm{erg/s}$。进一步的 Chandra 卫星证实了这是一个带有致密星体绕转双星系统，并且给出了伴星的相关观测数据，推测其为 B9Ia 光谱型的伴星，并且预测其质量在 18~23 倍太阳质量之间；根据 HeII 辐射的径向速度方法，预测其轨道周期为 64 天。然而，致密星的相关信息很难提取。

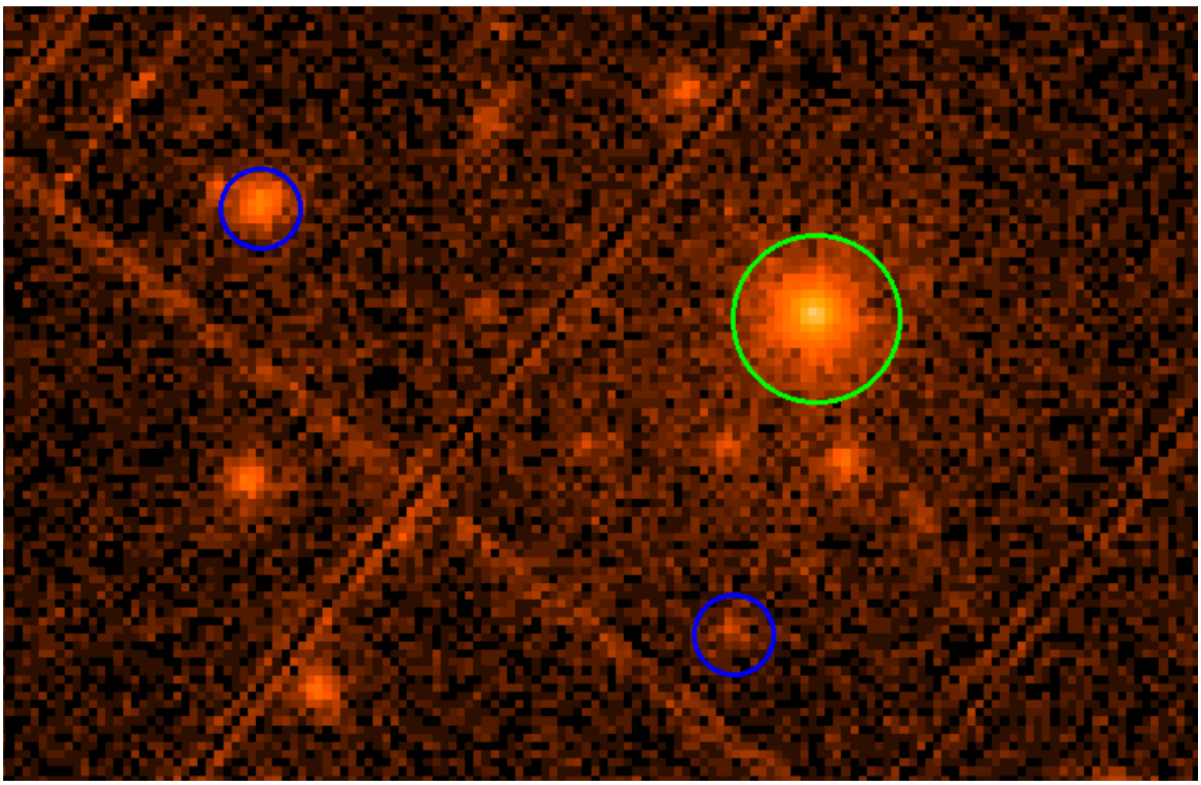

图 3-1 由 XMM-Newton 观测样例 0693760101 得到的视角图，其中绿圈代表在新发现的极亮 X 射线源处于活跃状态下的图片，采用了这个40″角度区域的圆形来分析光谱数据。蓝线为现在已知的极亮 X 射线源，其中左上和左下分别代表 P9 和 P13（用于本文分析）两个源。整个图片观测区域为360″ × 560″，基本上包括了此星系的光学范围[34]。

近年来，对其 X 射线波段的观测也逐渐增多，发现了其中的相干脉冲。2016 年，Fürst 等人结合相关的观测数据，发现了宽频 X 射线辐射中的正弦脉冲信号，周期约为 0.42 秒；此外，因为中子星在双星系统中吸积物质，星风的角动量传输到中子星上，造成了自转持续加速的现象，这也被观测所证实，并给出了自转加速率$\dot{P} \approx 3.5 \times 10^{-11}\mathrm{s/s}$。证实了该双星系统中致密星为脉冲星。因为中子星不能超过奥本海默极限，所以该源如果在各向同性的辐射前提下，确认了超出爱丁顿亮度，

也亟待新理论来解释此种中子星的 X 射线辐射机理。

3.1.2 NGC 300 ULX-1

NGC 300 ULX-1 是在 2010 年第一次以超新星爆发的候选者引起关注。后来被确认为 NGC 300 星系的一个极亮 X 射线源。Vasilopoulos 等人运用 XMM-Newton 的观测结果给出了极亮 X 射线源的观测参数[35]，判断其为中子星极亮 X 射线源系统。而后 Heida 等人对 Very Large Telescope/X-shooter 的 X 射线谱进行了进一步的分析，清楚地表明了其伴星为红超巨星（Red Supergiant，RSG）时精确符合 MARCS 全波段的恒星气象学模型。并给出其伴星有效温度$T_{\mathrm{eff}} = 3650 - 3900\mathrm{K}$，光度$\log\left(L_{\mathrm{bol}}/L_{\odot}\right) = 4.25 \pm 0.10$。作为第二个被发现以超巨星为伴星的极亮 X 射线源，NGC 300 ULX-1 丰富的观测数据与理论研究也为星族合成提供了多种有效的核验方式。他们也提出了近年来的计算发现红超巨星占比很少，可能是没有考虑红超巨星的星风吸积模型，对于中子星-超巨星系统来说，巨大的质量比也让洛希瓣吸积盘很难稳定存在。

3.2 星族合成模拟结果

运用前文介绍的星族合成模拟方法，采取了类银河系星系的恒星生成率（$\mathrm{SFR} = 3\mathrm{M}_{\odot}\mathrm{yr}^{-1}$），计算得到了相关模型的数目展示如表 3-1。

由表可以看出，其风吸积模型中分别取到β=1(B1)，β=2(B2)，β=3(B3)和 BHL 时，星族数目有明显改变，传统的风吸积模型中很难达到极亮 X 射线源的最低亮度，数目分布也十分稀少；新型的风吸积模型显著增加了风吸积极亮 X 射线源的数目，也为极亮 X 射线源的解释提供了一个新的机制。此外，这种吸积模型也是对金属丰度依赖关系很强，这与 Marchant 的理论研究结果十分符合[36]。金属丰度减小时，在洛希瓣式风吸积模型中极亮 X 射线源的数目显著增加，传统的邦迪模式的风吸积极亮 X 射线源数目反而减少。

由表可知，在其他条件相同的前提下，随着风吸积模型的指数β的增加，相应的极亮 X 射线源的数目也随之增加。这应该是与风吸积效率随β的增加而增加有关，具体可见图 2-3。因为随着β的增加，风速到达终端速度也随着延后，相对应的就是风吸积效率增加。

表 3-1 在类银行系星系中模拟计算中，所得中子星极亮 X 射线源风吸积的数目。其中模型标号 B1，B2，B3 和 BHL 分别代表在风吸积模型中 β=1(B1)，β=2(B2)，β=3(B3)。和邦迪风吸积模型。Z 表示金属丰度，Z_⊙表示太阳金属丰度。

Z	B1	B2	B3
$Z_{\odot}$	3.1×10^{-1}	3.7×10^{-1}	6.8×10^{-1}
$0.2Z_{\odot}$	3.2×10^{-1}	6.7×10^{-1}	1.5
$0.02Z_{\odot}$	1.1	2.9	6.3

根据模拟计算的结果，在低金属丰度区域，风吸积极亮 X 射线源的典型伴星为质量在 15 到 40 倍太阳质量之间的超巨星；然而，在太阳金属丰度左右时，小于十倍太阳质量的红超巨星在其中占据了大多数。这也与部分高质量 X 射线双星（High mass X-ray binary，HMXB）的星族合成结果类似。主要是由于相对于高金属丰度的环境，低金属丰度环境下的星体更致密，其恒星半径下降的更快，所以在充满洛希瓣的过程中，低金属丰度的星体更致密。

为了具体探究新型风吸积机制在典型的极亮 X 射线源系统中的影响，伴星质量和轨道周期平面被用来展示不同模式的风吸积影响。其中左侧三列分别代表的β=1(B1)，β=2(B2)，β=3(B3)的洛希瓣式风吸积模式，最右侧一列代表着传统的邦迪吸积模型。前三行分别是金属丰度为 1 倍，0.2 倍，0.02 倍太阳金属丰度的演化模型。其中所采用的双星的轨道参数均是达到极亮源条件$L_x >$

10^{39}erg/s的双星系统，图中颜色深浅表示极亮源的数目对数。其中采取了极亮源 PULX NGC 7793 P13 作为参考系统，如图中蓝色十字所示，其伴星根据观测数据已经基本确认为一个 20 倍太阳质量的 B9Ia 超巨星，且双星系统的轨道周期大约为 64 天，具体介绍可见 3.1.1 小节，因为其为中子星极亮 X 射线源，所以质量比应该在 5 以上，很难形成稳定的洛希瓣吸积，所以是理想的风吸积模型研究对象。

由图可知，P13 源很难由传统的风吸积模型解释。传统的洛希瓣吸积模型中极亮 X 射线源的数目稀少，且在质量轨道平面主要集中于低质量，长轨道周期区域，与 P13 源的观测数据误差十分不符合。然而，在新型的风吸积模型中，部分模型的轨道周期分布完美符合 P13 源的轨道参数。为洛希瓣式风吸积模型提供了强有力的理论支持。

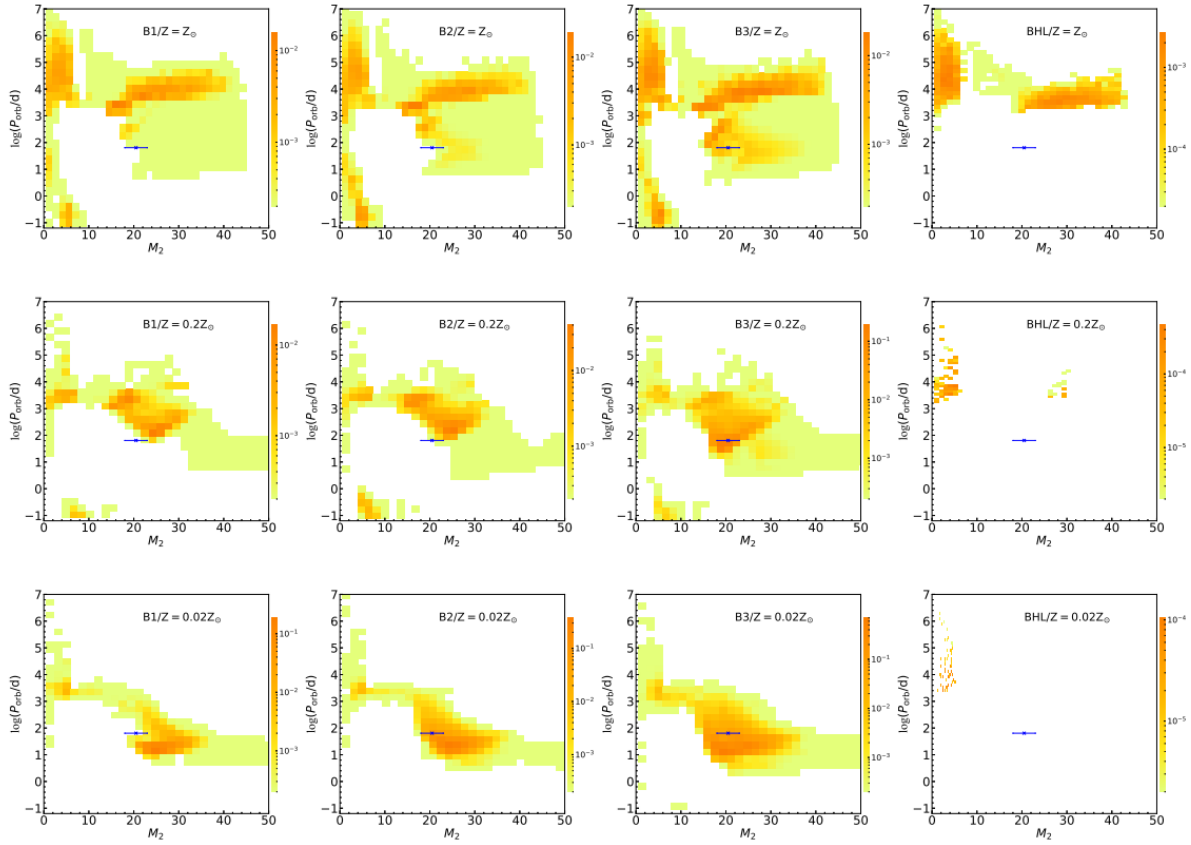

图 3-2 轨道周期-伴星质量分布图。图中四列分别为模型 B1，B2，B3 和 BHL 风吸积模型。并且三行分别对应初始金属丰度为 1 倍，0.2 倍，0.02 倍太阳金属丰度的演化模型。图中颜色代表风吸积模式的中子星极亮 X 射线源的数目占比，其中判断条件为光度大于 10^39 erg/s。图中蓝色误差棒代表的是上文描述的系统 P13 的相关轨道参量。模型标号 B1，B2，B3 和 BHL 分别代表在风吸积模型中 β=1(B1)，β=2(B2)，β=3(B3)。和邦迪吸积模型。

尽管现有争论认为风吸积效率较低，根据 Mohamed 的理论研究结果，风吸积效率不可能超过 50%，此外，我们采用的模型风吸积效率最高为 20%，即便如此，相对于传统的风吸积模型也获得了量级上的提高，和相应的观测结果也有对照。此吸积模式下在太阳金属丰度的环境中，每 1 太阳质量每年的恒星生成率，预测有 0.1 个极亮 X 射线源，如果在金属丰度较小的情况下（$0.02Z_{\odot}$），预测有 1 个极亮 X 射线源诞生，这也达到了观测的数量级（大约 2 个极亮 X 射线源）。将洛希瓣式风吸积模型纳入极亮 X 射线源的考虑范围内也十分合理。

针对于部分太阳金属丰度的模型（如第一行），其明显的分为了两个星族：其一是拥有较长

轨道周期的，一般大于 100 天，主要是来自于小质量的双星系统，并且两者的初始距离也较大，如果讨论某些星暴星系，其演化时间较短，这一类的源的所占比重将会下降。其二就是具有相对较短轨道周期的系统，他们主要是分布在由公共包层产生的 He 燃烧的伴星上。

为了进一步探究极亮 X 射线源中伴星参数，根据伴星的光度和有效温度所得的 H-R 图如图 3-3 所示。同上图一样，前三行分别是金属丰度为 1 倍，0.2 倍，0.02 倍太阳金属丰度的演化模型。图中双星系统筛选条件是达到极亮源条件$L_x > 10^{39}\mathrm{erg/s}$的，图中颜色深浅表示极亮源的数目对数。其中采取了极亮源 PULX NGC 300 ULX-1 作为参考系统，依据最新的观测结果，该双星系统伴星是一个红超巨星，相应的有效温度为$T_{\mathrm{eff}} = 3650 - 3900\mathrm{K}$，恒星光度为$\log\left(L_{\mathrm{bol}}/L_{\odot}\right) = 4.25 \pm 0.10$，如图中蓝色十字所示，具体介绍可见 3.1.2 小节。

由图 3-3 可知，针对于不同的洛希瓣式风吸积模型，都可以解释 NGC 300 ULX-1 系统的轨道参量。然而，传统的风吸积模型却无法涵盖到 NGC 300 ULX-1 的轨道参量。此外，这种红超巨星的轨道参量也十分依赖于初始金属丰度的选择，不同金属丰度下，红超巨星占比差异十分显著。其在高金属丰度下（例如太阳金属丰度）占据主要地位，在低金属丰度下被低有效温度，高光度的源所替代。此外，红超巨星的质量在此次星族合成中皆偏小，并且具有较长的轨道周期，例如 NGC 300 ULX-1，其他的超巨星质量较大，例如 PULX NGC 7793 P13，这也是采用这两个源作为典型特例分析的原因。

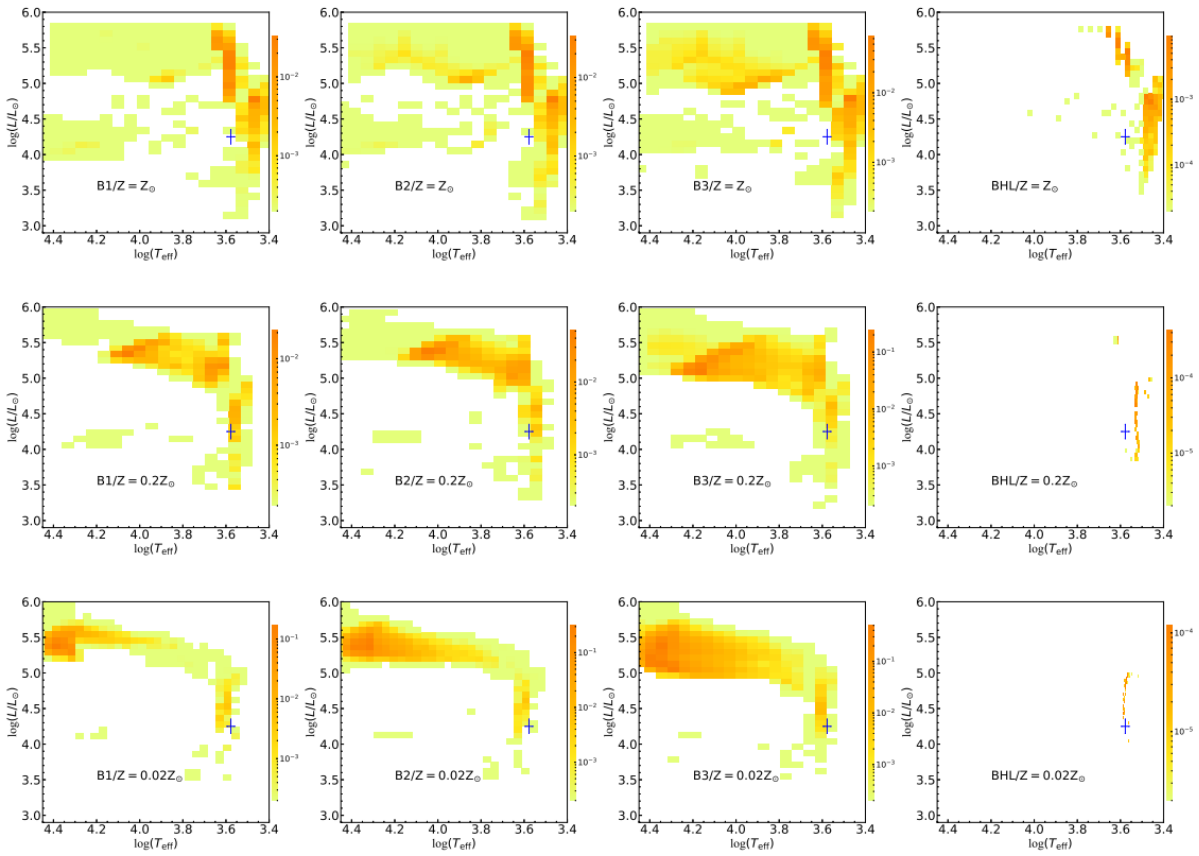

图 3-3 伴星光度-有效温度分布图。图中四列分别为模型 B1，B2，B3 和 BHL 风吸积模型。并且三行分别对应初始金属丰度为 1 倍，0.2 倍，0.02 倍太阳金属丰度的演化模型。图中颜色代表风吸积模式的中子星极亮 X 射线源的数目占比，其中判断条件为光度大于 10^39 erg/s。图中蓝色误差棒代表的是上文描述的系统 PULX NGC 300 ULX-1 的相关伴星观测数据。模型标号 B1，B2，B3 和 BHL 分别代表在风吸积模型中 β=1(B1)，β=2(B2)，β=3(B3)。和邦迪吸积模型。

4 环形星系的 ULX 星族分析

4.1 环形星系

星暴星系（Starburst Galaxy）是指经历十分剧烈的反应，导致恒星形成率显著高于正常水平的星系我们采用了 Wolter 针对不同环状星系的总结归纳，如下表所示[37]。其中可以看出，环状星系的金属丰度相对不集中，这也会导致我们后续计算结果有所出入。环形星系是双星演化研究的理想实验室。尽管它们有助于小分布大约所有螺旋星系的 0.02%-0.2%[38]，但没有杂散源污染的特殊和充满活力的环境适合研究二元进化。环状星系爆发恒星形成的原因是与附近的星系相撞，这意味着恒星的年龄相似。此外，大多数极亮 X 射线源的诞生环境类似。此外，由于恒星形成率（SFR）高和演化持续时间较短，环形星系与我们假设环境具有更多的相似性，从而避免了星族合成的各种初始条件所带来的误差。根据对 NGC2276 星系的总结[39]，在星爆星系中检测到大量的 ULX 强烈支持我们的模拟。

表 4-1 不同环形星系相关参数

Name	Distance(Mpc)	SFR ($M_{\odot}$/yr)	Z($Z_{\odot}$)
Cartwheel	122	20	0.14
NGC 922	48	8.0	0.5-1.
Arp 147	133	4.1	0.19-0.40
AM 0644-741	91.6	2.6	0.45
Arp 143	57.1	2.3	0.44-0.71
Arp 148	145.2	2.5	
Arp 284	37	4.0	0.19-0.38

4.2 环形星系光度函数曲线

本节中的模拟是在恒定 SFR 和金属丰度下进行的。早期形成的环形星系的最大演化时间为 200Myr。由于星暴星系中的恒星形成率相对较高（$SFR > 4.5 M_{\odot} yr^{-1}$），因此可以合理地假设该算法中极亮 X 射线源的数量与恒定 SFR 呈线性关系，这与之前的 Mineo 在 2013 年的工作结果一致[40]。假设观测到的星系的恒星形成率恒定，我们将其与观测和先前的分析进行比较。考虑到恒星形成的复杂事件，应该通过更现实的方法修改估计值。我们采用 Hurly 开发的 EPS 代码用于 BH 双星系统的演化，而中子星双星系统我们采用了 MESA 用于详细模拟极亮 X 射线源的数目。

环状星系比较少见（345 个星系中只有 15 个），但其中极亮 X 射线源占据了相当一部分的比例。根据 wang 等人在 2016 年的工作[40]，星暴星系的观测分析特征（即 X 射线光度函数的形状）与其他星系不同，值得我们关注。由于其纯净的环境和爆发的恒星形成，环形星系可以展示 ULX 的一般特征。此外，年轻星系为恒星演化和早期星系的预测提供了纯净的环境，与 Kovlakas 在 2020 年的工作[10]中的图 15 具有很多的相似性。我们进行了计算，将它们与以星系为中心的观测[37]进行比较。 X 射线光度函数（X-ray Luminosity Function，XLF）的结果如下图所示。

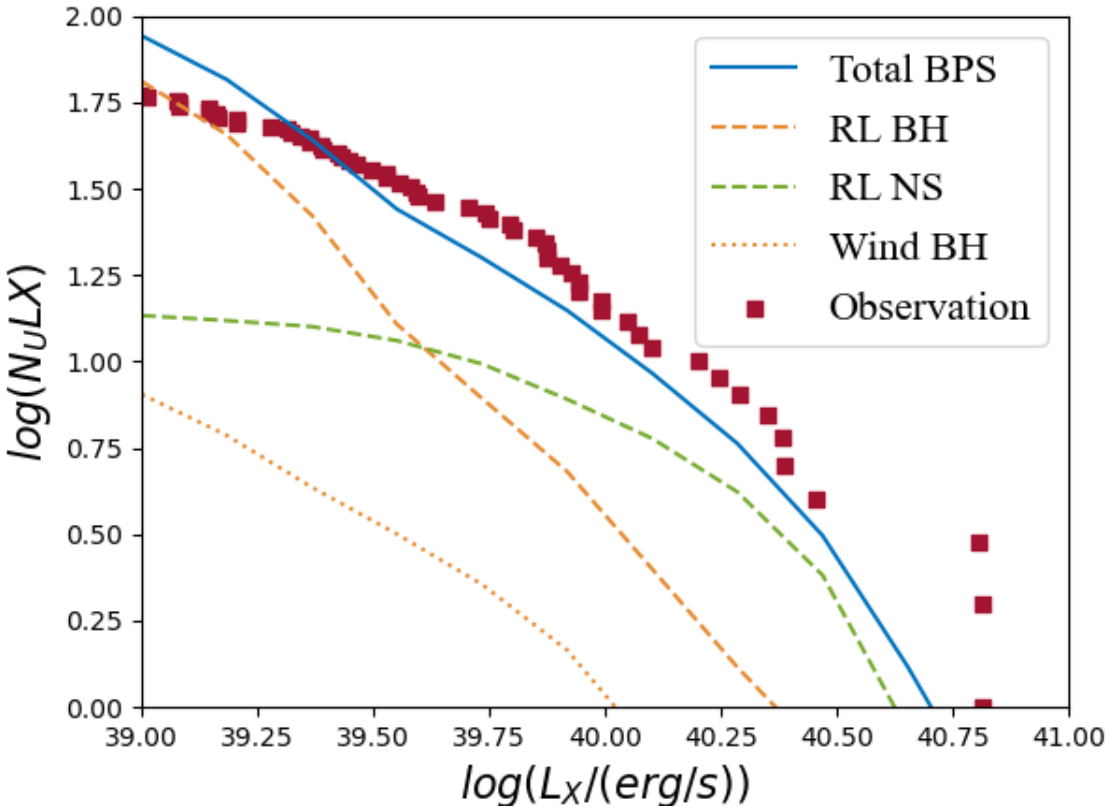

图 4-1 极亮 X 射线源的光度函数。其中 Total BPS 为总的星族合成模拟数目，RL BH 和 RL NS 分别为洛希瓣吸积下主星为黑洞和中子星的数目，Wind BH 为洛希瓣式风吸积模型主星为黑洞的数目，Observation 指观测所得的光度函数。

极亮 X 射线源的预测数量基于前文提及的在星族合成模拟中，特定源数目的计算方法。根据从 $L_{H\alpha}$ [41]获得的 7 个星系的恒星形成率总和约为$43.5M_{\odot}$。此处应注意测量恒星生成率的不确定性，这将导致了我们模拟结果的不确定性，因为在公式中极亮 X 射线源的数目与恒星生成率成正比例关系。因此，对其他有限星系的观察可能与我们的模拟不具有代表性和可比性。收集了极亮 X 射线源在公阈值标准（$10^{39}erg\cdot s^{-1}$，详见 Kaaret 在 2017 年的综述[6]）及以上的 50 个来源，其中 23 个来源高于$5\times10^{39}erg\cdot s^{-1}$。星族合成模拟的结果基本上符合极亮 X 射线源的观测和物理特性。统计上针对极亮 X 射线源的光度函数研究在 2011 年由 Swartz 完成，其中包括在 127 个附近星系中识别出的 107 个 ULX，根据 XLF 的微分函数拟合出幂律斜率。统计拟合已与观测数据进行了比较（如 Wolter 在 2018 年的观测文献图 5[37]）。XLF 中星暴星系与邻近星系的差异明显，邻近星系的 XLF 下降幅度更大。此外，HMXBs [42]中的 XLF 也不可能在星暴星系中拟合。因为这些星系的普查由于其独特的演化阶段和环境，不适合我们对星暴星系的模拟。所以，星族合成研究根据极亮 X 射线源的诞生以及具体的演化过程，更能体现出极亮 X 射线源的观测特征。

根据星族合成方法的模拟结果，在大约$3\times10^{40}erg\cdot s^{-1}$处有一个截断，这与其他星系[43]的观测结果一致。XLF 的截断现有的预测应该是对应于中子星的[44]的爱丁顿光度。尽管有达到峰值光度$10^{41}erg\cdot s^{-1}$的极端天体存在（例如 M82），但它们都被确认为是中等质量黑洞 (IMBH) [45]。它们具有较高质量（$10^2-10^5M_{\odot}$），对应于完全不同的恒星诞生以及演化过程，因此中等质量黑洞不在这项工作的考虑范围内。虽然在我们的模拟中形成极亮的光源（$L_X>3\times10^{40}erg\cdot s^{-1}$）有诞生的可能，但它们需要非常低几何结构因子，因此基本上不会被观测到。此外，这些案例在环形星系

中的观察也很有限[46]，所以我们重点关注 XLF 的中间部分。

在这种各向异性机制下，通过风洛希瓣流的吸积模式有助于物质传输率相对较低。虽然吸积物质比例μ在 WRL 中小于 20% 并且必须小于 50%[47] 。这意味着在吸积过程中大部分质量损失，但通过洛希瓣式风吸积的极亮 X 射线源存在并且可以达到$5 \times 10^{40} erg \cdot s^{-1}$。在我们的模拟中，高质量的吸积星体在高物质传输率情形下为 X 射线辐射提供了足够的燃料。对于风洛希瓣流，伴星充满洛希瓣，而这种情形在洛希瓣吸积情形下就十分不稳定。因此，在洛希瓣吸积中，伴星的质量比限制比洛希瓣式风吸积更严格。在我们的模拟中，洛希瓣式风吸积的高质量比（大于 3）和高伴星质量（$> 10 M_{\odot}$）在洛希瓣式风吸积情况下很常见，而对于洛希瓣吸积则不稳定。我们可以得出结论，在这些演化阶段，吸积可以通过洛希瓣式风吸积保持稳定，具有洛希瓣式风吸积的 ULXs 在低光度区域占据 XLF 的一部分。

对于洛希瓣吸积，它们的数目在光度函数中占主导地位，可以根据致密星种类分为两组（BH 或 NS）。对于亮度较低的光源，极亮 X 射线源的致密星往往是 BH 而不是 NS。我们注意到在高光度下黑洞洛希瓣吸积的持续时间明显长于中子星，因此更有可能被观察到。中子星的质量和半径远小于黑洞，在下一个演化阶段之前，恒定传质的持续时间更难维持。黑洞通过洛希瓣渗溢的典型轨道周期是几天，并且伴星恒星质量往往小于 2.7 个太阳质量。较低的初始伴星恒星质量表明出生概率较高，相应地，对应星族中的占比就大。

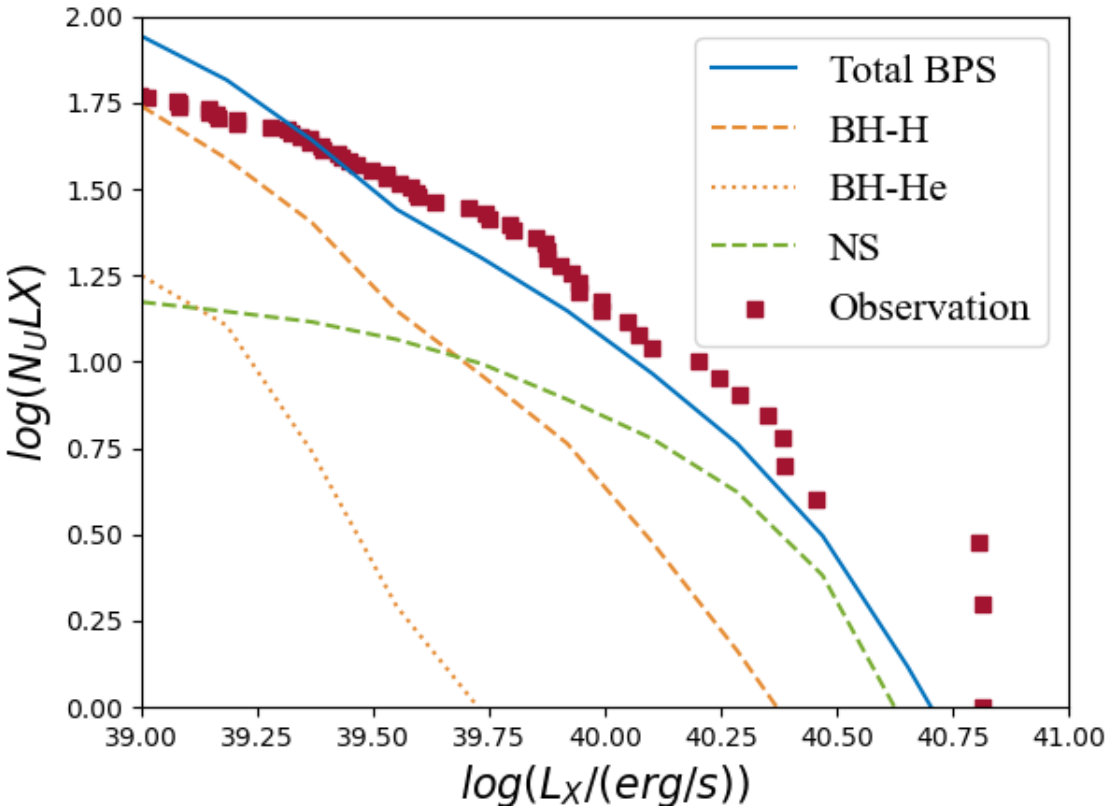

图 4-2 极亮 X 射线源的光度函数。其中 Total BPS 为总的星族合成模拟数目，BH-H 和 BH-He 分别为洛希瓣吸积下主星为黑洞，伴星主要燃烧元素为氢和氦，NS 为中子星极亮 X 射线源的数目，Observation 指观测所得的光度函数。

中子星在亮度较高的区域占主导地位$L_{app} > 10^{40} erg \cdot s^{-1}$\$，这与前期的工作可比拟。在我们的模拟中，光束因子和光度之间存在已证明的正相关关系。 黑洞极亮 X 射线源中的 X 射线辐射通常是各向同性的或轻度辐射的。然而，在 NS 极亮 X 射线源中，beaming 效应是明显的，并且在某些情况下可以达到饱和光束（$b_{min} = 3.2 \times 10^{-3}$ 详见 Lasota2016 年的研究[48]），这是导致中子星极

亮 X 射线源的高亮度的直接原因。

在上图中，我们显示了富氦和富氢伴星的分布。为了分析极亮 X 射线源的年龄，我们在模拟中执行了不同的演化持续时间，并将它们展示在图中。我们为不同的演化持续时间绘制了不同颜色的 XLF。更明亮的极亮 X 射线源的数量在大于 150Myr 的年龄显着下降，其致密星对应于 NS。当年龄约为 30 Myr 时，带有黑洞的极亮 X 射线源占主导地位。年龄小于 20 Myr 的双星系统仅贡献了少量一部分，因为这需要严格的条件才能快速形成致密星。大多数年轻极亮 X 射线源的持续时间通常很短，因此对这些双星的观察很少。大多数极亮 X 射线源的年龄约为 150Myr，这表明极亮 X 射线源是 HMXBs[24]的尾部进化阶段。在我们的模型中，200Myr 之后的星族数目增长并不明显，超出了我们在这个环形星系案例中的考虑。

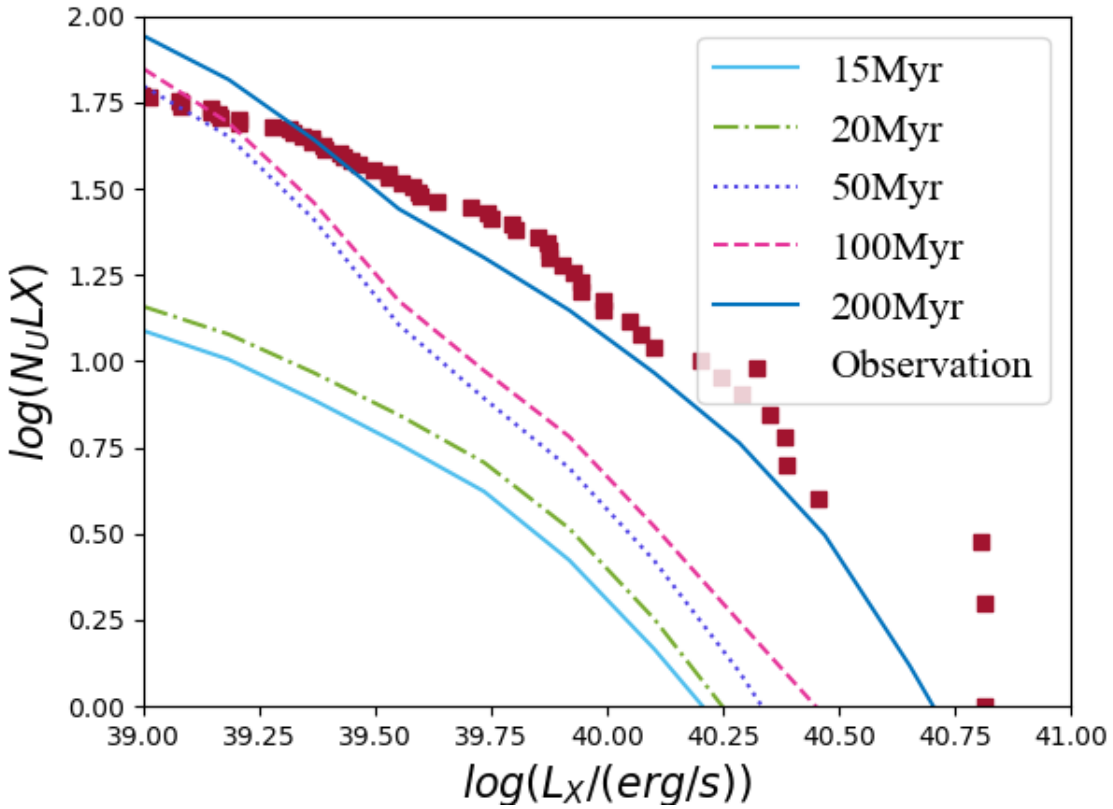

图 4-3 极亮 X 射线源的光度函数。其中不同颜色代表不同最大演化时间对应的极亮 X 射线源数目，Observation 指观测所得的光度函数。

我们同时也给出了光度大于$10^{39} erg \cdot s^{-1}$时极亮 X 射线源的轨道周期数值分布。其每个元素的总体计算方式与上小节中光度函数计算相同。可以看出，轨道周期短于 10 天的双星占主导地位，这与之前邵勇的工作[13]相对应。显然，较低的发光区域包含更多的极亮 X 射线源。此外，详细分析表明，轨道周期较短的极亮 X 射线源的传质机制倾向于洛希瓣渗溢，而洛希瓣式风吸积的极亮 X 射线源是轨道周期较长的系统。在星暴星系中，具有洛希瓣式风吸积的供体恒星质量更大，而较短的周期是恒定质量转移的不稳定因素。由于初始质量函数中较大的诞生几率，较低质量的伴星占很大比例。此外，带有洛希瓣式风吸积的极亮 X 射线源也对这个图有贡献，但质量跨度很大，每个元素的分布很小。观测 BH 极亮 X 射线源的情况很少，轨道参数难以确定。 刘继峰等人已经揭示了带有 BH 和沃尔夫-拉叶星的 M101 ULX-1 [49]，并确认轨道周期为 8.2 天。之后 Titarchuk, Lev 等人分析了 M101 的光谱[50]，估计主星黑洞质量约为$10^4 M_{\odot}$，这是一个中等质量黑洞，因此我们无法在质量轨道平面上预测这个黑洞。

5 结论与展望

本文主要是基于星族合成模拟方法，针对近年来形成机理尚未清楚的极亮 X 射线源进行了多方面的探究。相比于传统的极亮 X 射线源的星族研究而言，创新性的引入了星风吸积模型，采用了 I. El Mellah 等人的数值模拟工作，没有采用传统的 BHL 风吸积模型，从而证实了极亮 X 射线源条件是可以在洛希瓣式风吸积模型中达到的。

为了进一步验证模型的合理性，借助 BSE 和 MESA 星族合成软件，模拟了不同β和金属丰度下极亮 X 射线源的星族，首先采用了质量-轨道周期分布来比较观测的中子星极亮 X 射线源与星族合成模拟的异同，其中 P13 源在较高风吸积效率指数时完美符合理论预测。质量-轨道周期分布同时也给出了不同星族分类的概况，其中长周期，大于 100 天的，主要是来自于小质量的双星系统，并且两者的初始距离也较大；此外具有相对较短轨道周期的系统，他们主要是分布在由公共包层产生的 He 燃烧的伴星上。除此之外，理论模拟也给出了 H-R 图来表示恒星伴星光度和有效温度之间的关系。并且与观测得到的 PULX NGC 300 ULX-1 源的相关参数进行比较，在多个参量空间下均符合观测特征，也证实了之前推测其为风吸积下极亮 X 射线源的猜测。我们注意到风吸积的中子星极亮 X 射线源的绝对形成率是高度不确定的。例如恒星形成率、单双星比例、主次星的初始质量函数以及新生中子星的 kick 可能对其产生两个数量级级别的影响。

此外，针对于单一类型的数个环状星系，用星族合成方法得到了其光度函数曲线，发现其与 Wolter 在 2018 年统计的观测所得的曲线基本吻合，其中新加入的洛希瓣式风吸积模型也在极亮 X 射线源中占据相当一部分。此外，针对于极亮 X 射线源的星族，黑洞洛希瓣系统仍占据主要部分，因为其高物质传输率和稳定的物质传输效率使其更易达到极亮 X 射线源的条件，中子星洛希瓣吸积在高光度时数目更多，是由于其高 beaming 而导致的各向异性辐射。进行伴星主要构成元素的分析，都是以伴星为氢燃烧为主，也说明了此类恒星还未到演化的后期，后续的不同时间下的光度函数曲线也证实了这一点。

本次课题的研究还缺少更广泛的参量空间下的模拟，例如恒星生成率对其影响；在非星暴星系下，不同的恒星诞生环境对于其轨道周期分布以及光度函数的影响；大质量恒星的恒星风的不确定因素。此外，更细致的超爱丁顿亮度的风吸积和洛希瓣吸积可以考虑到参数空间中去，在双星演化过程中，风吸积速率是个很难确定的量，各向异性的情况下，风吸积速率可能会由于双星质量比，轨道周期，双星间距而显著改变，这一点可以在未来的研究中予以重视。

致 谢

大学四年已经过去，这篇毕业设计也是对我这一路来的总结，从初入茅庐，到现在完成这篇毕业设计，自己的路才刚刚开始，路漫漫其修远兮，吾将上下而求索。

这一路以来最感谢的就是左兆宇老师，在给我科研上悉心指导的同时，也在我精神上压力大的时候，给予了我支持和鼓励，也包容了我许多在科研中的错误。从选题，到工作进展，再到困难的克服，各种软件的使用，左老师都给予了很大帮助。左老师是我科研路上的第一位导师，也是我走向天文路上的引路人，滴水之恩必当涌泉相报。

另外还要感谢同组的薛瀚宸，张倍铭，胡泽浩，杨涛只老师在科研过程中的交流讨论，他们也让我感受到了，科研工作永远都不是一个人能完成的，交流与讨论才是更上一层的阶梯。“人不可有傲气，但不可无傲骨。”在以后的道路上，我也一定要谦逊待人，砥砺前行。

最后要感谢我的父母，在我困难的时候给了我信心和勇气。有时候自己迷茫困惑，也是父母给了我未来的保障与前进的动力。这四年，是我第一次离开家的四年，也是我最多成长与感悟的四年，我的父母给予了我无限关怀，让我勇于面对困难。

参考文献

[1] Pakull M W, Mirioni L. Optical Counterparts of Ultraluminous X-Ray Sources, 2002: astro-ph/0202488.
[2] 孔旭, 程福臻. 演化的星族合成方法[D]. 2001.
[3] Begelman M C, King A R, Pringle J E. The nature of SS433 and the ultraluminous X-ray sources[J]. Monthly Notices of the Royal Astronomical Society, 2006, 370: 399.
[4] Hurley J R, Pols O R, Tout C A. Comprehensive analytic formulae for stellar evolution as a function of mass and metallicity[J]. Monthly Notices of the Royal Astronomical Society, 2000, 315(3): 543-569.
[5] Hurley J R, Tout C A, Pols O R. Evolution of binary stars and the effect of tides on binary populations[J]. Monthly Notices of the Royal Astronomical Society, 2002, 329(4): 897-928.
[6] Kaaret P, Feng H, Roberts T P. Ultraluminous X-ray sources[J]. Annual Review of Astronomy and Astrophysics, 2017, 55: 303-341.
[7] Kajava J J E, Poutanen J. Spectral variability of ultraluminous X-ray sources[J]. Monthly Notices of the Royal Astronomical Society, 2009, 398: 1450.
[8] Swartz D A, Soria R, Tennant A F, et al. A Complete Sample of Ultraluminous X-Ray Source Host Galaxies[J]. The Astrophysical Journal, 2011, 741(1): 49.
[9] Wang S, Qiu Y, Liu J, et al. Chandra ACIS Survey of X-Ray Point Sources in Nearby Galaxies. II. X-Ray Luminosity Functions and Ultraluminous X-Ray Sources[J]. The Astrophysical Journal, 2016, 829(1): 20.
[10] Kovlakas K, Zezas A, Andrews J J, et al. A census of ultraluminous X-ray sources in the local Universe[J]. Monthly Notices of the Royal Astronomical Society, 2020, 498(4): 4790-4810.
[11] Liu J-F, Bregman J N, Bai Y, et al. Puzzling accretion onto a black hole in the ultraluminous X-ray source M 101 ULX-1[J]. Nature, 2013, 503: 500.
[12] Bachetti M, Harrison F A, Walton D J, et al. An ultraluminous X-ray source powered by an accreting neutron star[J]. Nature, 2014, 514(7521): 202-4.
[13] Shao Y, Li X-D. A Population of Ultraluminous X-ray Sources with An Accreting Neutron Star[J]. The Astrophysical Journal, 2015, 802(2): 131.
[14] Belczynski K, Kalogera V, Rasio F A, et al. Compact object modeling with the StarTrack population synthesis code[J]. The Astrophysical Journal Supplement Series, 2008, 174(1): 223.
[15] Wiktorowicz G, Lasota J-P, Middleton M, et al. The Observed versus Total Population of ULXs[J]. The Astrophysical Journal, 2019, 875(1): 53.
[16] Wiktorowicz G, Sobolewska M, Lasota J-P, et al. The Origin of the Ultraluminous X-Ray Sources[J]. The Astrophysical Journal, 2017, 846(1): 17.
[17] Shao Y, Li X-D, Dai Z-G. A Population of Neutron Star Ultraluminous X-Ray Sources with a Helium Star Companion[J]. The Astrophysical Journal, 2019, 886(2): 118.
[18] Wiktorowicz G, Lasota J-P, Belczynski K, et al. Wind-powered ultraluminous X-ray sources[J]. arXiv preprint arXiv:2103.02026, 2021.
[19] Eggleston S J, Turiel E. The Development of Social Knowledge[M]. The development of social knowledge :, 1983.
[20] King A. Accretion rates and beaming in ultraluminous X-ray sources[J]. Monthly Notices of the Royal Astronomical Society: Letters, 2008, 385(1): L113-L115.
[21] King A R, Puchnarewicz E M. Black hole blackbodies[J]. Monthly Notices of the Royal Astronomical Society, 2002, 336(2): 445-448.
[22] Feng H, Kaaret P. Origin of the X-ray Quasi-Periodic Oscillations and Identification of a Transient Ultraluminous X-Ray Source in M82[J]. Astrophysical Journal, 2007, 668(2): 941-948.

[23] Servillat M, Farrell S A, Lin D, et al. X-Ray Variability and Hardness of ESO 243-49 HLX-1: Clear Evidence for Spectral State Transitions[J]. The Astrophysical Journal, 2011, 743: 6.
[24] Zuo Z-Y, Li X-D, Gu Q-S. Population synthesis on high-mass X-ray binaries: prospects and constraints from the universal X-ray luminosity function[J]. Monthly Notices of the Royal Astronomical Society, 2014, 437(2): 1187-1198.
[25] Edgar R. A review of Bondi–Hoyle–Lyttleton accretion[J]. New Astronomy Reviews, 2004, 48(10): 843-859.
[26] Mohamed S, Podsiadlowski P. Wind Roche-Lobe Overflow: a new mass-transfer mode for wide binaries[C]. 15th European Workshop on White Dwarfs, 2007: 397.
[27] Mohamed S, Podsiadlowski P. Mass transfer in Mira-type binaries[J]. Open Astronomy, 2012, 21(1-2): 88-96.
[28] Abate C, Pols O R, Izzard R G, et al. Wind Roche-lobe overflow: Application to carbon-enhanced metal-poor stars[J]. Astronomy & Astrophysics, 2013, 552.
[29] Hoefner S. Headwind: Modelling Mass Loss of AGB Stars, Against All Odds[J]. astro.uu.se, 2007.
[30] El Mellah I, Sundqvist J O, Keppens R. Wind Roche lobe overflow in high-mass X-ray binaries[J]. Astronomy & Astrophysics, 2019, 622: L3.
[31] Pavel K, Tout C A, Gerard G. The distribution of low-mass stars in the Galactic disc[J]. Monthly Notices of the Royal Astronomical Society, 1993(3): 545-587.
[32] Lamers H J, Snow T P, Lindholm D M. Terminal velocities and the bistability of stellar winds[J]. The Astrophysical Journal, 1995, 455: 269.
[33] Read A, Pietsch W. ROSAT observations of the Sculptor galaxy NGC7793[J]. arXiv preprint astro-ph/9810013, 1998.
[34] Quintin E, Webb N, Gúrpide A, et al. A new candidate pulsating ULX in NGC 7793[J]. Monthly Notices of the Royal Astronomical Society, 2021, 503(4): 5485-5494.
[35] Vasilopoulos G, Haberl F, Carpano S, et al. NGC 300 ULX1: A test case for accretion torque theory[J]. A&A, 2018, 620: L12.
[36] Marchant P, Langer N, Podsiadlowski P, et al. Ultra-luminous X-ray sources and neutron-star–black-hole mergers from very massive close binaries at low metallicity[J]. Astronomy & Astrophysics, 2017, 604: A55.
[37] Wolter A, Fruscione A, Mapelli M. The X-Ray Luminosity Function of Ultraluminous X-Ray Sources in Collisional Ring Galaxies[J]. The Astrophysical Journal, 2018, 863(1).
[38] Wolter A, Consolandi G, Longhetti M, et al. The Cartwheel galaxy as a stepping stone for binaries formation[J]. International Astronomical Union. Proceedings of the International Astronomical Union, 2018, 14(S346): 297-306.
[39] Wolter A, Esposito P, Mapelli M, et al. NGC 2276: a remarkable galaxy with a large number of ultraluminous X-ray sources[J]. Monthly Notices of the Royal Astronomical Society, 2015, 448(1): 781-791.
[40] Mineo S, Rappaport S, Steinhorn B, et al. Spatially Resolved Star Formation Image and the Ultraluminous X-Ray Source Population in NGC 2207/IC 2163[J]. The Astrophysical Journal, 2013, 771(2): 133.
[41] Appleton P, Marston A. Multiwavelength Observations of Collisional Ring Galaxies. I. Broad-Band Images, Global Properties, and Radial Colors of the Sample Galaxies[J]. The Astronomical Journal, 1997, 113: 201-224.
[42] Grimm H-J, Gilfanov M, Sunyaev R. High-mass X-ray binaries as a star formation rate indicator in distant galaxies[J]. Monthly Notices of the Royal Astronomical Society, 2003, 339(3): 793-809.
[43] Mineo S, Gilfanov M, Sunyaev R. X-ray emission from star-forming galaxies–I. High-mass X-ray binaries[J]. Monthly Notices of the Royal Astronomical Society, 2012, 419(3): 2095-2115.
[44] Belczynski K, Ziolkowski J. On the apparent lack of Be X-ray binaries with black holes[J]. The Astrophysical Journal, 2009, 707(2): 870.
[45] King A R. The brightest black holes[J]. Monthly Notices of the Royal Astronomical Society, 2002, 335: L13.
[46] Liu J-F, Bregman J N. Ultraluminous X-Ray Sources in Nearby Galaxies from ROSAT High Resolution Imager Observations I. Data Analysis[J]. The Astrophysical Journal Supplement Series, 2005, 157: 59.
[47] Mohamed S, Podsiadlowski P. Wind Roche-lobe overflow: a new mass transfer mode for Mira-type

binaries[C]. Why Galaxies Care about AGB Stars II: Shining Examples and Common Inhabitants, 2011: 355.
[48] Lasota J-P, Vieira R, Sadowski A, et al. The slimming effect of advection on black-hole accretion flows[J]. Astronomy & Astrophysics, 2016, 587: A13.
[49] Liu J-F, Bregman J N, Bai Y, et al. Puzzling accretion onto a black hole in the ultraluminous X-ray source M 101 ULX-1[J]. Nature, 2013, 503(7477): 500-503.
[50] Titarchuk L, Seifina E. Scaling of the photon index vs. mass accretion rate correlation and estimate of black hole mass in M101 ULX-1[J]. Astronomy & Astrophysics, 2016, 585: A94.

附 录A 英文文献原文

High-mass X-ray Binaries: Illuminating the Passage from Massive Binaries to Merging Compact Objects
Proceedings IAU Symposium No. 346, 2019
L. M. Oskinova, E. Bozzo, T. Bulik & D. Gies, eds.

doi:10.1017/S1743921319001157

The Cartwheel galaxy as a stepping stone for binaries formation

Anna Wolter[1], Guido Consolandi[1,2] Marcella Longhetti[1], Marco Landoni[1] and Andrea Bianco[1]

[1]INAF-Osservatorio Astronomico di Brera,
Via Brera 28, I-20121 Milano, Italy
email: anna.wolter@inaf.it

[2]Universitá degli Studi di Milano Bicocca,
Piazza dell'Ateneo Nuovo, 1, I-20126 Milano, Italy
email: guido.consolandi@inaf.it

Abstract. Ultraluminous X-ray sources (ULXs) are end points of stellar evolution. They are mostly interpreted as binary systems with a massive donor. They are also the most probable progenitors for BH-BH, and even more, for BH-NS coalescence. Parameters of ULXs are not know and need to be better determined, in particular the link with the metallicity of the environment which has been invoked frequently but not proven strongly. We have tackled this problem by using a MUSE DEEP mosaic of the Cartwheel galaxy and applying a Monte Carlo code that jointly fits spectroscopy and photometry. We measure the metallicity of the emitting gas in the ring and at the positions of X-ray sources by constructing spatially resolved emission line ratio maps and BPT diagnostic maps. The Carthweel is the archetypal ring galaxy and the location and formation time of new stellar populations is easier to reconstruct than in more normal galaxies. It has the largest population of ULXs ever observed in a single galaxy (16 sources have been classified as ULXs in Chandra and XMM-Newton data). The Cartwheel galaxy is therefore the ideal laboratory to study the relation between Star Formation (SF Rates and SF History) and number of ULXs and also their final fate. We find that the age of the stellar population in the outer ring is consistent with being produced in the impact ($\leqslant 300 Myr$) and that the metallicity is mostly sub-solar, even if solutions can be found with a solar metallicity that account for most observed properties. The findings for the Cartwheel will be a testbed for further modelisation of binary formation and evolution paths.

Keywords. stars: binaries, galaxies: individual (Cartwheel), galaxies: peculiar, galaxies: interaction, galaxies: evolution

1. Introduction

Why did we choose the Cartwheel galaxy? The Cartwheel is the epitome of the Ring Galaxies (RiGs), in which many ultra luminous X-ray sources (ULXs) are produced as end points of stellar evolution. We have shown (see later) that ULXs are in general the high luminosity tail of high mass X-ray binaries (HMXB; see also contributions by Roberts or Kovlakas, this volume). They are the testimony of a recent event: the gravitational encounter of two galaxies. In RiGs, the location and formation time of new stellar populations are easier to reconstruct than in normal spirals due to the simpler geometry and dynamics. Brighter ULXs seem to be preferentially found in low metallicity environments. Two possibilities have been put forward: a) the largest black holes (BH) are constructed from direct collapse of low metallicity stars (e.g. Mapelli *et al.* 2009)

or b) metal-poor X-ray binaries are more luminous than their metal-rich peers (Linden *et al.* 2010, which could be the case for both BH or neutron stars (NS) counterparts (see also contributions by Artale, this volume).

The Cartwheel belongs to a compact group of 4 members (Iovino 2002) at a distance of D = 122 Mpc. The shock wave of the encounter with one of the group galaxies has launched a shock wave that has triggered star formation and enhanced emission in all bands. The consequence of this star formation is the large number of ULXs found, especially in the ring - see Wolter *et al.* (2015).

The recent Gravitational Waves (GW) detections have increased the interest of ULXs as possible sites of coalescence. Many authors have used the ULXs as progenitors to compute the expectancy for GW detection of different kinds of merging, in particular the NS-BH event which has not been detected yet. Many recent estimates of expected rates (e.g. Inoue *et al.* 2016) do take into consideration the ULX properties (Luminosity Function, active time, frequency by galaxy mass or SFR). However, many of these parameters are very uncertain or not known (see also contributions by Giacobbo *et al.*, by Erkut *et al.* and by Fabrika *et al.* this volume).

We use an operative definition of ULX as an extra-galactic, point-like, non-nuclear, X-ray source with 10^{39} erg/s $< L_X < 10^{42}$ erg/s (Fabbiano 1989). This definition is bound to create a mixed class of sources and includes interlopers, like background AGNs, and at least a subclass of Supernovae, possibly numbering about 25% of all ULXs (Swartz *et al.* 2011). The majority of ULXs nevertheless are thought to be binary systems, with a degenerate object and a large (in most cases) companion. The engine of the system might be: a) an Intermediate Mass BH (10^{2-5} $M_\odot$ - this was the initial guess but now runs a bit out of fashion; b) a BH with a heavy stellar mass (30-100 $M_\odot$) or c) a Neutron Star - this has been proven for at least 5 cases (Bachetti *et al.* 2014, Israel *et al.* 2017a,b, Fuerst *et al.* 2016, Carpano *et al.* 2018) out of a few hundred ULXs.

2. The X-ray Luminosity Function of ULXs

First we use the X-ray luminosity function (XLF) to show that ULXs are related to HMXB, which are the subject of this meeting, and therefore deserve attention here. A number of authors, including us, has produced the XLF for individual galaxies with a large number of ULXs (Cartwheel: Wolter & Trinchieri 2004; Antennae: Zezas *et al.* 2007; NGC337: Somers *et al.* 2013; NGC 2276: Wolter *et al.* 2015) and compared it with the so-called universal luminosity function of HMXB by Grimm *et al.* (2003). The normalization of the XLF for the Star Formation Rate (SFR), measured typically via the Hα luminosity, is consistent with the idea that ULXs are linked to recent star formation bursts. The smooth connection with the lower luminosity sources and the slope of the XLF are consistent with our hypothesis.

This is also shown by the XLF of both a large number of ULXs collected in the rings of seven collisional RiGs (Wolter *et al.* 2018) and those in the collection of nearby galaxies (Swartz *et al.* 2011) observed by Chandra, which yield a similar number of ULXs and consistent results between each other, even if the RiGs have a possible excess at high luminosity. The combination of many galaxies relies on the assumption that we are witnessing a single burst of star formation in each galaxy, with a reasonable short age (possibly less than 100 Myr as per the simulations of Renaud *et al.* 2018), close to the formation time of HMXB, and that the spread in metallicity is not large. In any case, the effect of metallicity is not predominant with respect to the SFR (see e.g. Mapelli *et al.* 2010).

The Cartwheel, with its 15 out 65 sources in the collection of ring galaxies, is the best testbed in which to search for new information about the environment of formation and evolution of ULXs and HMXB in general. A measure of the metallicity of the Cartwheel is available in the literature (Fosbury *et al.* 1977), measured in the brightest HII regions. The

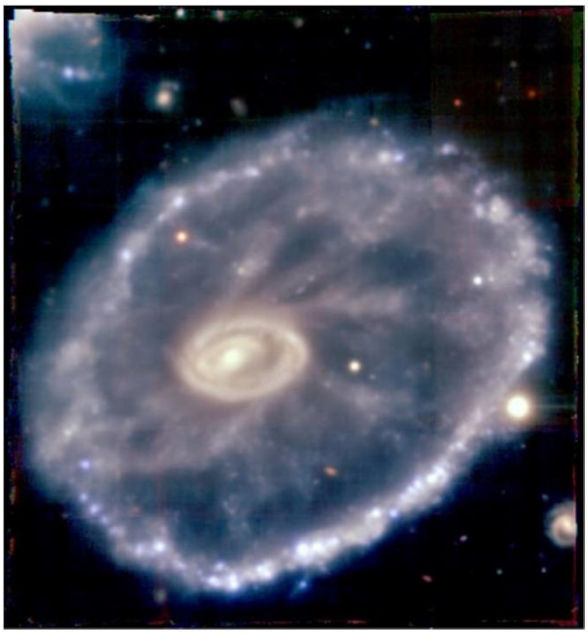

Figure 1. Three color image derived from Muse data - using filters matching as close as possible the g, i and r Gunn filters.

age of the star burst is not known, even if a few estimates of the epoch of the encounter are available in the literature: Higdon (Higdon 1996) estimates 300 Myr from the impact from the HI velocity field; Amram (Amram *et al.* 1998) estimate the age of the ring at > 200 Myr from Hα kinematics (13-30 km/s expansion); while Renaud (Renaud *et al.* 2018) run detailed simulations that imply an age < 100 Myr for the persistence of ring.

We intend therefore to study the Cartwheel to address these issues.

3. MUSE data

The Cartwheel was observed by MUSE in Aug 2014 for calibration purposes with a mosaic of four 4 ksec pointings to include the entire ring (1.4×1.5 arcmin). The data have been downloaded from the ESO archive. The MUSE 3D science data cubes have their instrumental signature removed, and are astrometrically calibrated, sky-subtracted, wavelength and flux calibrated, using the MUSE pipeline, version muse-1.4 and higher. We show in Figure 1 a color image, obtained by filtering on the Gunn filters g, i, and r the band pass of MUSE (details in Wolter *et al.* in prep).

To robustly estimate emission line fluxes, we accounted for the stellar absorptions underlying the Balmer emission lines that fall in the MUSE spectral window: Hα and Hβ. For this, we used the code GANDALF (Sarzi *et al.* 2006) complemented by the penalize pixel-fitting code (Cappellari & Emsellem 2004) to simultaneously model the stellar continuum and the emission lines in individual spaxels with S /N > 5. The stellar continuum was modeled with the superposition of stellar templates from the MILES library (Vazdekis *et al.* 2010) convolved by the stellar line-of-sight velocity distribution, whereas the emission lines and kinematics were modeled assuming a Gaussian profile. In each spaxel, the modeled stellar continuum spectrum was subtracted from the observed spectrum to obtain a final datacube of pure emission lines that is free of stellar absorption.

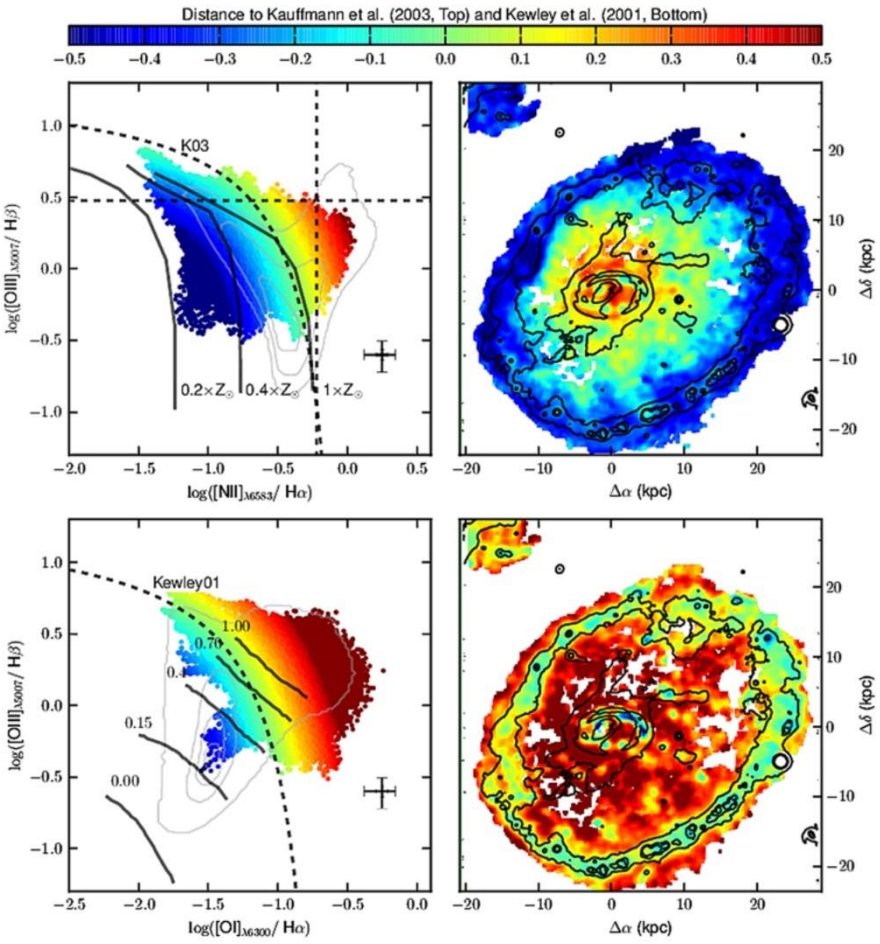

Figure 2. BTP diagrams: see text for details. *Top-left*: [OIII]λ5007/Hβ vs. [NII]λ6583/Hα. *Top-right*: map of the spaxel contributing to the BPT, color-coded as in the top-left panel. *Bottom-left*: [OIII]λ5007/Hβ vs. [OI]λ6300/Hα *Bottom-right*: map of the spaxels contributing to the BPT, color-coded as in the bottom-left panel.

3.1. *Metallicity*

We have extracted "line" images (for Hα, Hβ, [OIII], [OI] and [NII]). We can then use those images to compute standard classification diagrams resolved in spaxels, as the two BTP diagnostic maps shown in Figure 2. In the top-left panel the [OIII]λ5007/Hβ vs. [NII]λ6583/Hα is plotted. The dashed curve separates AGN from HII regions and is adopted from Kauffmann *et al.* 2003 (Ka03). Data (in the top-right panel) are color-coded according to their minimum distance to the Ka03 curve. The black crosses indicate the typical error of the ratio of lines with a S/N $\sim$ 15/5. Thick solid lines show the three different photoionization models at different metallicities (0.2 $Z_\odot$, 0.4 $Z_\odot$ and $Z_\odot$) by Kewley *et al.* (2001).

In the bottom-left panel the [OIII]λ5007/Hβ vs. [OI]λ6300/Hα is plotted. The dashed curve separates AGN from HII regions and is adopted from Kewley *et al.* 2001 (Ke01).

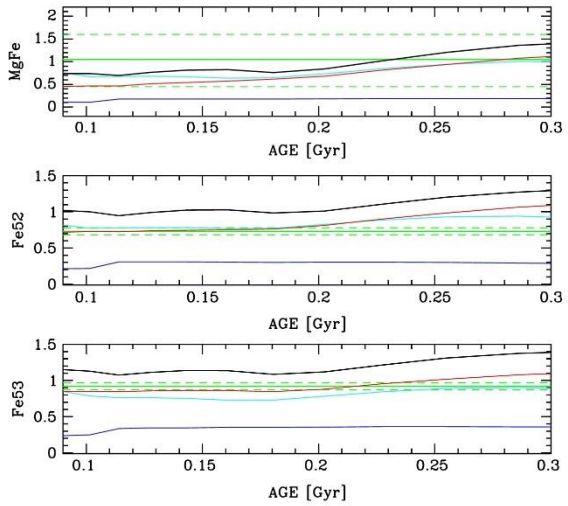

Figure 3. Comparison between BC03 models expectations and MgFe (*top panel*), Fe5270 (*middle panel*) and Fe5335 (*lower panel*) indices measures of the Cartwheel outer ring spectrum. The green lines represent our measures (*solid line*) and their errors (*short dashed line*). In each panel, expected indices values as a function of the age of a SSP are reported for solar metallicity (*black line*), Z = 0.4 $Z_\odot$ (*red line*), Z = 0.2 $Z_\odot$ (*cyan line*) and Z=0.02 $Z_\odot$ (*blue line*).

Data (in the bottom-right panel) are color-coded according to their minimum distance to the Ke01 curve. The black crosses indicate the typical error of the ratio of lines with a S/N $\sim$ 15/5. Thick solid lines show the five different shock models by Rich *et al.* 2011, indicating five different fractions (from 0 to 1) of Hα flux contributed by shocks.

A general assessment of the metallicity in the galaxy shows that the metallicity of the ring is consistently lower than in the rest of the galaxy. The small portion of G1 visible in the upper left corner shows about the same metallicity of the ring. The central region appears supersolar. However, as shown in the bottom panels, where [OI] is used instead of [NII], we cannot exclude the presence of shocks that contribute to the line ratios.

3.2. *Spectra and inferences*

It is notorious that metallicity of stars and age of the galaxy give similar effects on the optical spectra. Nevertheless we try to measure them separately by looking at some Lick narrowband spectral indices like those related to the Mg and Fe absorption features in the range 5300-5500 Å (i.e., Mgb, Fe5270, F5335, MgFe) We compare our measures with the expectations of Bruzual & Charlot 2003 (BC03) models (Simple Stellar Population SSP, Chabrier IMF) for different metallicities (i.e., Z = $Z_\odot$; Z = 0.4 $Z_\odot$; Z = 0.2 $Z_\odot$; Z = 0.02 $Z_\odot$), as shown in Fig. 3.

The star metallicity is consistent with being 20-40% solar, in particular, expecially from the iron indices Fe5335 and Fe5270 (for which our measures result to have a better accuracy), it is Z = 0.4 $\times$ solar if the age of the star population is 200 Myr, while it is 0.2 $\times$ solar if the age is 300 Myr. This would confirm the picture in which the age is small (less than 400 Myr) and, even if the correlation between age and metallicity is still present, we can constrain the interval between 20-40% solar, consistent with the majority

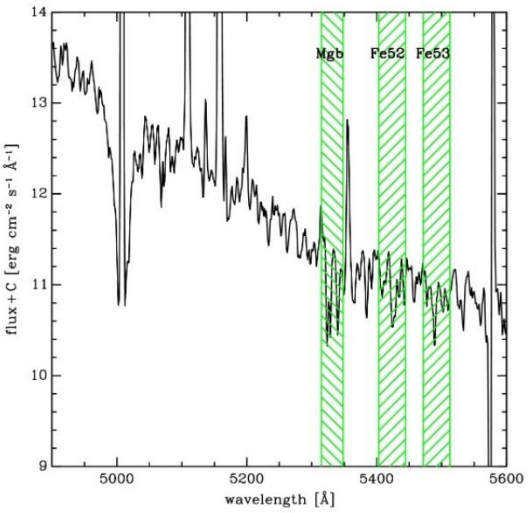

Figure 4. Cartwheel MUSE outer ring spectrum. The green dashed bands mark the spectral regions involved in the metallicity Lick indices which have been estimated in this work.

of the star having been produced in the impact, with a less than solar gas, possibly mixed between the original gas of the Cartwheel and the surrounding environment.

4. Spectro-photometric fitting with MultiNest

Is the timing right? Can we measure the age of the population? Given the age and metallicity correlation, can we disentangle them?

These are amongst the questions we would like to address with the MUSE data, in combination with all other multi-wavelength measures. To this aim, we have adapted the code by Fossati & Mendel (see Fossati *et al.* 2018 on the VESTIGE survey) which exploits a *MULTINEST* fit. It applies a Monte-Carlo Spectro-Photometric Fitter which derives the star formation history (SFH) by fitting high resolution (Bruzual&Charlot) population models. A linear interpolation of the stellar models (where Q_{age} is the look-back time of the event and T_q is the characteristic time scale) is performed, and the result is scaled in luminosity as part of the fitting procedure. The procedure includes nebular emission lines (ionizing radiation absorbed by gas) and dust attenuation.

We collect all the available photometric information in the UV-O-IR band. We select three different spatial regions: the outer ring, the middle zone and the inner (and nuclear) ring. We focus here on the outer ring, in which the majority of the stars should be produced in the impact, and which has a higher brightness, which helps in reducing degrees of freedom to the fitted models. The inner ring has a mix of old and new population which is quite more complicated to simulate with a simple star formation history. The middle zone is fainter a therefore more uncertain, even if very interesting from the point of view of confirming simulations.

We derive photometric points for the outer ring, and extract a MUSE spectrum from the same spatial region, as input to the spectrophotometric fitter. We plot the results for the solar value and for 20% solar - which are the extremes we considered - in Figure 5, where in the bottom left panel: blue indicates the young component, with stellar emission and nebular lines, while red represents the old component (> 10 Myr). The shape of the SFH is a single burst, exponentially quenched. The fitted parameters are the age of the burst ($Q_{age} = 300/132$ Myr) and the quenching scale ($T_q = 69/19$ Myr) for metallicity $Z = Z_\odot$ (top) and $0.2\ Z_\odot$ (bottom) respectively.

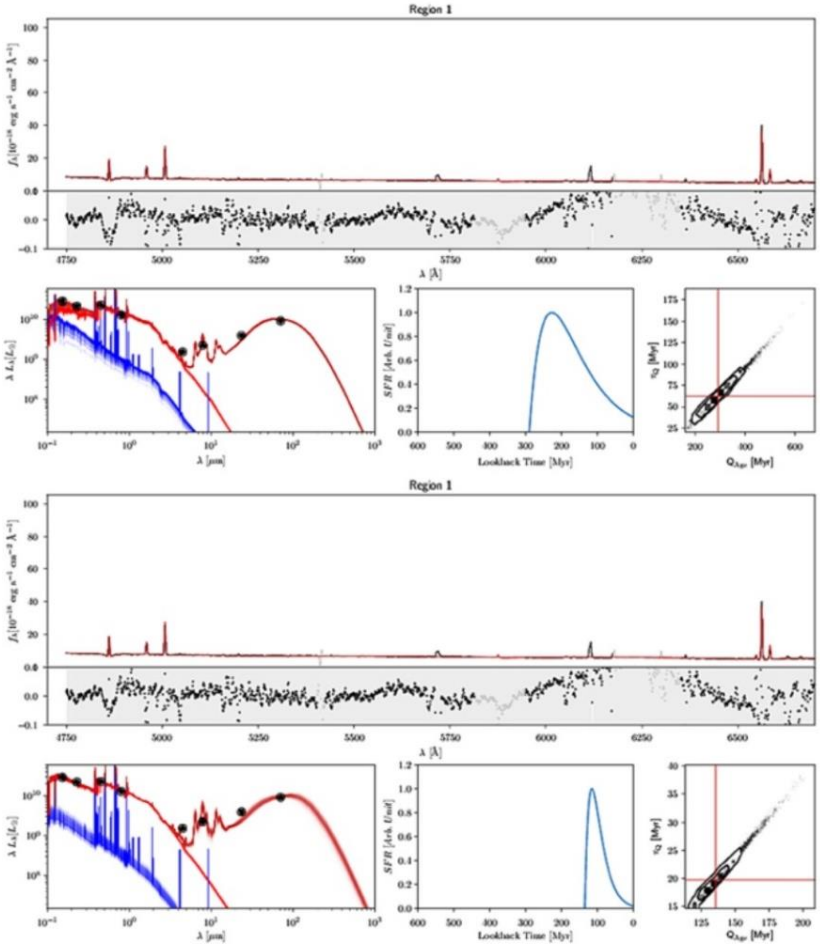

Figure 5. a) *Top figure*: solar metallicity; b) *Bottom figure*: 20% solar metallicity. Both figures are thus structured: *Top*: Results of the MC-SPF fitting for the outer ring. Upper panel: MUSE spectrum (black) and best fit model (dark red). Regions where the spectrum is plotted in grey are not used in the fit. The fit residuals ($Data - Model$) are shown below the spectrum and the grey shaded area shows the 1σ uncertainties. *Lower left panel*: photometric data points in black. The blue line represents the stellar emission with nebular lines from the young component (Age < 10 Myr), the red lines are from the old component (Age > 10 Myr), while the dark red lines are the total model including the dust emission. *Lower middle panel*: reconstructed SFH from the fitting procedure. *Lower right panel*: marginalised likelihood maps for the Q_{age} and T_q fit parameters. The red lines show the median value for each parameter, while the black contours show the 13 σ confidence intervals

5. X-ray band information

One of our aims is to compare the environment properties with the production of ULXs to gather information on the formation mechanism. The first step is to compare the X-ray emission observed by Chandra to the optical one measured by MUSE, as shown in Figure 6. In the same figure, red circles indicate the background objects, easily traceable in the MUSE data cube. No particularly X-ray bright interloper is found in the ring region.

First we investigate if the metallicity is different at the ULXs positions from the rest of the ring. We compute the metallicity by following the prescription of Curti *et al.* 2017,

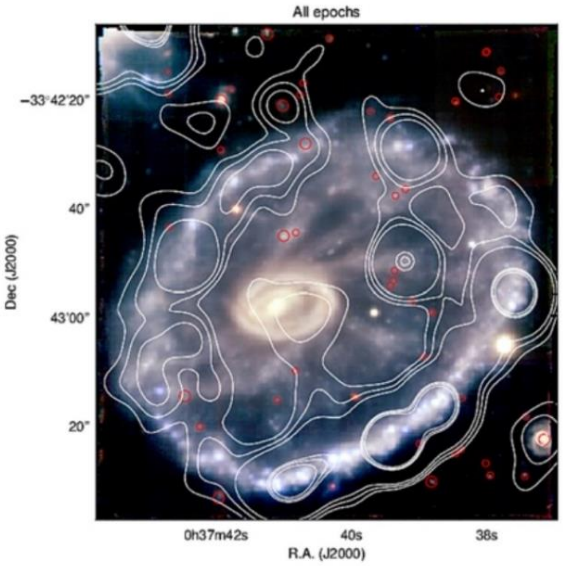

Figure 6. The RGB MUSE image reports the position of the background sources (red circles). The X-ray emission from the Chandra observation (Wolter & Trinchieri 2004) is superposed in white contours.

which calibrate the relation differently for different metallicity ranges, by using the O_3N_2 index defined as: $O_3N_2 = ([OIII]\lambda5007/H_\beta)/([NII])\lambda6584/H_\alpha)$.

We extract the metallicity value at the position of the HII regions listed in (Higdon 1995), and at the ULXs positions from (Wolter & Trinchieri 2004). The range of metallicities - 12 + log(O/H) = 8.16 – 8.47 - is the same for the two samples, indicating that a) a range of values is found even in the ring; b) the ULXs do not occupy a privileged position with respect to the metallicity distribution (see also the contribution by Kouroumpatzakis *et al.*, this volume).

6. Conclusion

ULXs are in the majority binaries, whether NS or BH, produced by a recent episode of Star Formation. The recent construction of XLF for RiGs suggests the presence of a larger number of high luminosity sources in collisional environments. This results may be applicable to constrain estimates for GW events. Galaxies like the Cartwheel represent sizable samples of ULXs and are therefore the most interesting to study. We have exploited the MUSE dataset that allows us to derive spatially resolved information to compare with multi-wavelength data. We find that metallicity is 20-40% solar in the external ring, consistently in both stars and gas, but we cannot exclude yet from our spectrophotometric fitting procedure that the metallicity is solar. From the above results it follows that the age of the stellar population produced in the encounter is $\leqslant 300$ Myr and possibily smaller, consistent with the timing of HMXB formation, which reinforces the interpretation of ULX system as the high luminosity (higher mass transfer? higher magnetic field?) tail of HMXB. ULXs are not found in special regions with respect to the rest of the galaxy, or at least of the ring, for what concerns metallicity. While this point needs to be further studied, it might lessen the importance of the environment for the formation of ULXs and strengthen the importance of the timing of the event.

In the future we plan to perform a detailed comparison with simulations (Renaud *et al.* 2018, Mapelli & Mayer 2012) for different regions of the galaxy; we will exploit available long-slit spectra for determining the ionization parameter and even better calibrate the

metallicity relations. These results will be applied then to constrain formation models of ULXs (e.g. Wiktorowicz *et al.* 2017).

References

Amram, P., Mendes de Oliveira, C., Boulesteix, J. & Balkowski, C., 1998, *A&A*, 330, 881
Bachetti, M. *et al.* 2014, *Nature*, 514, 202
Bruzual, G., & Charlot, S., 2003, *MNRAS*, 344, 1000
Cappellari, M., & Emsellem, E. 2004, *PASP*, 116, 138
Carpano, S., Haberl, F., Maitra, C. & Vasilopoulos, G., 2018, *MNRAS*, 476L, 45
Curti, M., Cresci, G., Mannucci, F., Marconi, A., Maiolino, R., & Esposito, S., *MNRAS*, 465, 1384
Fabbiano, G., 1989, *ARA&A*, 27, 87
Fosbury, R. A. E. & Hawarden, T. G., 1977, *MNRAS*, 178, 473
Fossati, M., *et al.*, *A&A*, 2018, 614, 57
Fürst, F., Walton, D. J., Stern, D., Bachetti, M., Barret, D., Brightman, M., Harrison, F. A. & Rana, V., 2016, *ApJ*, 834, 77
Grimm, H.-J., Gilfanov, M. & Sunyaev, R., 2003, *MNRAS*, 339, 793
Higdon, J. L., 1995, *ApJ*, 455, 524
Higdon, J. L., 1996, *ApJ*, 467, 241
Inoue, T., Tanaka, Y.T., & Isobe, N., 2016, *MNRAS*, 461, 4329
Iovino, A., 2002, *AJ*, 124, 2471
Israel, G. L. *et al.*, 2017a, *MNRAS*, 466L, 48
Israel, G. L. *et al.*, 2017b, *Science*, 355, 817
Kauffmann, G., Heckman, T.M., Tremonti, C., *et al.* 2003, *MNRAS*, 346, 1055
Kewley, L.J., Dopita, M.A., Sutherland, R.S., Heisler, C.A., & Trevena, J. 2001, *ApJ*, 556, 121
Linden, T., Kalogera, V., Sepinsky, J. F., Prestwich, A., Zezas, A. & Gallagher, J. S., 2010, *ApJ*, 725, 1984
Mapelli, M., Colpi, M. & Zampieri, L., 2009, *MNRAS*, 395L, 71
Mapelli, M., Ripamonti, E., Zampieri, L., Colpi, M. & Bressan, A., 2010,*MNRAS*, 408, 234
Mapelli, M. & Mayer, L., *MNRAS*, 420, 1158
Renaud, F. *et al.*, 2018, *MNRAS*, 473, 585
Rich, J.A., Kewley, L.J., & Dopita, M.A. 2011, *ApJ*, 734, 87
Sarzi, M., Falcón-Barroso, J., Davies, R. L., *et al.* 2006, *MNRAS*, 366, 1151
Somers, G., Mathur, S., Martini, P., Watson, L., Grier, C.J. & Ferrarese, L., 2013, *ApJ*, 777, 7
Swartz, D. A., Soria, R., Tennant, A. F. & Yukita, M. *ApJ*, 741, 49
Vazdekis, A., Sánchez-Blázquez, P., Falcón-Barroso, J., *et al.* 2010, *MNRAS*, 404, 1639
Wiktorowicz, G., Sobolewska, M. , Lasota, J.-P. & Belczynski, K., 2017, *ApJ*, 846, 17
Wolter, A. & Trinchieri, G, *A&A*, 426, 787
Wolter, A., Esposito, P., Mapelli, M., Pizzolato, F. & Ripamonti, E., 2015, *MNRAS*, 448, 781
Wolter, A., Fruscione, A. & Mapelli, M., 2018 *ApJ*, 863, 43
Wolter, A., Consolandi, G., Longhetti, M., Landoni, M. & Bianco, A., in preparation
Zezas, A., Fabbiano, G., Baldi, A., Schweizer, F., King, A. R., Rots, A. H. & Ponman, T. J., *ApJ*, 661, 135

Discussion

Indulekha Kavila: Your see misalignment between ULXs and the HII regions. Since there is a time gap between the star formation event and the appearance of the ULX, wouldn't it be more apt to look for alignment with signatures of B stars - which are the brightest objects in the "post star formation event" phase?

Wolter: We have checked for offsets between the location of the peak of the optical emission and the ULX number density, with no particular selection of emission signatures.

Claus Leitherer: One additional step would be to apply population synthesis models with binary star evolution (BPASS; Eldridge *et al.* 2017). This would allow you to model the optical and X-ray data simultaneously and check for consistency.

Wolter: We thank you for the suggestion and we will try to implement this for the next publication.

附　录 B 文献翻译

以车轮星系为基础的双星形成过程

超亮 X 射线源（ULX）是恒星演化的终点。它们大多被解释为伴星质量较大的双星系统。它们也是 BH-BH 最有可能的前身，甚至是 BH-NS 合并的前身。ULX 的轨道参量仍然未知，还需要更多的研究来确定，特别是与环境的金属丰度之间的联系，这种关系经常被提及，但没有得到强有力的证明。我们通过使用车轮（Carthweel）星系的 MUSE DEEP 马赛克并应用了蒙特卡罗代码（Monte Carlo Code）来共同解决光谱学和光度学问题，从而证明了这个问题。我们通过构建空间分辨的发射谱线比图和 BPT 诊断图来测量星系中和 X 射线源位置的发射气体金属丰度。该车轮星系是原型环星系并且新的恒星群体的形成时间和位置比正常的星系更容易构建。ULX 数量在这个星系中最多（在钱德拉（Chandra）和 XMM-Newton 数据中有 16 个来源被分类为 ULX）。因此，车轮星系是研究恒星形成（恒星形成率和恒星形成历史）与 ULX 数量及其最终演化状态关系的理想实验平台。我们发现，外环中恒星种群的年龄与在撞击中产生的时间（300 Myr（3 亿年））相一致，并且即使发现大部分为亚太阳金属丰度，即使太阳金属丰度的假设也可行，并且与一些观测到的特性相符。关于车轮星系的这些发现将会在进一步的双星形成模型和演化路径中被检验。

关 键 字：恒星：双星，星系：单个（车轮），星系：特有的，星系：相互作用，星系：进化

引言

为什么我们选择车轮星系？车轮星系是环形星系（RiGs）的一个缩影，其中在星系演化终点诞生了很多 ULXs。我们展示了（见后文）ULX 大致就是高质量 X 射线双星（HMXB，另见这册的 Roberts 或者 Kovlakas 的部分）。他们是近期一些事件的证据，例如两个星系的引力并合。在 RIGs 中，因为新产生的恒星种群比旋涡中的具有更加简单的几何和动力学特征，所以他们的位置和产生时间更好重构。更亮的 ULX 似乎更容易在低金属丰度的环境中找到。两种可选原因已经被提出来：（a）最大的黑洞（BH）直接吸积了一些低金属丰度的恒星（例如： Mapelli et al. 2009[21]），（b）低金属丰度的 X 射线双星比高金属丰度的更加亮[20]。这对于黑洞和中子星都有可能。

车轮星系是属于一个 122Mpc 以外的 4 个致密团体中的一个[15]。和这团体中其他星系相撞的冲击波引发了一系列的恒星形成以及各个波段的辐射。这种恒星形成的一个结果就是大量的 ULX 被发现了[32]。

近期的引力波探测引起了人们对于 ULX 可能作为合并遗迹的兴趣。许多研究者已经用 ULX 作为先导来计算不同种类并合引起的可能的引力波探测，尤其是对于中子星黑洞这种还没有被探测到的情况。许多最近的概率估算已经把 ULX 的性质[14]（如光度函数，活跃时间，对于星系质量的频率以及恒星形成率）考虑在内。然而，许多参数还是未知的或者不确定的。

我们用了对于 ULX 最合适的定义：银河系外的，点状的，不涉及原子能的光度范围在 10^{39}~$10^{42} erg/s$的 X 射线源[7]。这种定义是为了创造一个多元的源的种类并且包括了其他闯入者，

例如活跃的星系核和至少超新星的一个分支，预计占 25%的 ULX[28]。ULX 的主要成分仍旧被认为是带有演化终点主星和一个巨大伴星（在大多数情况下）的双星系统。这种系统的主星可能是：（a）一个中等质量黑洞（10^2~10^5太阳质量-这是最初的一些猜测，但是最近不流行了）（b）一个重的黑洞（30~100 太阳质量）或者（c）一个中子星-这个已经被证实有五个例子了[2][16][17][10][5]。

ULX 的光度函数

开始我们用光度函数（XLF）来展示 ULX 和 HMXB 的联系，这也是本文的主旨，因此也需要足够的重视。很多学者，包括我们自己，已经做出了对于个别有大量 ULX 星系的 XLF，并且把它和所谓的 HMXB 的宇宙光度函数相比较[11]。XLF 用恒星生成率（SFR）来归一化。恒星生成率是用$H\alpha$的光度来计算的。这种比较和一些关于 ULX 和最近的恒星形成爆发有关的意见相符。对于低光度源在 XLF 上平滑的连接和斜率也与我们的假设相符。

这也被大量的在 Chandra 观测到的七个碰撞 RiG 星系和近邻星系中 ULX 的 XLF 证实[33]。他们也产出了相似数目的 ULX 并且结果相互匹配[28]，即使 RiG 在高光度有可能超界。多个星系的组合依赖于我们分别见证在不同星系独立的恒星形成爆发并且时间很短（大约少于 100Myr，与 HMXB 的形成时间相近[24]）的假设。并且还要假设金属丰度之间的差距不会过大。在任何情况下，金属丰度的影响相对于 SFR 并不占主导作用[22]。

带有 65 个环形星系中 15 个源的车轮星系是最好的检测 ULX 和 HMXB 大致形成环境和演化路径的目标。对于车轮星系的金属丰度的测量在一些文献中都有涉猎。在最亮的 HII 区域测量的。恒星爆发的年龄还是未知，即使一些相撞的年龄估算已经在部分文献中给出了[8]。Higdon (Higdon 1996)[13]通过 HI 速度空间预测距离相撞有 300Myr；Amram et al. 1998[1]通过$H\alpha$的运动学分析（13~30km/s 的范围）预测星系年龄大于 200Myr；Renaud et al. 2018[24]通过详细的模拟计算得到星系的存在时间小于 100Myr。

我们因此想要研究车轮星系来解决这些问题。

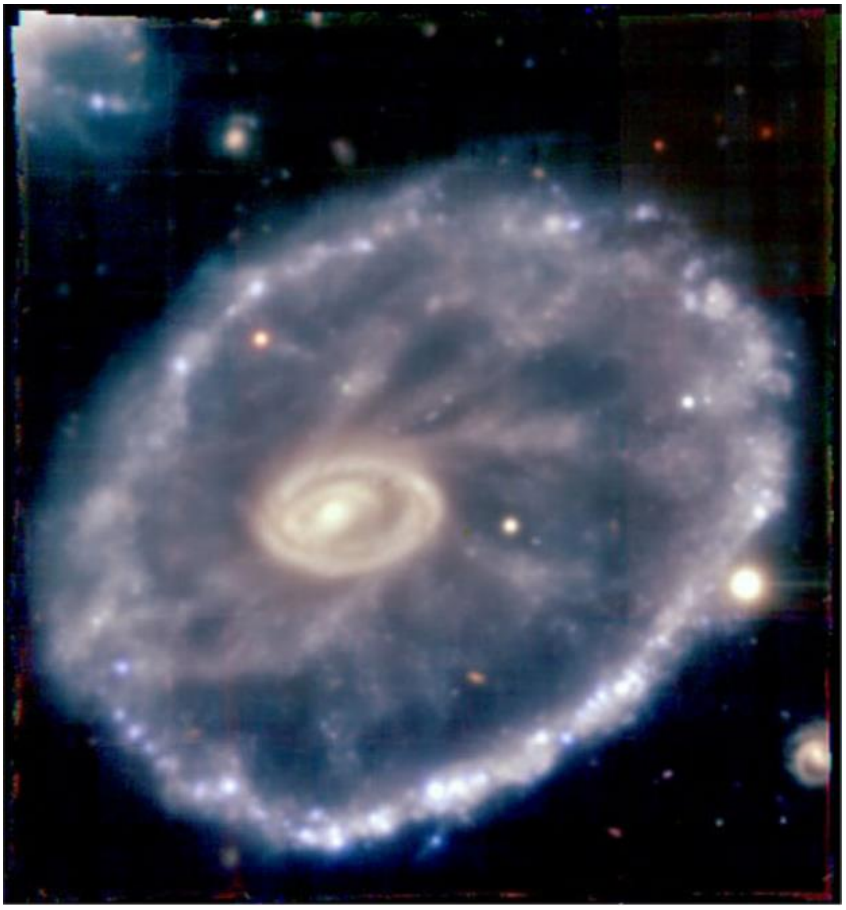

图 1 采用尽可能贴近 g, i and r Gunn 的过滤器，从 MUSE 数据中得到的彩色照片

MUSE 数据

车轮星系被 MUSE 在 2014 年八月观测到，用四个广度为 4ksec 的像素点校准，其中包括了整个星系（1.4×1.5弧分）。数据已经从 ESO 档案中下载。MUSE 3D 科学档案集已经将仪器特征误差消除，并且用 MUSE 版本 1.4 以上的处理软件做了天文测量上的矫正，背景消除，波长和 flux（单位立体角接受到的信号强度）矫正[34]。

为了大致估测辐射线的 flux，我们认为经历巴尔默辐射线的恒星的吸收仍旧在 MUSE 的观测光谱范围内：$H\alpha$和$H\beta$。针对此种情况，在独立像素点满足$S/N > 5$时，我们用被修正点扩散[4]的 GANDALF 软件[26]来建立星际连续谱线的模型。星际的连续性是用 MILES 数据库的模板通过恒星视向速度分布的卷积完成的。这里我们采用了发射线和动量为高斯分布的模型。在每个像素点上，从模型中的恒星连续光谱去除了观测到的光谱来得到一个最终的仅含辐射的数据库[29]，从而避免了星际吸收的干扰。

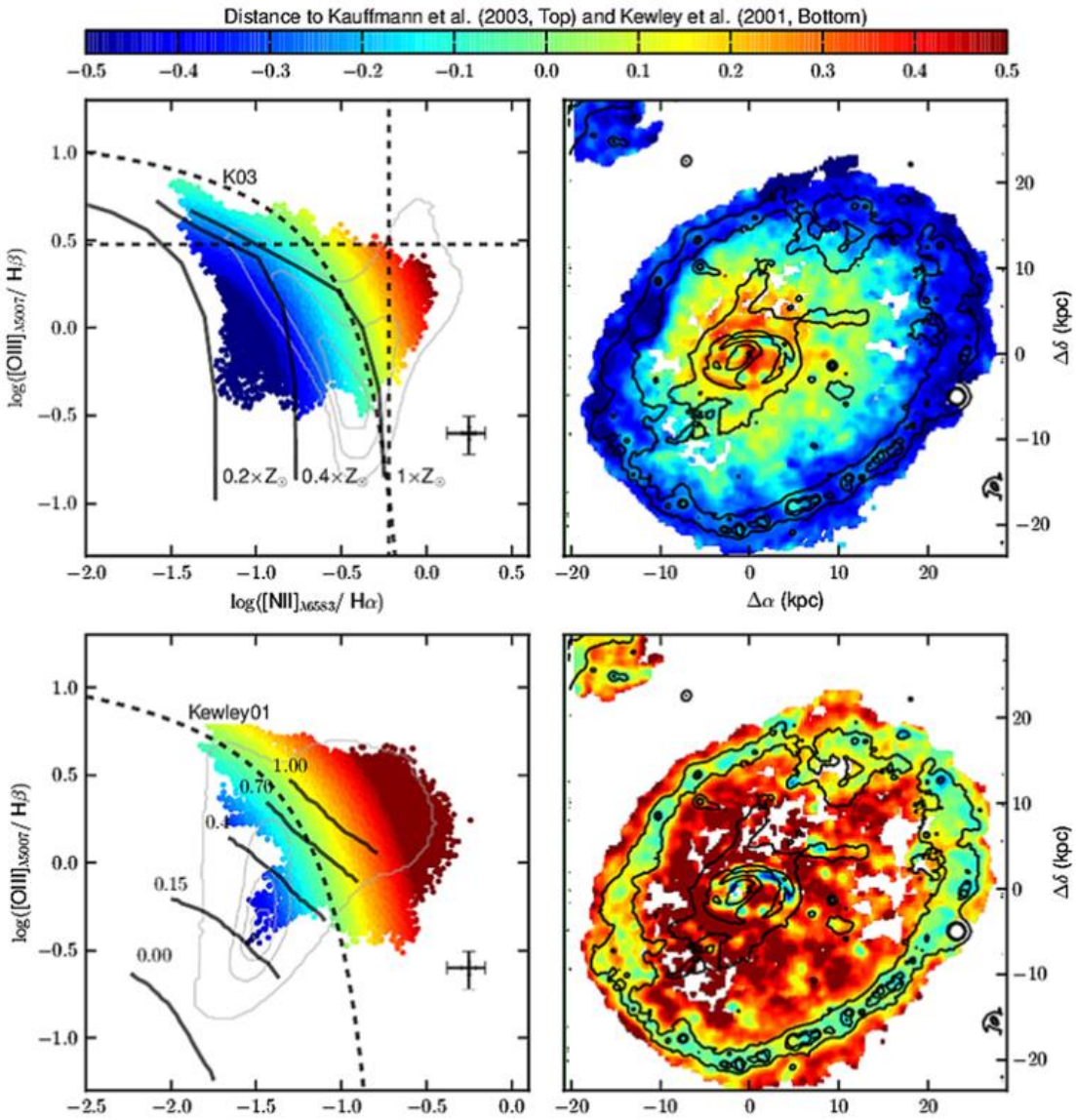

图表 2 BTP 图表：详情见文中。左上：[OIII]λ5007/Hβ **和**[NII]λ6583/Hα**，右上：**BPT **观测的空间像素分布，颜色同左上。左下：**[OIII]λ5007/Hβ **和**[OI]λ6300/Hα**。右下：**BPT **观测的空间像素分布，颜色同左下。

金属丰度

我们提取了“谱线”的照片（对于 Hα, Hβ, [OIII], [OI] 和[NII]）。我们可以用这些照片来计算根据空间像素的分类模型的标准，如同在图表 2 中两个 BTP 分析图。在左上方[OIII]λ5007/Hβ 和[NII]λ6583/Hα 被画出。虚线按照 Kauffmann et al. 2003 (Ka03)[18]把 AGN 和 HII 两个区域分离开来。根据他们最小的和 Ka03 的距离，右上方的数据被涂上颜色。黑色的十字表示相对于辐射线的误差在S/N~15/5下。粗黑线根据 Kewley et al. (2001)[19]展示了三个不同的光致电离模型在不同金属丰度下（0.2，0.4 和 1 倍太阳金属丰度）。

在左下角[OIII]λ5007/Hβ 和[OI]λ6300/Hα 被画出来。虚的曲线根据 Kewley et al. 2001 (Ke01)[19]把 AGN 和 HII 两个区域分离开来。黑色的十字表示相对于辐射线的误差在S/N~15/5下。粗黑线根据 Rich et al. 2011[25]展示了五个不同的由于冲击造成的$H\alpha$的 flux 占比（从 0 到 1）。

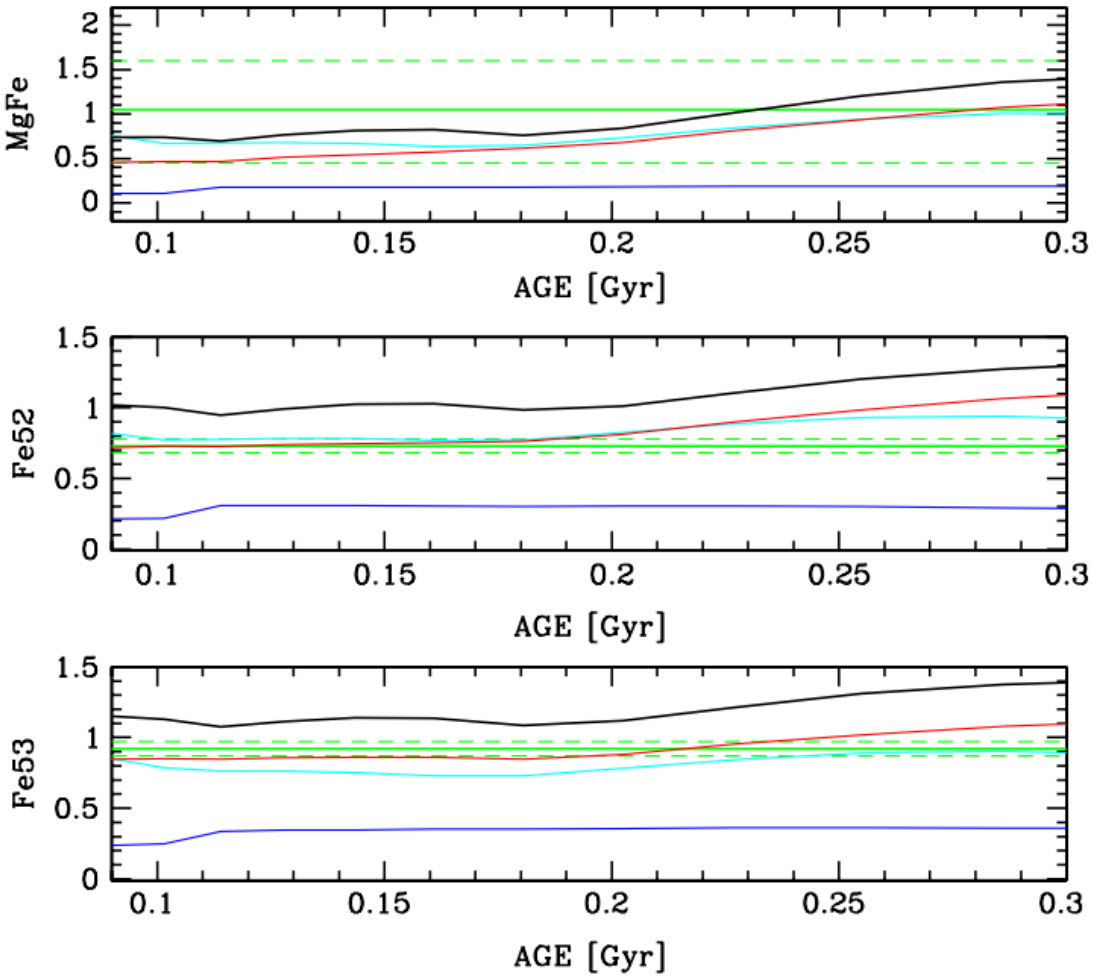

图表 3 BC03 模型预测和 MgFe（上方），Fe5270（中间）与 Fe5335（下方）模型的比较。这展示了对于车轮星系外部环光谱的测量。绿线表示我们的测量（实线）和误差（短虚线）。在不同的图中，根据关于 SSP 年龄的预测的指数如图所示。其中金属丰度分别为 1 倍（黑线），0.4 倍（红线），0.2 倍（蓝绿线）和 0.02 倍（蓝线）金属丰度。

一个基本的关于星系金属丰度的讨论展示了环形星系的金属丰度基本上比其他星系的要低。G1 的在左上角看到的一小部分展示了和环形星系一样的金属丰度。中间显示出 超太阳金属丰度。然而，像下方用【OI】代替【NII】的图表展示的那样，我们不能排除冲击波的存在，因为他们对谱线的贡献比例有贡献。

图谱和推断

恒星的金属性和星系年龄对于光学谱线的影响是相似的，这一点已经被广泛认同。然而我们已经尝试通过观测一些 Lick 窄频带的光谱去分别测量他们，就像那些在 5300-5500 埃关于 Mg 和 Fe 的吸收特征（例如：Mgb，Fe5270,F5335，MgFe）一样。如图表 3 所示，我们比较了我们的测量和 Bruzual & Charlot 2003 (BC03)[3]模型针对不同金属丰度（例如 Z = Z⊙; Z = 0.4 Z⊙; Z = 0.2 Z⊙; Z = 0.02 Z⊙）的预测（简单的恒星种群模型，采用 Chabrier 的初始质量函数（IMF））。

恒星金属丰度一直保持在 20~40%太阳金属丰度左右，尤其是从铁的吸收线 Fe5335 和 Fe5270（我们针对这些有更高的精确度），如果恒星演化时间是 200Myr，这是 0.4 太阳金属丰度。同样的，

如果演化时间为 300Myr，金属丰度为 0.2 太阳的。这可以证明这是年轻的星系（至少小于 400Myr）并且即使年龄和金属丰度的联系仍然存在，我们可以强制范围间距为 20~40%，这样可以与大多数撞击产生的星相匹配。其中包括低于太阳金属丰度的气体，还可能混有介于原始车轮星系和周围环境之间的气体。

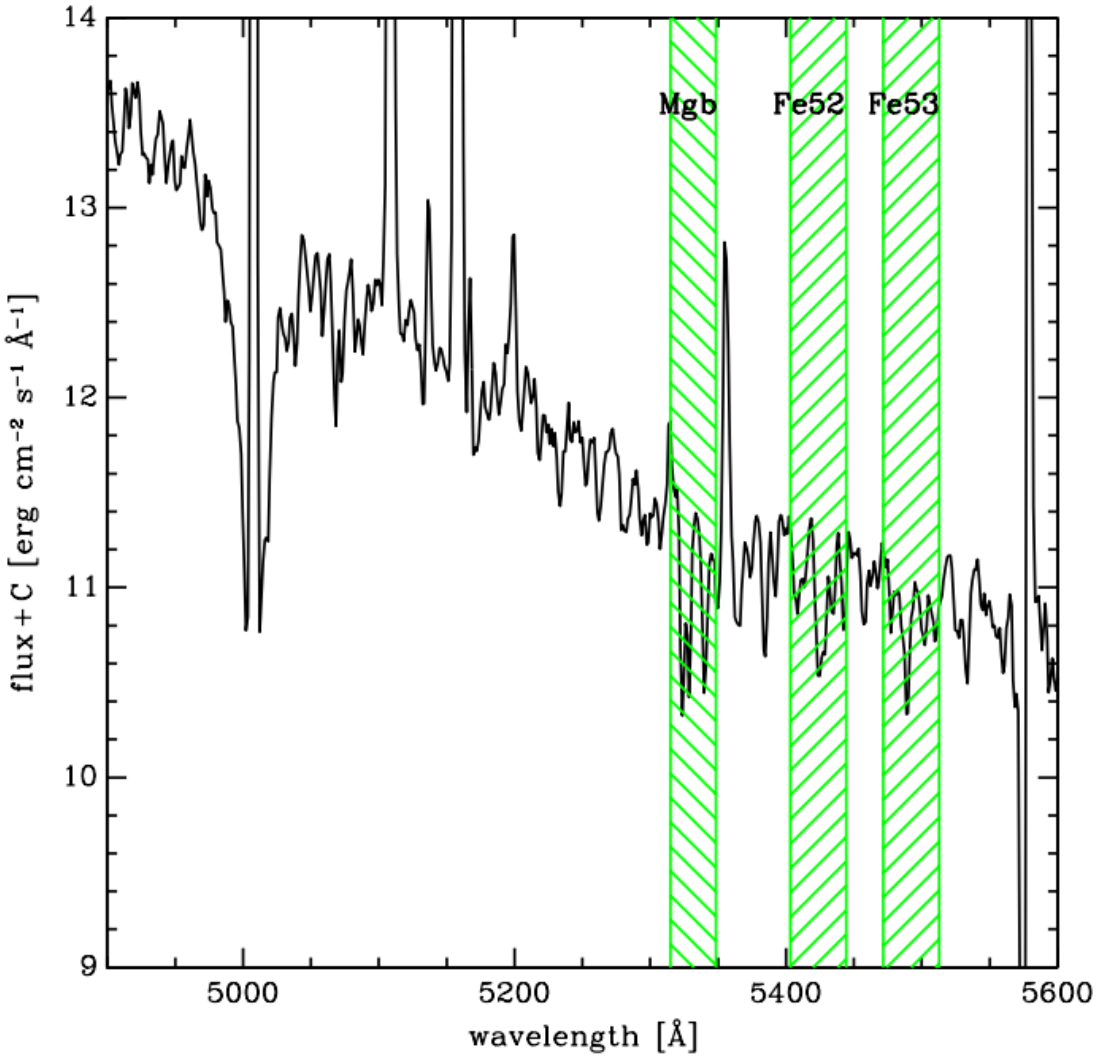

图表 4　MUSE 观测的车轮星系外部的光谱。绿色虚线标志了本文中估算的参与 Lick 修正的光谱区域

用 MultiNest 进行光谱光度测量拟合

时间频率是准确的吗？我们能测量星族的年龄吗？给出了年龄和金属丰度的关系，我们能分离他们吗？

我们要结合其他各个波段的测量关注 MUSE 数据来回答这些问题。为达此目的，我们采用了 Fossati & Mendel[9]的程序，他们应用蒙特卡洛光谱光度拟合开发了 MULTINEST 拟合工具。此工具可以根据高精度的拟合种群模型得出恒星生成历史（SFH）。采用对恒星模型线性插值的方法（Q_{age}是此事件前的时间跨度，T_q是典型的时间跨度），作为程序一部分，最终结果根据光度进行挑选。此程序包括了星云的辐射线（气体吸收的电离辐射）和星际尘埃的干扰。

我们手机了所有在 UV-O-IR 波段光度测定的信息。我们筛选了三个不同的光谱区域，外部环，中间区域和内部（产生核反应的）环。我们这里主要关注外部环，因为大部分恒星是由于相撞产生的，此处也具有更高的亮度，这也就帮祝我们减少了模拟参数空间的维数。内部环是由老的和新的族群共同构成的，用简单的恒星演化历史来模拟很棘手，即使从验证模拟结果的角度来说十分有意义。

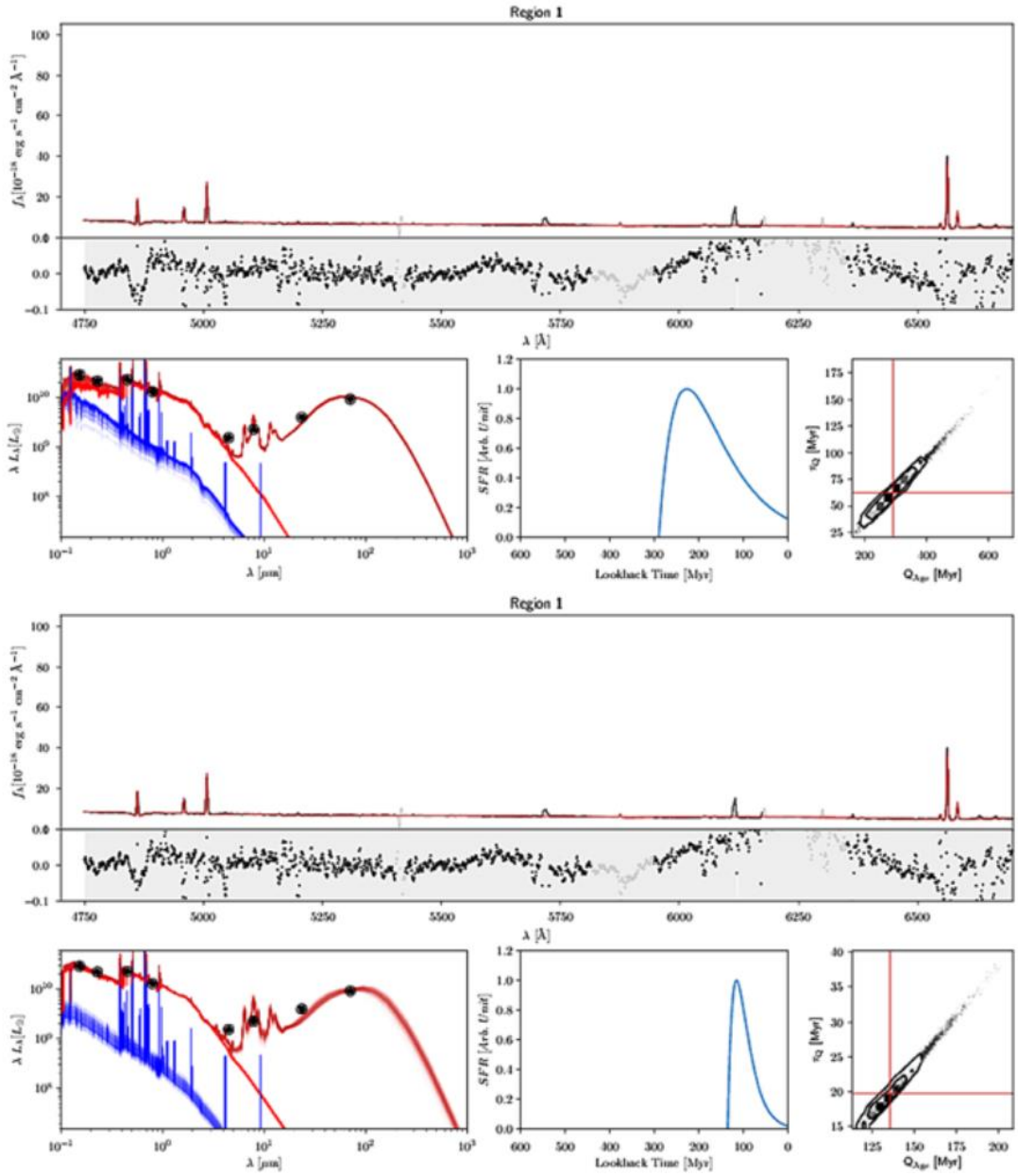

图表 5（a）上图：太阳金属丰度；（b）下图：20%太阳金属丰度。两个图的编排：上图：MC-SPF 的结果针对于外部星系。上部分：MUSE 的光谱（黑色）和最佳拟合模型（红黑色）。光谱画出的区域为灰色的并没有用于拟合。拟合的差值（数据-模型）在光谱下面显示，灰色阴影区域展示了 1σ的不确定度。下图：光度数据用黑色标出。蓝线代表了在一些年轻的伴星中（年龄<10Myr》）星际间中星云线的辐射。红线代表在老的伴星中（年龄>10Myr）。红黑线是包括尘埃辐射的总的模型。下图中间：通过拟合程序重构的恒星生成历史，下图右方：对Q_{age}和T_q边缘拟合的参数。红线代表着不同参数的中间值，黑色等高线展示了 13σ的置信区间。

我们针对外部环形得到了光度的点，并且分离了 MUSE 光谱的数据从相同的空间区域。把它们作为输入给程序。我们在图表 5 画出了 20%太阳金属丰度的结果。底部左侧：蓝色代表年轻的

伴星带有星际辐射和星云谱线；红色代表老的伴星（>10Myr）。SFH 的形状是单个的爆发，以指数衰减的形式结束。拟合参数是爆发的年龄（$Q_{age} = 300/132Myr$）和结束时长（$T_q = 69/19Myr$）分别对于 Z=Z⊙ (上方) and 0.2 Z⊙（下方）。

X 射线波段信息

我们其中一个目标就是比较产生 ULX 的环境特征来收集更多关于恒星形成机制的信息。第一步就是比较 Chandra 观测到的 X 射线辐射和光学波段 MUSE 的观测，如图表 6。在同一个图上，红圈表示了背景的源，通过 MUSE 数据库可以轻松获取。在这个区域内，没有特别的 X 射线源闯入被发现。

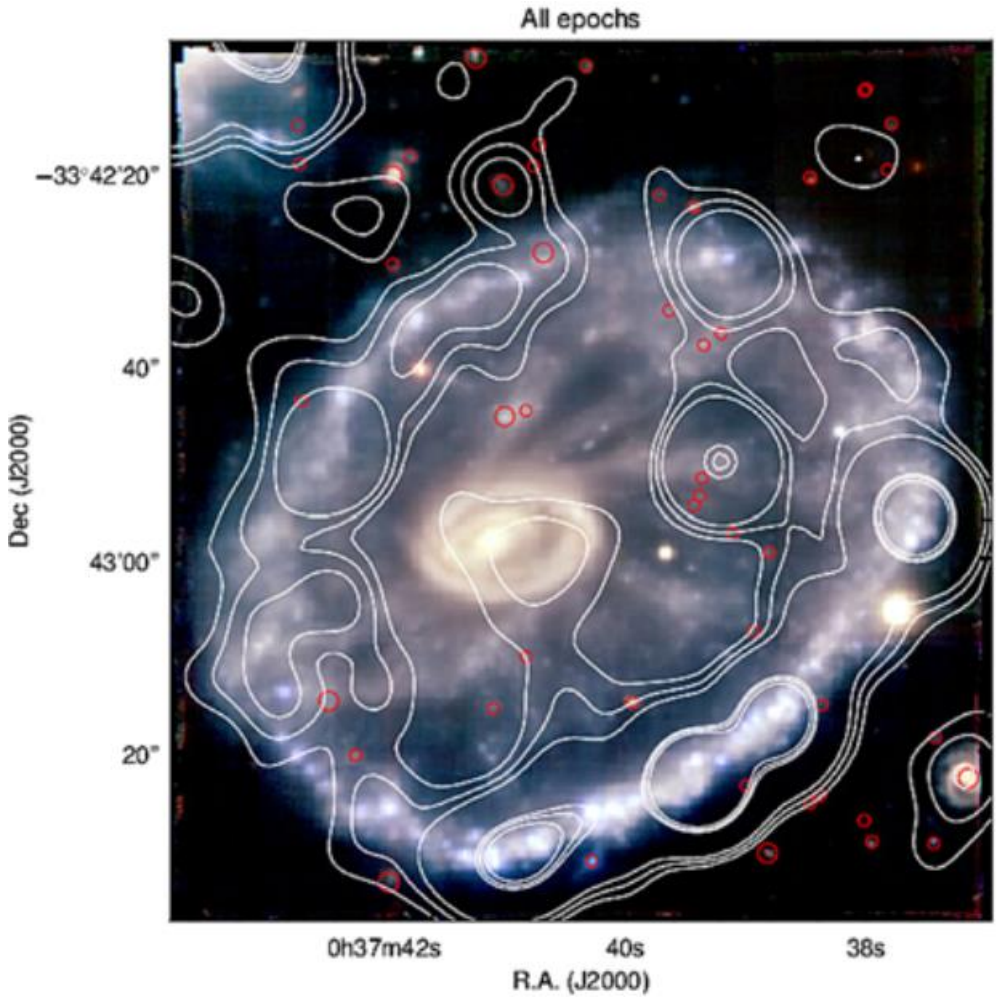

图表 6 MUSE 观测的 RGB 图片，显示了背景源的位置（红圈）。Chandra 观测的 X 射线辐射是在白色的等高线上表示

开始我们调查了环形其他区域不同位置 ULX 中金属丰度的不同。我们通过下面的指示[6]计算了金属丰度并标定了针对不同金属丰度范围的联系，采用O_3N_2指数，其被定义为$O_3N_2 = ([\mathrm{OIII}]\lambda5007/\mathrm{H}\beta)/([\mathrm{NII}])\lambda6584/\mathrm{H}\alpha)$。

我们提取了在(Higdon 1995)[12]列出的 HII 区域的金属丰度和在 Wolter & Trinchieri 2004[31]的 ULX 的位置。金属丰度范围为 12 + log(O/H) = 8.16 – 8.47 和两个例子都相等，预示了（a）即使在环中金属丰度范围也成立；（b）ULX 不占据一个特殊的金属丰度范围的位置。

总结

不管是黑洞还是中子星，ULX 是主要由最近的恒星形成的。近年来的对于 XLF 的研究显示了在碰撞的环境中大量的高亮度源。这个结果可能对于模拟引力波事件有借鉴作用。像车轮星系这种代表了许多 ULX 的样本因此成为研究热点。我们利用 MUSE 数据来进行空间上的分析进而比较多个波段的数据。我们发现在环外部 20%~40%太阳金属丰度，对于恒星和气体都适用。通过上述的结果，碰撞后产生的恒星的年龄也小于 300Myr 或者更小，与 HMXB 的形成时间相符合，进一步证明了 ULX 是高亮度的 HMXB 演化末期假说（或者高物质传输率？强磁场？）。根据金属丰度的测量，ULX 没有被发现在一些特殊的区域相对于星系的其他位置，或者至少属于星系内。这点需要进一步研究，这可能减少了 ULX 形成环境的限制并且加强了碰撞发生时间的重要性。

在未来我们计划进行一个针对不同区域星系的详细模拟[23][24]的比较；我们会开发出长切口的光谱来决定离子化的参数并且更好的校准金属丰度之间的关系。这些结果也会被用于构建 ULX 的形成模型[30]。

参考文献：

[1]. Amram, P., Mendes de Oliveira, C., Boulesteix, J. & Balkowski, C., 1998, *A&A*, 330, 881
[2]. Bachetti, M. *et al.* 2014, *Nature*, 514, 202
[3]. Bruzual, G., & Charlot, S., 2003, *MNRAS*, 344, 1000
[4]. Cappellari, M., & Emsellem, E. 2004, *PASP*, 116, 138
[5]. Carpano, S., Haberl, F., Maitra, C. & Vasilopoulos, G., 2018, *MNRAS*, 476L, 45
[6]. Curti, M., Cresci, G., Mannucci, F., Marconi, A., Maiolino, R., & Esposito, S., *MNRAS*, 465, 1384
[7]. Fabbiano, G., 1989, *ARA&A*, 27, 87
[8]. Fosbury, R. A. E. & Hawarden, T. G., 1977, *MNRAS*, 178, 473
[9]. Fossati, M., *et al.*, *A&A*, 2018, 614, 57
[10]. F¨urst, F., Walton, D. J., Stern, D., Bachetti, M., Barret, D., Brightman, M., Harrison, F. A. & Rana, V., 2016, *ApJ*, 834, 77
[11]. Grimm, H.-J., Gilfanov, M. & Sunyaev, R., 2003, *MNRAS*, 339, 793
[12]. Higdon, J. L., 1995, *ApJ*, 455, 524
[13]. Higdon, J. L., 1996, *ApJ*, 467, 241
[14]. Inoue, T., Tanaka, Y.T., & Isobe, N., 2016, *MNRAS*, 461, 4329
[15]. Iovino, A., 2002, *AJ*, 124, 2471
[16]. Israel, G. L. *et al.*, 2017a, *MNRAS*, 466L, 48
[17]. Israel, G. L. *et al.*, 2017b, *Science*, 355, 817
[18]. Kauffmann, G., Heckman, T.M., Tremonti, C., *et al.* 2003, *MNRAS*, 346, 1055
[19]. Kewley, L.J., Dopita, M.A., Sutherland, R.S., Heisler, C.A., & Trevena, J. 2001, *ApJ*, 556, 121
[20]. Linden, T., Kalogera, V., Sepinsky, J. F., Prestwich, A., Zezas, A. & Gallagher, J. S., 2010, *ApJ*, 725, 1984
[21]. Mapelli, M., Colpi, M. & Zampieri, L., 2009, *MNRAS*, 395L, 71
[22]. Mapelli, M., Ripamonti, E., Zampieri, L., Colpi, M. & Bressan, A., 2010,*MNRAS*, 408, 234
[23]. Mapelli, M. & Mayer, L., *MNRAS*, 420, 1158
[24]. Renaud, F. *et al.*, 2018, *MNRAS*, 473, 585
[25]. Rich, J.A., Kewley, L.J., & Dopita, M.A. 2011, *ApJ*, 734, 87
[26]. Sarzi, M., Falc´on-Barroso, J., Davies, R. L., *et al.* 2006, *MNRAS*, 366, 1151
[27]. Somers, G., Mathur, S., Martini, P., Watson, L., Grier, C.J. & Ferrarese, L., 2013, *ApJ*, 777, 7
[28]. Swartz, D. A., Soria, R., Tennant, A. F. & Yukita, M. *ApJ*, 741, 49
[29]. Vazdekis, A., S´anchez-Bl´azquez, P., Falc´on-Barroso, J., *et al.* 2010, *MNRAS*, 404, 1639
[30]. Wiktorowicz, G., Sobolewska, M. , Lasota, J.-P. & Belczynski, K., 2017, *ApJ*, 846, 17
[31]. Wolter, A. & Trinchieri, G, *A&A*, 426, 787
[32]. Wolter, A., Esposito, P., Mapelli, M., Pizzolato, F. & Ripamonti, E., 2015, *MNRAS*, 448, 781
[33]. Wolter, A., Fruscione, A. & Mapelli, M., 2018 *ApJ*, 863, 43
[34]. Wolter, A., Consolandi, G., Longhetti, M., Landoni, M. & Bianco, A., in preparation

附 录C 中子星ULX论文

A&A 649, L2 (2021)
https://doi.org/10.1051/0004-6361/202140792

Astronomy & Astrophysics

LETTER TO THE EDITOR

Population synthesis on ultra-luminous X-ray sources with an accreting neutron star: Wind Roche-lobe overflow cases

Zhao-Yu Zuo, Hao-Tian Song, and Han-Chen Xue

School of Physics, Xi'an Jiaotong University, Xi'an 710049, PR China
e-mail: zuozyu@xjtu.edu.cn

Received 12 March 2021 / Accepted 16 April 2021

ABSTRACT

Very recently, wind Roche-lobe overflow (WRLOF) has been suggested as a possible mass transfer mechanism for ultra-luminous X-ray sources (ULXs) and, to date, two neutron-star (NS) ULXs (i.e., NGC 7793 P13 and NGC 300 ULX-1) are remarkable and hard to understand in the current, usual RLOF picture. In this work, we test if the two sources could fit into the WRLOF paradigm. By using an evolutionary population synthesis method, we modeled the population of NS ULXs with (super)giant donors, taking the WRLOF accretion mode into account. We find that the population of wind-fed NS ULXs in the WRLOF mode is distinct in numbers and binary parameters from that in the traditional Bondi-Hoyle-Lyttleton mode, and it is strongly metallicity dependent. The number of NS ULXs with (super)giant donors can be enhanced greatly, by one or two orders of magnitude, depending on the metallicity adopted. Sources with massive ($\sim$15−40 $M_\odot$) (super)giant donors dominate wind-fed NS ULXs in the very low metallicities, while sources in near solar cases are dominated by a red supergiant with a lower mass $M_2 < 10\,M_\odot$ instead. Moreover, the two NS ULXs can be well reproduced in the WRLOF paradigm, which significantly enriches our understanding of the nature of ULXs and the population. We also present the current distributions of binary parameters of wind-fed NS ULXs, which may be further testified by future high-resolution optical and X-ray observations of these populations.

Key words. stars: evolution – X-rays: binaries – stars: neutron – methods: statistical – binaries: close

1. Introduction

Ultraluminous X-ray sources (ULXs) are non-nuclear, point-like objects with apparent luminosities of $L_X > 10^{39}$ erg s^{-1}, exceeding the Eddington limit for a 10 $M_\odot$ black hole (BH, Fabbiano 1989, see Kaaret et al. 2017 for a recent review). Although suggested to be intermediate mass (10^2−10^5 $M_\odot$) BHs (Colbert & Mushotzky 1999) in early studies as the accretor in ULXs, growing pieces of evidence (Gladstone et al. 2009; Liu et al. 2013; Sutton et al. 2013; Walton et al. 2018) demonstrate that most if not all ULXs are instead stellar-mass binary systems, proposed due to super-Eddington accretion (Begelman 2002) and/or geometric beaming (King et al. 2001; Poutanen et al. 2007; King 2008; King & Lasota 2020). Strikingly, ULXs can also harbor an accreting neutron star (NS), of which the Eddington limit $L_{\rm Edd}$ is much lower (i.e., around 2×10^{38} erg s^{-1} for a 1.4 $M_\odot$ NS[1]). Several NS ULXs have been identified so far and they are characterized by regular pulses with periods of $\sim$1 s, that is, M 82 X-2 (Bachetti et al. 2014), NGC 7793 P13 (Fürst et al. 2016, 2018; Israel et al. 2017a; Motch et al. 2014), NGC 5907 ULX1 (Israel et al. 2017b), NGC 300 ULX1 (Carpano et al. 2018; Heida et al. 2019b), NGC 1313 ULX-2 (Sathyaprakash et al. 2019), and M 51 ULX-7 (Rodríguez Castillo et al. 2020), or a cyclotron resonance feature, for example, M 51 ULX8 (Brightman et al. 2018).

In order to account for the ultra-high luminosity of NS ULXs, mass transfer through Roche-lobe overflow (RLOF) via an accretion disk has always been assumed in previous theoretical studies (Shao & Li 2015; Fragos et al. 2015; Wiktorowicz et al. 2015, 2017, 2019), as a highly super-Eddington mass transfer rate is unlikely to reach through stellar wind. For example, after the discovery of the first NS ULX (i.e., M 82 X-2, Bachetti et al. 2014), Shao & Li (2015) first studied the population of NS ULXs by the use of both evolutionary population synthesis (EPS) and a detailed binary evolution method. They suggest that NS ULXs may contribute significantly to the whole ULX population. And the distribution of the NS ULX population was demonstrated in the donor mass-orbital period plane (see their Figs. 3 and 4), as well. Utilizing the StarTrack EPS code, Wiktorowicz et al. (2017) show that the typical donor of NS ULXs is a red giant star with a mass of $\sim$1.0 $M_\odot$. They found that massive supergiant donors are rare (<1%) in their calculations. Interestingly, several massive stars have already been detected in the optical and infrared as potential donors for ULXs (Kaaret et al. 2004; Liu et al. 2004, 2013; Heida et al. 2014, 2015, 2016; Villar et al. 2016; Lau et al. 2019). Among them, two NS ULXs are remarkable and hard to understand in the current, usual RLOF picture (Shao & Li 2015; Wiktorowicz et al. 2017). One is NGC 7793 P13 (hereafter P13; Motch et al. 2014; Fürst et al. 2018), which is a pulsing ULX with a blue supergiant (B9Ia) of 18−23 $M_\odot$ in a long orbital period of about 64 d. Another is the pulsing ULX source NGC 300 ULX-1 (Carpano et al. 2018; Heida et al. 2019b), with a red supergiant (RSG) donor ($T_{\rm eff}$ = 3650−3900 K and $\log(L_{\rm bol}/L_\odot)$ = 4.25 ± 0.10, Heida et al. 2019a).

[1] In the case of a strong magnetic field, the effective Eddington luminosity of NS can be increased by a factor of $(\mu_{\rm B}/\mu)^2$ for frequency μ below cyclotron ($\mu_{\rm B}$) due to the reduction of the electron-scattering cross-section (Dall'Osso et al. 2016; Ekşi et al. 2015; Tong 2015).

Very recently, wind Roche-lobe overflow (WRLOF, first introduced by Podsiadlowski & Mohamed 2007; Mohamed & Podsiadlowski 2007 has been suggested as a possible mass transfer mechanism for ULXs (El Mellah et al. 2019a; Heida et al. 2019a,b). In this scenario, WRLOF can remain stable for large mass ratios while still leading, for relatively sufficient slow winds, to the formation of a wind-captured disk around the accretor, even when the donor does not fill its Roche lobe (RL, El Mellah et al. 2019b). El Mellah et al. (2019a) find that the mass-transfer rate can be boosted much higher than normal Bondi-Hoyle-Lyttleton (BHL) wind accretion (see their Fig. 3), necessary to reach the ULX luminosity level. We note several observations also support the idea of the WRLOF regime (Orosz et al. 2011; Liu et al. 2013). However, population synthesis on NS ULXs considering WRLOF is still lacking.

In the present work, we applied an up-to-date EPS code to investigate the population of NS ULXs in the case of the WRLOF scenario. In the EPS code, we implemented the mass transfer efficiencies μ computed by El Mellah et al. (2019a). We examined several parameters, such as metallicity and the exponent β of the velocity law, which may affect the stellar wind and hence the formation and evolution of WRLOF NS ULXs significantly. The objective of this Letter is to see if the two NS ULXs (i.e., P13 and NGC 300 ULX-1) can be explained in the WRLOF scenario within the range of a reasonable value of key parameters. We also explored the detailed components of wind-fed NS ULX populations, which may help understand the nature of the sources and may be testified by future observations.

This Letter is organized as follows. In Sect. 2, we describe the EPS method and the input physics for wind-fed NS ULXs in our model. The calculated results are presented in Sect. 3. We discuss and summarize our results in Sect. 4.

2. Models

We used the EPS code initially developed by Hurley et al. (2000, 2002) and updated by Zuo et al. (2014) to simulate the population of wind-fed NS ULXs. Several major updates have been made to this code, including the common envelope (CE) evolution (Xu & Li 2010; Loveridge et al. 2011), compact object (CO) mass prescription (i.e., the rapid supernova mechanism, Fryer et al. 2012; Belczynski et al. 2016), and natal kicks of CO formation (i.e., fallback prescription, Fryer et al. 2012). For NS formation, we adopted a Maxwellian kick distribution with a dispersion velocity of $\sigma_{\rm kick} = 265\,{\rm km\,s^{-1}}$ (Hobbs et al. 2005) for NSs that formed from core-collapse supernova explosion (SNe). We also considered the formation of low mass NSs through electron-capture supernova (i.e., ECS, Podsiadlowski et al. 2004), which typically has small kicks (Dessart et al. 2006, we assumed $\sigma_{\rm kick} = 50\,{\rm km\,s^{-1}}$). The maximum NS mass was assumed to be $3\,M_\odot$, above which BH was assumed to form. For CE evolution, we adopted the energy budget approach (Webbink 1984, 2008) and chose $\alpha_{\rm CE} = 0.9$ throughout (Zuo & Li 2014).

We assumed that all stars were formed in binaries (i.e., the binary fraction $f_{\rm b} = 1$) and evolved 8×10^6 primordial binaries in each model. The initial mass function (IMF) of Kroupa et al. (1993) was taken for the primary star, with mass $M_1 \in [7, 60]$ in solar mass. For the mass of the secondary, a flat distribution of the mass ratio $q \equiv M_2/M_1$ between 0 and 1 was adopted. We assumed that $\ln(a)$ was evenly distributed between $a = 3$ and $10^4\,R_\odot$. The tidal effect was taken into account to remove any eccentricity induced in a post-SN binary prior to the onset of mass transfer. The star formation rate (SFR) was fixed to be constantly $3\,M_\odot\,{\rm yr^{-1}}$ over the 13 Gyr period (Milky Way-like).

The stellar wind of massive stars is vital in our simulations. For the wind mass-loss, Vink et al. (2001) winds were applied for hot, massive stars, that is, metal-dependent fitting formulae given by Belczynski et al. (2010, that is to say Eqs. (6) and (7)). For Wolf-Rayet wind, we chose a combination of the Hamann & Koesterke (1998) wind and Vink & de Koter (2005) metal-dependent wind (i.e., Eq. (9), Belczynski et al. 2010). We adopted Eq. (8) in Belczynski et al. (2010) for luminous blue variable stars ($L > 6 \times 10^5$ and $10^{-5}RL^{1/2} > 1.0$, Humphreys & Davidson 1994), which is independent of metallicity. The other wind parameters are the same as in Hurley et al. (2000) if not mentioned otherwise. Due to the dependance of metallicity which may influence stellar winds significantly, we considered three choices of metallicity, that is, $Z = Z_\odot$(=0.02), $Z = 0.2\,Z_\odot$ and $Z = 0.02\,Z_\odot$ in our models, to see its effects. It is difficult to determine the wind velocity accurately. We set it proportional to the escape velocity from the surface of the mass-losing star, as a ratio $\beta_{\rm wind}$ (Hurley et al. 2002; Belczynski et al. 2008). The value of $\beta_{\rm wind}$ depends on the spectral type of the mass-losing star (Lamers et al. 1995). We adopted $\beta_{\rm wind} = 7$ for the most massive MS stars (>120 $M_\odot$), $\beta_{\rm wind} = 0.5$ for low-mass MS stars (<1.4 $M_\odot$), and interpolated in between. We adopted $\beta_{\rm wind} = 0.125$ (i.e., slow winds) for extended ($R_{\rm don} > 900\,R_\odot$) H-rich giants. For He-rich stars, we adopted $\beta_{\rm wind} = 7$ for $M_{\rm don} > 120\,M_\odot$ and $\beta_{\rm wind} = 1.3$ for $M_{\rm don} < 10\,M_\odot$, and interpolated in between. We note the terminal wind velocity of low mass He-rich stars is still very uncertain. The value we adopted here is different from that suggested by Belczynski et al. (2008), which is too low (J. S. Vink, priv. comm.).

For wind accretion, we adopted the commonly used Bondi-Hoyle-Lyttleton (BHL) mass-accretion-rate formula (Bondi & Hoyle 1944, see Eq. (6) in Hurley et al. 2002) for fast wind cases. When the orbital and wind velocities are comparable, the WRLOF mode was taken into account. In practice, if the mass transfer rate in the WRLOF mode is higher than the BHL rate, we adopted the WRLOF rate, otherwise the BHL rate was kept the same as in Hurley et al. (2002). For the WRLOF mode, we used the fitting formula based on data obtained from numerical simulations by El Mellah et al. (2019a, Fig. 2 and the data tables they provided) to conduct the calculation. In their simulation, the fraction of stellar wind captured, μ, only depends on the mass ratio $q = M_{\rm don}/M_{\rm CO}$, the stellar filling factor $f = R_{\rm don}/R_{\rm RL}$ (Eggleton 1983), the exponent β of the velocity law, and the ratio of the terminal wind speed to the orbital speed $\eta = v_\infty/v_{\rm orb}$, with $v_{\rm orb} = 2\pi a/P_{\rm orb}$ and $P_{\rm orb}$ being the orbital period. Since only two mass ratios for q ($q = 15$ for the NS and $q = 2$ for the BH) are provided for μ in their simulations, a linear interpolation (in logarithmic space) between the two extremal points was conducted for other cases than $q = 2$ and 15, which is expected to give a reasonable value of μ (suggested by Ileyk El Mellah). Due to the large uncertainties of the parameter β, which represents how fast the wind reaches its terminal speed (i.e., the efficiency of the acceleration), we adopted $\beta = 1$ (models labeled "B1"), $\beta = 2$ (models labeled "B2"), and $\beta = 3$ (models labeled "B3") to test its effects. We also designed models with only the BHL mode applied (models labeled "BHL") for comparison with the above WRLOF models (i.e., models B1, B2, and B3). Then combined with the three choices of metallicity, twelve models were constructed in total. Then the final absolute X-ray luminosity released by accretion onto a CO fed by a stellar companion could be calculated with the traditional formula $L_{\rm X} = 0.1\dot{M}c^2$, without considering the Eddington limit.

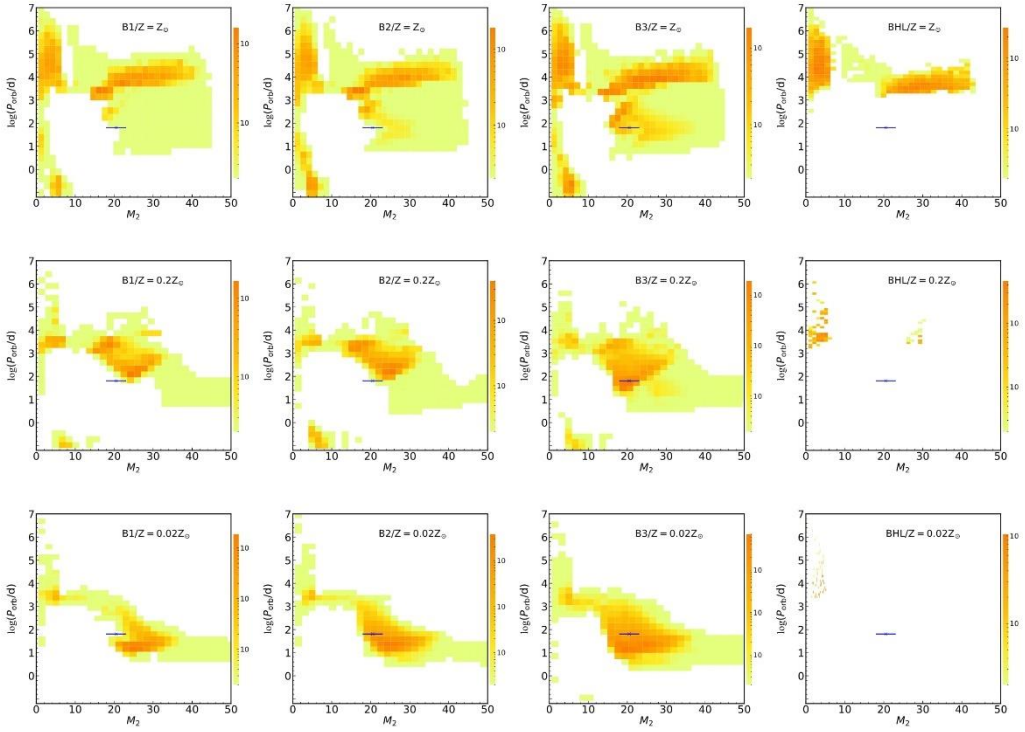

Fig. 1. Current orbital period $P_{\rm orb}-M_2$ distributions for models B1, B2, B3, and BHL at $Z = Z_\odot$ (*upper panel*), $0.2\,Z_\odot$ (*middle panel*), and $0.02\,Z_\odot$ (*lower panel*), respectively. The color represents the number of wind-fed NS ULXs (i.e., $L_{\rm X} > 10^{39}$ erg s^{-1}) in each matrix element. The cross with errorbars is the location of P13. The labels B1, B2, B3, and BHL in the panels represent WRLOF models with $\beta = 1$ (B1), $\beta = 2$ (B2), $\beta = 3$ (B3), and BHL models, respectively. For example, the model B1/$Z = Z_\odot$ represents WRLOF model with $\beta = 1$ (B1) and $Z = Z_\odot$.

Table 1. Expected number of wind-fed NS ULXs (i.e., $L_{\rm X} > 10^{39}$ erg s^{-1}) for a Milky-Way-like galaxy with SFR $= 3\,M_\odot$ yr^{-1} for models B1, B2, B3, and BHL at $Z = Z_\odot$, $0.2\,Z_\odot$, and $0.02\,Z_\odot$, respectively.

	B1	B2	B3	BHL
$Z_\odot$	3.1×10^{-1}	3.7×10^{-1}	6.8×10^{-1}	9.0×10^{-2}
$0.2\,Z_\odot$	3.2×10^{-1}	6.7×10^{-1}	1.5	7.0×10^{-3}
$0.02\,Z_\odot$	1.1	2.9	6.3	2.3×10^{-3}

3. Results

Our models show conclusively that with the WRLOF scenario taken into account, the population of wind-fed NS ULXs is distinct in number and binary parameters from that in the traditional BHL mode. Additionally, it is strongly metallicity dependent.

In Fig. 1, we show the distribution of current orbital period $P_{\rm orb}$ and donor mass M_2 in models B1, B2, B3, and BHL, respectively. The upper, middle, and lower panels are for metallicities with $Z = Z_\odot$ (i.e., Solar), $Z = 0.2\,Z_\odot$, and $Z = 0.02\,Z_\odot$, respectively. The color represents the number of wind-fed NS ULXs (i.e., $L_{\rm X} > 10^{39}$ erg s^{-1}) in each matrix element. Overplotted is the PULX P13 (Fürst et al. 2016; Israel et al. 2017a), which has a 20 $M_\odot$ B9Ia donor star in a ~64 day orbit (Motch et al. 2014). It is clear that the source P13 cannot be reproduced at all in any of the BHL cases, and the number of wind-fed NS ULXs in this case is low, especially in lower metallicities. However, when WRLOF is applied, many more NS ULXs are produced when comparing models B1, B2, and B3 with BHL models (see Table 1). The number of NS ULXs is enhanced greatly, about an order of magnitude in the solar case, and even more than two in lower metallicities. It is reasonable, as in the traditional BHL wind mode, wind accretion is much less efficient than RLOF, which has been neglected in previous studies (Linden et al. 2010; Shao & Li 2015; Wiktorowicz et al. 2017). However in the WRLOF mode, the mass-accretion rates are significantly enhanced, sometimes by more than an order of magnitude (El Mellah et al. 2019a, see their Fig. 3), which helps to reach a typical ULX luminosity level. When compared with current observational statistics (i.e., ~2 ULXs per $M_\odot$ yr^{-1} of SFR, Grimm et al. 2003; Swartz et al. 2011), our results are sound, that is, ~0.1 ULXs (at $Z = Z_\odot$) to ~1 ULXs ($Z = 0.02\,Z_\odot$) per $M_\odot$ yr^{-1} of SFR. We suggest that the WRLOF scenario should be taken into account for the study of ULX and its populations in the future.

However the component of WRLOF NS ULXs between models (i.e., B1, B2, and B3, we do not discuss BHL models

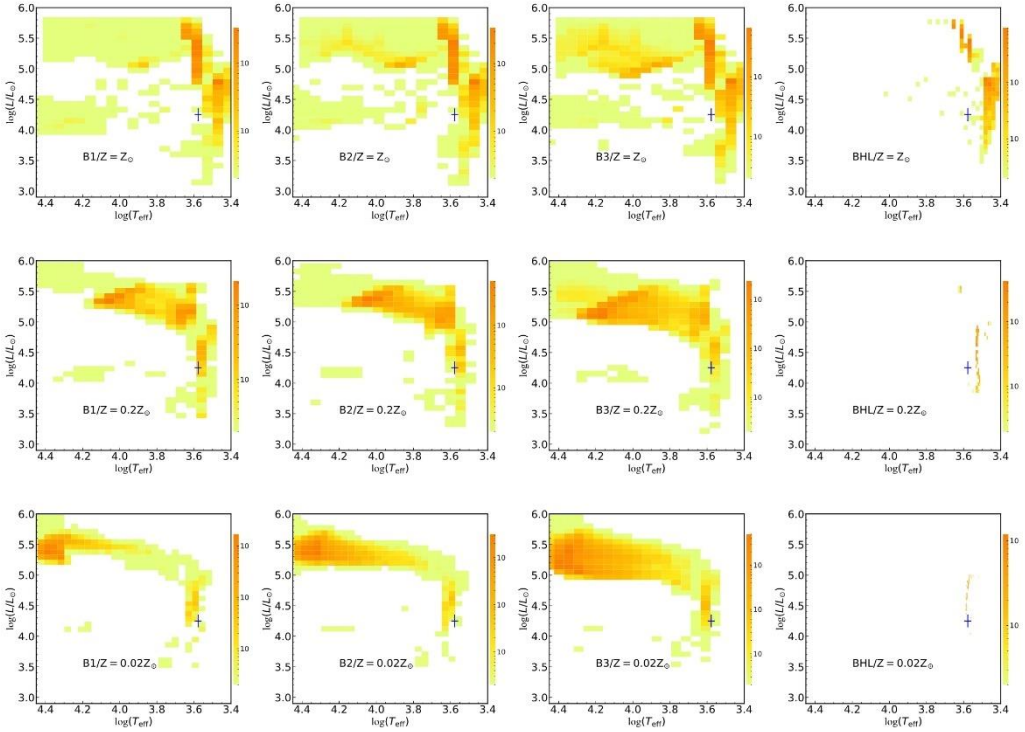

Fig. 2. Expected distributions of donor stars in H-R diagram for models B1, B2, B3, and BHL at $Z = Z_{\odot}$ (*upper panel*), $0.2\,Z_{\odot}$ (*middle panel*), and $0.02\,Z_{\odot}$ (*lower panel*), respectively. The color represents the number of wind-fed NS ULXs (i.e., $L_{\rm X} > 10^{39}\,{\rm erg\,s^{-1}}$) in each matrix element. The cross is the location of the red supergiant donor star in PULX NGC 300 ULX-1. The labels B1, B2, B3, and BHL in the panels represent WRLOF models with $\beta = 1$ (B1), $\beta = 2$ (B2), $\beta = 3$ (B3), and BHL models, respectively. For example, the model B1/$Z = Z_{\odot}$ represents the WRLOF model with $\beta = 1$ (B1) and $Z = Z_{\odot}$.

hereafter due to their rarity) is distinct. The different species reveal that they may come from different evolutionary pathways. We note the most common subpopulation is sources with massive ($\sim$15–40 $M_{\odot}$) (super)giant donors in WRLOF models (i.e., B1, B2, and B3). But the distribution of current orbital period $P_{\rm orb}$ is different and much shorter in lower metallicities ($\lesssim 10^3$ days in model B3; $\lesssim 10^4$ days in model B2) when compared with that in the solar cases ($\lesssim 10^5$ days in model B1). The phenomena we obtained here are very similar to that found by Linden et al. (2010) for supergiant high-mass X-ray binaries (SG-HMXBs, see the lower panel in their Fig. 5). The reason is that the donor with a poor metallicity is more compact than the rich ones (Linden et al. 2010; Klencki et al. 2020), particularly the maximum radius during the (sub)giant phase drops precipitously with decreasing metallicity (see their Fig. 7, Linden et al. 2010). So during the expansion of the donor before filling its RL, the orbit can be more compact at lower metallicities, while much wider at near solar metallicities. We note the donor of this population is mostly rejuvenated, that is, getting mass during the first RLOF from the more massive primary, which produces the NS after the SNe (age within $\sim$10 Myr). After that, the WRLOF phase may take place soon thereafter, lasting $\sim$0.1–1 Myr before the donor fills its RL, after which a common envelope (CE) occurs due to a large donor-to-compact object mass ratio, resulting in a binary merger. Another subpopulation is sources with lower donor masses (i.e., $M_2 < 10\,M_{\odot}$). Especially at solar metallicity (upper panel, models B1/$Z = Z_{\odot}$, B2/$Z = Z_{\odot}$, and B3/$Z = Z_{\odot}$), it clearly contains two species: one being sources with longer orbital periods (i.e., $P_{\rm orb} > 100$ days), which mainly come from binaries with a less massive progenitor ($<10\,M_{\odot}$), and large initial separations ($\sim 10^3$–$10^4\,R_{\odot}$). We note that when the star formation history is shortened to within tens of million years, corresponding to intense star burst cases, this population would drop. The other species is sources with short orbital periods (i.e., $P_{\rm orb} \sim 0.1$–100 days). We note that they are mainly stripped He-rich stars, which are produced from a CE.

In addition, we find that there is a trend that the larger the value of β, the more WRLOF NS ULXs are produced in each metallicity case. The reason is mainly related to the dependence of μ (i.e., the fraction of stellar wind captured by the accretor) on the exponent β of the velocity law, as illustrated in Fig. 2 by El Mellah et al. (2019a). It is clear in the figure that the higher β is, the larger μ is in the same condition, as the higher β, the later v_{∞} is matched, hence the larger μ as seen in their Fig. 2 and stated by El Mellah et al. (2019a). Furthermore, it is notable that P13 can be produced in all metallicity cases as well, especially in

cases with larger values of β and lower metallicities. Additionally, there is a weak trend that more WRLOF NS ULXs seem to be produced in lower metallicities, when compared with the solar cases, which is similar to the finding recently obtained by Marchant et al. (2017). It is because of the increase in μ with decreasing η, which is the most significant effect shown in their Fig. 2. We note sources in lower metallicities are more compact, that is, a smaller $P_{\rm orb}$, then a larger $v_{\rm orb} = 2\pi a/P_{\rm orb}$, hence a smaller $\eta = v_\infty/v_{\rm orb}$, which gives a larger μ, resulting in more NS ULXs instead, although the wind mass loss is relatively lower in the low-metallicity regime.

The donor of ULXs is the key to understanding the nature of ULXs and the population. In Fig. 2, we present the expected distributions of the luminosity $\log(L_{\rm bol}/L_\odot)$ and effective temperature $\log(T_{\rm eff}/{\rm K})$ of donor stars (i.e., H-R diagram) for models B1, B2, B3, and BHL, at $Z = Z_\odot$ (i.e., Solar, upper panel), $Z = 0.2\,Z_\odot$ (middle panel), and $Z = 0.02\,Z_\odot$ (lower panel), respectively. The color represents the number of wind-fed NS ULXs (i.e., $L_{\rm X} > 10^{39}\,{\rm erg\,s^{-1}}$) in each matrix element. The cross is the location of PULX NGC 300 ULX-1 (Carpano et al. 2018; Heida et al. 2019b) with a donor counterpart recently discovered as a RSG star ($T_{\rm eff} = 3650-3900$ K and $\log(L_{\rm bol}/L_\odot) = 4.25 \pm 0.10$, Heida et al. 2019a). It is clear that in each metallicity case, the source can be reproduced roughly in all WRLOF models. However, the percentage of RSG in all (super)giant donors changes largely as metallicity changes. It dominates in near solar metallicities (upper panel), but declines significantly as metallicity decreases. Also there is less of it in very low metallicity (i.e., $Z = 0.02\,Z_\odot$, lower panel). We note that RSG NS ULXs usually have lower donor masses (i.e., $M_2 < 10\,M_\odot$) with longer orbital periods (i.e., $P_{\rm orb} > 100$ days), while other (super)giant NS ULXs mainly have massive donors ($\sim$15$-$40 $M_\odot$), which are hotter and brighter, as expected.

4. Discussion and concluding remarks

This study shows that with the WRLOF accretion mode taken into account, it is possible to model the population of (super)giant NS ULXs, although the results are still subject to some uncertainties and simplified treatments. For example, the stellar wind of massive stars is vital in our simulations; however, it is still highly uncertain (Puls et al. 2008; Sander & Vink 2020), in particular due to the effects of clumping, other unsteady modes of mass loss, and the effects caused by a binary among massive stars (Smith 2014), about which our knowledge is still poor. In this study, we adopted a simplified parameter, $\beta_{\rm wind}$, to depict the velocity of stellar wind. Normally, a smaller $\beta_{\rm wind}$ means a smaller wind velocity v_∞, hence a smaller $\eta = v_\infty/v_{\rm orb}$, resulting in a higher mass transfer efficiency μ. We also varied the value of $\beta_{\rm wind}$ for very hot stars from 7 to 3, but we find no significant changes in our results. Additionally, for the super-Eddington accretion, geometrical beaming may take place (King et al. 2001; Poutanen et al. 2007; King 2008; King & Lasota 2020), but it is still very uncertain (Abarca et al. 2018; Mushtukov et al. 2021). We also tested this scenario and find that our conclusion is largely unchanged. Finally, we note that the absolute formation rate of (wind-fed) NS ULXs is highly uncertain. Several parameters, such as the star formation rate and history of the galaxy, the binary fraction, the IMF of the primary and secondary stars, and the natal kick of newborn NS (Zuo et al. 2014) may affect it significantly by up to one or two orders of magnitude. Unique galaxies such as ring galaxies (Wolter et al. 2018) are helpful to further address this issue (i.e., the relative and absolute formation rate of different kinds of ULXs through the X-ray luminosity function modeling, see Zuo et al. 2014, for example), which is in preparation, however, and beyond the scope of this Letter.

Nevertheless, this study still shows that the population of wind-fed NS ULXs in WRLOF mode is distinct in number and the binary parameters from that in the traditional BHL mode, and it is strongly metallicity dependent. The number of NS ULXs with (super)giant donors is enhanced greatly by about an order of magnitude in solar cases, and even more than two in lower metallicities (see Table 1) when considering the WRLOF accretion mode. Furthermore, they are heavily metallicity-dependent. The most common population in all WRLOF models is sources with massive ($\sim$15$-$40 $M_\odot$) (super)giant donors, which dominate in lower metallicities. However, that is not the case in the solar case, which is dominated by RSG with lower mass $M_2 < 10\,M_\odot$ instead. Moreover, the two NS ULXs (i.e., P13 and NGC 300 ULX-1) can be well reproduced in the WRLOF paradigm, which significantly enriches our understanding of the nature of ULXs and the population. We also present the current distributions of binary parameters (see Figs. 1 and 2), which may be further testified by high-resolution optical and X-ray observations of (NS)ULXs populations in the future.

Acknowledgements. We thank Ileyk El Mellah for providing the data tables that help to conduct the simulation. We are grateful to Ileyk El Mellah for useful discussions on the WRLOF scheme and Jorick S. Vink for the constructive suggestions on the wind velocity of He-rich star. This work is supported by the National Natural Science Foundation of China (grant Nos. 11573021, U1938104, 12003020) and the Fundamental Research Funds for the Central Universities.

References

Abarca, D., Kluźniak, W., & Sądowski, A. 2018, MNRAS, 479, 3936
Bachetti, M., Harrison, F. A., Walton, D. J., et al. 2014, Nature, 514, 202
Begelman, M. C. 2002, ApJ, 568, L97
Belczynski, K., Kalogera, V., Rasio, F. A., et al. 2008, ApJS, 174, 223
Belczynski, K., Bulik, T., Fryer, C. L., et al. 2010, ApJ, 714, 1217
Belczynski, K., Heger, A., Gladysz, W., et al. 2016, A&A, 594, A97
Bondi, H., & Hoyle, F. 1944, MNRAS, 104, 273
Brightman, M., Harrison, F. A., Fürst, F., et al. 2018, Nat. Astron., 2, 312
Carpano, S., Haberl, F., Maitra, C., & Vasilopoulos, G. 2018, MNRAS, 476, L45
Colbert, E. J. M., & Mushotzky, R. F. 1999, ApJ, 519, 89
Dall'Osso, S., Perna, R., Papitto, A., Bozzo, E., & Stella, L. 2016, MNRAS, 457, 3076
Dessart, L., Burrows, A., Ott, C. D., et al. 2006, ApJ, 644, 1063
Eggleton, P. P. 1983, ApJ, 268, 368
Ekşi, K. Y., Andaç, İ. C., Çıkıntoğlu, S., et al. 2015, MNRAS, 448, L40
El Mellah, I., Sundqvist, J. O., & Keppens, R. 2019a, A&A, 622, L3
El Mellah, I., Sander, A. A. C., Sundqvist, J. O., & Keppens, R. 2019b, A&A, 622, A189
Fabbiano, G. 1989, ARA&A, 27, 87
Fragos, T., Linden, T., Kalogera, V., & Sklias, P. 2015, ApJ, 802, L5
Fryer, C. L., Belczynski, K., Wiktorowicz, G., et al. 2012, ApJ, 749, 91
Fürst, F., Walton, D. J., Harrison, F. A., et al. 2016, ApJ, 831, L14
Fürst, F., Walton, D. J., Heida, M., et al. 2018, A&A, 616, A186
Gladstone, J. C., Roberts, T. P., & Done, C. 2009, MNRAS, 397, 1836
Grimm, H. J., Gilfanov, M., & Sunyaev, R. 2003, MNRAS, 339, 793
Hamann, W. R., & Koesterke, L. 1998, A&A, 335, 1003
Heida, M., Jonker, P. G., Torres, M. A. P., et al. 2014, MNRAS, 442, 1054
Heida, M., Torres, M. A. P., Jonker, P. G., et al. 2015, MNRAS, 453, 3511
Heida, M., Jonker, P. G., Torres, M. A., et al. 2016, MNRAS, 459, 771
Heida, M., Harrison, F. A., Brightman, M., et al. 2019a, ApJ, 871, 231
Heida, M., Lau, R. M., Davies, B., et al. 2019b, ApJ, 883, L34
Hobbs, G., Lorimer, D. R., Lyne, A. G., & Kramer, M. 2005, MNRAS, 360, 974
Humphreys, R. M., & Davidson, K. 1994, PASP, 106, 1025
Hurley, J. R., Pols, O. R., & Tout, C. A. 2000, MNRAS, 315, 543
Hurley, J. R., Tout, C. A., & Pols, O. R. 2002, MNRAS, 329, 897
Israel, G. L., Papitto, A., Esposito, P., et al. 2017a, MNRAS, 466, L48
Israel, G. L., Belfiore, A., Stella, L., et al. 2017b, Science, 355, 817
Kaaret, P., Ward, M. J., & Zezas, A. 2004, MNRAS, 351, L83
Kaaret, P., Feng, H., & Roberts, T. 2017, ARA&A, 55, 303
King, A. R. 2008, MNRAS, 385, L113

King, A., & Lasota, J.-P. 2020, MNRAS, 494, 3611
King, A. R., Davies, M. B., Ward, M. J., Fabbiano, G., & Elvis, M. 2001, ApJ, 552, L109
Klencki, J., Nelemans, G., Istrate, A. G., & Pols, O. 2020, A&A, 638, A55
Kroupa, P., Tout, C. A., & Gilmore, G. 1993, MNRAS, 262, 545
Lamers, H. J. G. L. M., Snow, T. P., & Lindholm, D. M. 1995, ApJ, 455, 269
Lau, R. M., Heida, M., Walton, D. J., et al. 2019, ApJ, 878, 71
Linden, T., Kalogera, V., Sepinsky, J. F., et al. 2010, ApJ, 725, 1984
Liu, J., Bregman, J. N., & Seitzer, P. 2004, ApJ, 602, 249
Liu, J.-F., Bregman, J. N., Bai, Y., Justham, S., & Crowther, P. 2013, Nature, 503, 500
Loveridge, A. J., van der Sluys, M. V., & Kalogera, V. 2011, ApJ, 743, 49
Marchant, P., Langer, N., Podsiadlowski, P., et al. 2017, A&A, 604, A55
Mohamed, S., & Podsiadlowski, P. 2007, in 15th European Workshop on White Dwarfs, eds. R. Napiwotzki, & M. R. Burleigh, ASP Conf. Ser., 372, 397
Motch, C., Pakull, M. W., Soria, R., Grisé, F., & Pietrzyński, G. 2014, Nature, 514, 198
Mushtukov, A. A., Portegies Zwart, S., Tsygankov, S. S., Nagirner, D. I., & Poutanen, J. 2021, MNRAS, 501, 2424
Orosz, J. A., McClintock, J. E., Aufdenberg, J. P., et al. 2011, ApJ, 742, 84
Podsiadlowski, P., & Mohamed, S. 2007, Balt. Astron., 16, 26
Podsiadlowski, P., Langer, N., Poelarends, A. J. T., et al. 2004, ApJ, 612, 1044
Poutanen, J., Lipunova, G., Fabrika, S., Butkevich, A. G., & Abolmasov, P. 2007, MNRAS, 377, 1187
Puls, J., Vink, J. S., & Najarro, F. 2008, A&ARv, 16, 209
Rodríguez Castillo, G. A., Israel, G. L., Belfiore, A., et al. 2020, ApJ, 895, 60
Sander, A. A. C., & Vink, J. S. 2020, MNRAS, 499, 873
Sathyaprakash, R., Roberts, T. P., Walton, D. J., et al. 2019, MNRAS, 488, L35
Shao, Y., & Li, X. D. 2015, ApJ, 802, 131
Smith, N. 2014, ARA&A, 52, 487
Sutton, A. D., Roberts, T. P., & Middleton, M. J. 2013, MNRAS, 435, 1758
Swartz, D. A., Soria, R., Tennant, A. F., & Yukita, M. 2011, ApJ, 741, 49
Tong, H. 2015, Res. Astron. Astrophys., 15, 517
Villar, V. A., Berger, E., Chornock, R., et al. 2016, ApJ, 830, 11
Vink, J. S., & de Koter, A. 2005, A&A, 442, 587
Vink, J. S., de Koter, A., & Lamers, H. J. G. L. M. 2001, A&A, 369, 574
Walton, D. J., Fürst, F., Heida, M., et al. 2018, ApJ, 856, 128
Webbink, R. F. 1984, ApJ, 277, 355
Webbink, R. F. 2008, in Common Envelope Evolution Redux, eds. E. F. Milone, D. A. Leahy, & D. W. Hobill, 352, 233
Wiktorowicz, G., Sobolewska, M., Sądowski, A., & Belczynski, K. 2015, ApJ, 810, 20
Wiktorowicz, G., Sobolewska, M., Lasota, J.-P., & Belczynski, K. 2017, ApJ, 846, 17
Wiktorowicz, G., Lasota, J.-P., Middleton, M., & Belczynski, K. 2019, ApJ, 875, 53
Wolter, A., Fruscione, A., & Mapelli, M. 2018, ApJ, 863, 43
Xu, X. J., & Li, X. D. 2010, ApJ, 716, 114
Zuo, Z.-Y., & Li, X.-D. 2014, MNRAS, 442, 1980
Zuo, Z.-Y., Li, X.-D., & Gu, Q.-S. 2014, MNRAS, 437, 1187

附 录D 环形星系ULX论文

Mon. Not. R. Astron. Soc. **000**, 1–7 (2014) Printed 27 June 2021 (MN LATEX style file v2.2)

Ultra-luminous X-Ray sources with wind Roche lobe overflow in Ring galaxies

Hao-Tian Song[1] and Zhao-Yu Zuo[1,2⋆]
[1]*Department of Physics, School of Science, Xi'an Jiaotong University, Xi'an 710049, China*
[2]*Key laboratory of Modern Astronomy and Astrophysics (Nanjing University), Ministry of Education, Nanjing 210093, China*

27 June 2021

ABSTRACT
Ultra-luminous X-ray sources (ULX) are binaries containing a nondegenerate companion and a black hole (BH) or neutron star (NS), drawing great attention due to their super-Eddington luminosity. We have presented the comprehensive evolution model for ULXs in Ring galaxies including wind Roche-Lobe overflow mechanism. The wind-fed ULXs contributes more to population than traditional Bondi-Hoyle-Lyttleton (BHL) mode. Seven galaxies was adopted as example of star burst galaxies and X-ray luminosity function (XLF) was compared between observation and simulation. We predicted that donor mass is $2.7M_{\odot}$ and orbit period is few days in typical ULXs. Most of donor star are H donor stars, indicating active evolution stage.

Key words: methods: statistical — galaxies: star-burst — stars: evolution — X-ray: binaries — stars: distribution

1 INTRODUCTION

As off-center, point-like sources with isotropic equivalent X-ray luminosity $L_X > 10^{39} erg \cdot s^{-1}$, ultra-luminous X-ray sources (ULXs) have been focused on by plenty of observational and theoretical work (see Kaaret et al. 2017, for reviews). Generally ULXs are regarded as tail of high mass X-ray binaries (HMXB). The mechanism of ULXs is accretion of X-ray binaries. The compact stars are thought to be Black Holes (BH) before discovery of pulsing ultra-luminous X-ray source (PULXs) in M82 X-2 (Bachetti et al. 2014) with $L \simeq 1.8 \times 10^{40} \mathrm{ergs}^{-1}$. Neutron Stars (NS) mostly accompany by pulsar-like dipole field strengths $10^{11} \lesssim B \lesssim 10^{13}$G which allows several descriptions of the observed properties (King et al. 2017; Middleton et al. 2019).

As the luminosity of $10^{39} erg \cdot s^{-1}$ is the Eddington luminosity of a $10M_{\odot}$ BH, the majority of ULXs is super-Eddington isotropic accretion. However, assumption of geometrical beaming (King et al. 2001) can avoid breaching the Eddington luminosity with support of accretion disk simulation (Jiang et al. 2014; Ohsuga & Mineshige 2011). King (2009) gave an example of collimated radiation with $L > 3L_{Eddington}$. Furthermore, beaming factor in NS are correspondingly lower than BH with the same Mass transfer (MT) rate, which indicates that PULXs dominate the region of higher luminosity (King & Lasota 2016).

Previous theoretical simulation mostly indicates the stable RL overflow is the primary method for ULXs (Shao & Li 2015; Wiktorowicz et al. 2019a; Shao et al. 2019), which all implied the BHL mass transfer mode for wind overflow. For instances, Shao & Li (2015) utilized evolutionary population synthesis to reconstruct the evolution of NS ULXs. The simulation generally displays the mass-orbital plane and the predicted amount of NS ULXs in M82 and MW-like Galaxies. More specific systematic study in MW galaxies for NS ULXs indicates that donor star tends to be helium star (Shao et al. 2019). Furthermore, specific simulation via StarTrack EPS code was conducted by Wiktorowicz et al. (2019a), who took geometrical beaming into account. Assuming individual metallicity, They drew the conclusion that BH emits radiation isotropically while NS predominantly, and BH ULXs outnumber NS ULXs which is inconsistent with observation. Recently, wind-powered simulation by Baker et al. (2013) demonstrates that the majority of specific ULXs (red super-giant companion) transfer mass via wind-fed mode. However, the formalism of WRL developed by (Abate et al. 2013) was just adoptable for narrow region of parameters, whereas donors stars need to be carbon-enhanced metal-poor stars. As consequence, the observation is hard to be related to simulation results in such a strict condition. Another research about wind Roche-lobe overflow cases Zuo, Zhao-Yu et al. (2021) emphasized the enhancement of wind accretion mechanism and displayed the predicted binary parameters of NS ULXs.

Ring Galaxies are ideal laboratories for binaries evolution research. Although they contribute to a small distri-

⋆ E-mail:zuozyu@xjtu.edu.cn

bution (Wolter et al. 2018a, approximately $0.02\% - 0.2\%$ of all spiral galaxies), particular and energetic environment without contamination from spurious sources is suitable for studying binary evolution. The reason of burst star forming in Ring Galaxies is encounter with nearby galaxies, which implies that the age of stars is similar. Besides, most ULXs formulation environment is normal sharing similar metallicity (Wolter et al. 2018). Additionally, with high star forming rates (SFR) and shorter evolution duration, Ring Galaxies share more similarity with assuming environment, which avoids the various initial conditions of EPS. According to (Wolter et al. 2015), remarkable number of ULXs was detected in Star-burst galaxies strongly supports our simulation.

In this work, we utilize the advanced WRL mechanism for the BPS of ULXs, and predicted ULXs' number and population in Ring galaxies. The evolution parameters are comply the characteristics of Ring galaxies and observation X-ray luminosity function is used to be compared with simulation.

2 METHODS

We utilized the Evolutionary population synthesis (EPS) code initially developed by Hurley et al. (2002) with further updates, which are briefly described as follows. And MESA program was performed in the population synthesis of NS for more specific evolution.

The Initial Mass Function (IMF) developed by Kroupa et al. (1993) was applied. Although the shapes of IMF differ significantly, it is less subject to the uncertainty due to the similarity of the IMFs for larger masses. The mass of star on zero-age sequence (ZAMS) satisfies the following distribution with initial mass ranging from 2 $M_\odot$ to 150 $M_\odot$.

$$\xi(m) \propto m^{-\alpha} \tag{1}$$

where

$$\alpha(m) = \begin{cases} +0.3 \pm 0.7 & 0.01 \leqslant m < 0.08 \\ +1.3 \pm 0.5 & 0.08 \leqslant m < 0.50 \\ +2.3 \pm 0.3 & 0.50 \leqslant m < 1.00 \\ +2.3 \pm 0.7 & 1.00 \leqslant m \end{cases} \tag{2}$$

The distribution of mass ratios q ($q = M_1/M_2$) was uniform between 0.08 and 1 by steps of 0.10 (Wiktorowicz et al. 2019b). The orbital separation was ranged from 3.0 to $10^4 R_\odot$ which facilitates the comparison with other models (Yungelson et al. 1997). Here we assumed that $ln(a)$ is uniformly distributed. According to the previous analysis Wolter et al. (2018), produced stars are younger than 300Myr and majority of them is consistent with age of HMXBs. Therefore, the maximum evolution time was set to 200Myr in isolation. As for supernova kicks, we draw them from a Maxwellian distribution with $\sigma = 265km \cdot s^{-1}$ (Hobbs et al. 2005). And subsolar metallicity $Z = 0.5Z_\odot$ was adopted in our simulations which is the metallicity prediction of environment (Wolter et al. 2018). Furthermore, metallicity is a key factor affecting the evolution (Zuo, Zhao-Yu et al. 2021).

For sources undergoing Roche Lobe Overflow (RLOF) mass-transfer, the traditional formula was used for sub-Eddington accretion rates, where Eddington luminosity is approximately $L_E = 1.6 \times 10^{38} m_1$ for hydrogen-rich material. Supplied with super-Eddington mass transfer rates, the accretor expel matter in significantly different approach. Outside the spherization R_{sph} (Blundell et al. 2007), accretion luminosity is released as usual (Shakura & Sunyaev 1973; Poutanen et al. 2007). But within R_{sph}, radiation become inefficient and the outflow maintain energy release in L_E under the pressure of radiation. Bolometric luminosity L_X is

$$L_X = \begin{cases} L_{\rm Edd}\,(1 + \ln \dot{m}_{\rm tr}) & \dot{m}_{\rm tr} > 1 \\ L_{\rm Edd} \dot{m}_{\rm tr} & \dot{m}_{\rm tr} \leqslant 1 \end{cases} \tag{3}$$

Where $\dot{m}_{\rm tr} = \dot{M}_{\rm tr}/\dot{M}_{\rm Edd}$ and $\dot{M}_{\rm tr}$ is in units of $M_\odot/yr$. For the region within R_{sph}, a biconical geometry is formed with collimation of radiation (King 2008). Therefore, the finite cones can be detected by observer. The apparent (isotropic) X-ray luminosity is

$$L_{app} = L_X/b \tag{4}$$

Where b is beaming factor defined as the fraction of funnels area, $b \overset{\rm def}{=} \Omega/4\pi$, and Ω is the combined solid angle of both beams. When $\dot{m}$ is larger enough, the scales can vary from the typical cylinderical radius to R_{sph} markedly. And for soft-excess luminosity, the observed relation $L_{\rm soft} \propto T^{-4}$ sustain the estimated value of b (King 2009).

$$b = \begin{cases} 1 & \dot{m}_{\rm tr} \leqslant 8.5 \\ \frac{73}{\dot{m}_{\rm tr}^2} & 8.5 < \dot{m}_{\rm tr} \end{cases} \tag{5}$$

whereas for $\dot{m} < 8.5$, it is assumed unbeamed. And this formula have been verified in plenty of hyperluminous X-ray sources (King & Lasota 2014, 2016; King et al. 2017). In addition, there was an implication (Wiktorowicz et al. 2017) that extremely beamed sources are scarce and transient that lead to difficulty in detection. That means there is no lower valve for the beaming factor. For CE evolution during this process, the energy budget approach have been implied (Webbink 1984, 2008) and we set $\alpha_{CE} = 0.9$ suggested by Zuo & Li (2014).

Furthermore, the wind Roche lobe overflow (WRL) could be taken into account. The traditional Bondi-Hoyle-Lyttleton (BHL) MT formula for WRL (Bondi & Hoyle 1944; Edgar 2004) is

$$\dot{M}_{\rm BHL} = \pi R_{\rm BHL}^2 v_{\rm rel} \rho \tag{6}$$

where $\dot{M}_{\rm BHL}$ is the mass accretion rate, $v_{\rm rel} = \sqrt{v_\beta^2 + (v_{\rm orb}[q/(1+q)])^2}$ is relative speed between the wind and compact object. $v_{\rm orb}$ is orbital speed given by $v_{orb} = 2\pi a/P_{orb}$ with P_{orb} being the orbit period. $R_{BHL} = 2GM_\bullet/v_{\rm rel}^2$ is the modified accretion radius and ρ is the density of the wind at orbital separation. After assumption of isotropic dilution of the wind, the fraction of wind captured $\mu_{\rm BHL} = \dot{M}_{\rm BHL}/\dot{M}_\star$ can be:

$$\mu_{\rm BHL} = \frac{(1+q)/q^3}{\eta(1-f\mathcal{E})^\beta \left[1 + (\eta(1+q)(1-f\mathcal{E})^\beta/q)\right]^{3/2}} \tag{7}$$

where $\mathcal{E}$ is the ratio of stellar Roche lobe radius by the orbital separation and only related to q (Eggleton 1983), and η is the speed ratio. We adopt this model for fast wind accretion. However, another research (El Mellah et al. 2019) proposed that ULXs could remain stable in WRL with a

Table 1. Properties of Ring galaxies applied in this work.

Name	Distance (Mpc)	SFR ($M_\odot/yr$)	Z ($Z_\odot$)
Cartwheel	122	20	0.14
NGC 922	48	8.0	0.5-1.
Arp 147	133	4.1	0.19-0.40
AM 0644-741	91.6	2.6	0.45
Arp 143	57.1	2.3	0.44-0.71
Arp 148	145.2	2.5	
Arp 284	37	4.0	0.19-0.38

highly beamed wind. Based on realistic acceleration profiles, they estimated the MT by computing the bulk motion of the wind. By assuming non-isotropic dilution of stellar wind, the fraction of wind captured can be significantly higher especially for higher wind speed ratio. And several binary systems have been proved possible for WRL, such as M101 (Liu et al. 2013), and P13 (Fürst et al. 2018). We adopted his simulation and assume μ as a function of η, stellar filling factor, β and mass ratio q. The WRL efficiency systematically improved. And WRL can be a possible mechanism for ULXs. In this mechanism, the value of the wind velocity is not accurate during the simulation. As suggested by Belczynski et al. (2008), it was proportional to the escape velocity from the surface of the mass-lossing star

$$V_{\rm wind}^2 = 2\beta_{\rm wind}\frac{GM_{\rm don}}{R_{\rm don}} \tag{8}$$

where $M_{\rm don}$ and $R_{\rm don}$ are the mass and radius of donor star respectively. $\beta_{\rm wind}$ depends on the spectral type of the donor star. For main Sequence stars, we adopted a linear interpolation from $\beta_{\rm wind} = 0.5$ for lower massive stars ($< 1.4M_\odot$) to $\beta_{\rm wind} = 7$ most massive stars ($> 120M_\odot$) Lamers et al. (1995). The $\beta_{\rm wind}$ of extended H-rich stars ($R_{\rm don} > 900R_\odot$) was set to 0.125 due to slow winds. As for He-rich stars, $\beta_{\rm wind} = 7$ when $M_{donor} > 120M_\odot$ (the same as MS stars) and $\beta_{\rm wind} = 1.3$ when $M_{donor} < 10M_\odot$, and we interpolated in between.

As for the observation of ULXs, the statistics of ULXs in seven galaxies have been published (Wolter et al. 2018a). Relevant properties are listed in Tab. 1. All the metallicity of these galaxies are sub-solar and similar to each other. For numerical comparison with them, the evolved population of binaries should be in conjunction with a realistic birth rates and metallicity. Here the distribution of each binary system is

$$\delta r_j = \overline{S_b}\Phi\left(\ln M_{1j}\right)\varphi\left(\ln M_{2j}\right)\Psi\left(\ln a_j\right)\delta\ln M_1\delta\ln M_2\delta\ln a \tag{9}$$

where r is the rate of particular population, and $\overline{S_b}$ is the binary star forming rate (SFR) in units of *number/year* which can be obtained from following formula with SFR in units of $M_\odot/yr$ for binaries massive than 5 $M_\odot$ (Grimm et al. 2003):

$$\overline{S_b} = \left(\frac{M_{low}}{5}\right)^{1-\alpha}\frac{(\alpha-2)SFR}{5(\overline{3}+\overline{q})(\alpha-1)} \tag{10}$$

where M_{low} is the lower limit initial mass for EPS. For summation of seven galaxies $SFR \approx 42M_\odot/yr$, $\overline{S_b} = 1.5039yr^{-1}$ The total number N should be the summation of every binary system distribution. However, the number observed could differ in consideration of beaming effect. With assumption of linear relation between the area of the flux sphere and beaming factor, the chance probability is therefore $P \propto b$ (Middleton & King 2017). The observed number N_{OBS} is

$$N_{OBS} = \sum\delta N = b\sum\delta r\delta T \tag{11}$$

where δT is the duration of particular binary evolution stage. For mesa simulation, δr was obtained from EPS code where particular event is the birth of NS.

3 SIMULATION RESULTS

The simulation in this section was performed with constant SFR and metallicity. Maximal evolution time is 200Myr for early formed Ring galaxies. Because SFR in Star-burst galaxies are relatively high ($SFR > 4.5M_\odot yr^{-1}$), it is reasonable to assume that the number of ULXs is linear to constant SFR in this algorithm which accords with previous work (Mineo et al. 2013). With assumption of constant SFR for observed galaxies, we compare it with observation and previous analysis. Taking complex episodes of star forming into account, estimates should be modified via a more realistic method. We adopt EPS code developed by Hurley et al. (2002) for the evolution of BH binaries while NS binaries we implied the MESA for detailed simulation of several episodes.

Ring galaxies are comparatively rare (15 out of 345 galaxies), in which, however, the ULXs occupy the certain proportion. According to Wang et al. (2016), the observation analysis feature of star-burst galaxies (i.e., the shape of XLF and) is distinct with others galaxies which deserves our attention. Ring galaxies can imply general characteristics of ULXs due to its pure environment and burst star forming. Furthermore, young galaxies provide pure environment for star evolution and prediction of early-type galaxies share more similarity with population synthesis (see Figure 15 in Kovlakas et al. 2020). We have conducted our calculation to compare them with galaxy-focused observations (Wolter et al. 2018a). The result of X-ray luminosity function (XLF) is presented in Fig. 1.

The estimated numbers of ULXs are based on Eq. 9. The summation of the SFR for 7 galaxies is approximately $43.5M_\odot$ obtained from $L_{H\alpha}$ (Appleton & Marston 1997). Uncertainty of measuring SFR should be noticed which leads to the uncertainty of our simulation result. Therefore the observation of other limited galaxies may not be representive and comparable to our simulation. 50 sources above the ULXs valve ($10^{39}erg\cdot s^{-1}$ suggested by Kaaret et al. (2017)) are collected of which 23 sources are above $5\times10^{39}erg\cdot s^{-1}$. The simulation XLF generally fits the observation and display the characteristics of ULXs. Statistical research (Swartz et al. 2011) have been done including 107 identified ULXs in 127 nearby galaxies and differential function of XLF shows a power-law slope. The statistical simulation has been compared with observation Wolter et al. (see Fig. 5 in 2018b). The difference between star-burst galaxies and nearby galaxies is obvious in XLF, where the XLF in nearby galaxies show steeper decrease. Besides, XLF in HMXBs (Grimm et al. 2003) is also impossible to fit this in star-burst galaxies. Because the census of these galaxies is not suitable for our simulation for starburst galaxies due to their unique evo-

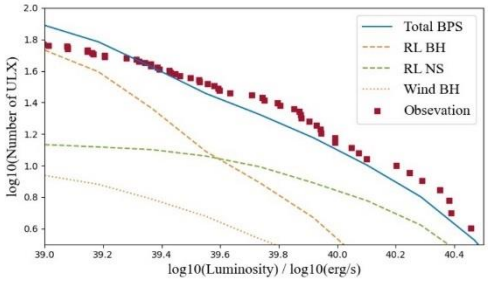

(a)

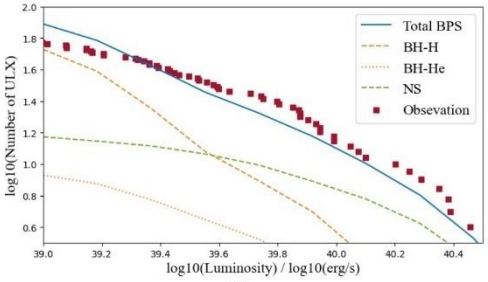

(b)

Figure 1. X-ray luminosity function (XLF) for seven Ring galaxies mentioned above. The solid blue line represents total ULXs number via EPS simulation, and red dots represent observation. (a) Dashed dotted lines represent the ULXs number in Roche Lobe accretion and wind accretion respectively. The compact star is BH and NS for pale blue and green lines respectively. (b) The simulation distribution of ULX donor and compact star. Dashed and dotted lines are ULX with Hydrogen rich and Helium rich donor star respectively, and orange lines are BH compact star while green line is NS.

lution stage and environment. However, these are requisite for EPS research.

According to the EPS simulation result, there is a break at approximately $3\times10^{40}erg\cdot s^{-1}$ which accords with the observation of other galaxies (Mineo et al. 2012; Swartz et al. 2011). The XLF break correspond to the Eddington luminosity of NS (Belczynski & Ziolkowski 2009). Although extreme objects reaching a peak luminosity of $10^{41}erg\cdot s^{-1}$ exist Gao et al. (e.g., 2003, M82), they are candidates for Intermediate Mass Black Holes (IMBHs) with masses in between $(10^2-10^5M_\odot)$ (Kuranov et al. 2007; Greene et al. 2020). With completely disparate formation scenarios, IMBHs exclude from consideration in this work. Although there is small probability of forming extremely luminous sources ($L_X > 3\times10^{40}erg\cdot s^{-1}$) in our simulation, they demand high beaming factor and correspondingly are impossible to be detected. Additionally, the observation in Ring galaxies of those cases is also limited, so we focus on middle part of XLF.

The accretion via WRL contributes quiet a few by implying this nonisotropic mechanism. Although accretion fraction μ is smaller than 20% in WRL and must be less

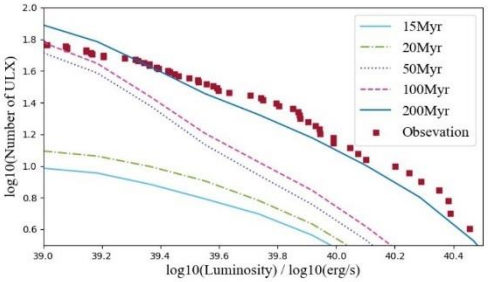

Figure 2. XLF for various evolution duration of ULXs for 200 Myr, 100 Myr, 50 Myr, 20 Myr, 15 Myr.

than 50% (Mohamed & Podsiadlowski 2011) which means most mass is lost during the accretion, ULXs via WRL exist and can reach luminosity at $5\times10^{40}erg\cdot s^{-1}$. In our simulation, high donor star mass and considerable mass transfer rate provide enough fuel for X-ray radiation. For WRL, Roche Lobe is brimming with donor star where situation is unstable in RL overflow. Consequently, mass ratio limit for donor star is more strict in RL overflow than WRL. In our simulation, high mass ratios of WRL (larger than 3) and heavy donor masses ($>10M_\odot$) are common in WRL cases, while it's unstable for RLOF. We can conclude that accretion could be stable in these evolution stage via WRL which accords to Baker et al. (2013) and ULXs with WRL occupy part of XLF in low luminosity region.

For RLOF, their population dominates in XLF and can be divided into two groups according to compact star (BH or NS, see Fig. 1). For less luminous sources, the compact stars of ULXs tend to be BH instead of NS. We note that duration of BH RLOF in high luminosity is significantly longer than NS, and, consequently, more likely to be observed. The mass and radius of NS is lower than BH, and duration of constant mass transfer is harder to maintain before next evolution stage. The typical orbit period for BH via RLOF is a few days and donor star mass tends to be less than 2.7 solar mass. Low initial donor star mass indicates high probability of birth and, correspondingly, larger proportion in population of ULXs. Meanwhile, NS dominates in the region with higher luminosity$L_{app} > 10^{40}erg\cdot s^{-1}$, which is analogous to the previous work (Shao & Li 2015). In our simulation, there is a proven positive correlation between beaming factor and luminosity as shown in Eq. 4. X-ray radiation in BH ULXs is commonly isotropical or mildly-beamed. However, beaming effects is obvious in NS ULXs, and saturated beaming ($b_{min} = 3.2\times10^{-3}$sec (Lasota et al. 2016)) can be reached in some cases, which is an immediate cause of high luminosity of NS ULXs.

In Fig. 1 (b), we displayed the distribution of Helium rich and Hydrogen rich donor stars. There is evidence showing that evolved donor stars should be the major of ULXs population. For analysis of ULXs' ages, we performed various evolution duration in our simulation, and displayed them in Fig. 2. We ploted the XLF with different color for respective evolution duration. The number of more luminous ULXs significantly drops at an age of 150Myr whose compact star corresponds to NS. When the population is around 30 Myr,

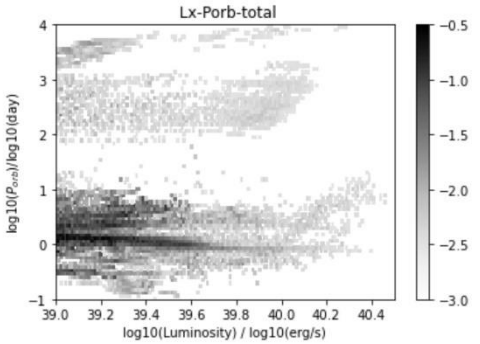

Figure 3. The numerical distribution in the $P_{orb} - L_X$ plane for ULXs. The depth of shade represents the quantity.

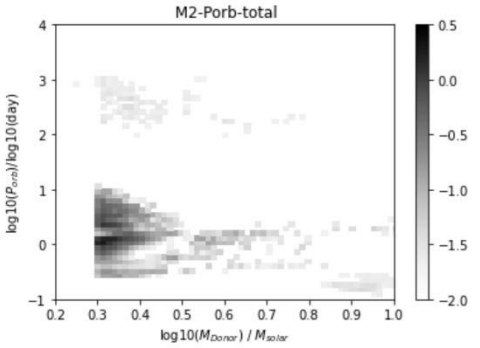

Figure 4. Same as Fig. 3, but for $M_2 - L_X$ plane.

ULXs harboring BH dominate. Galaxies younger than 20 Myr contributes a few because this requires strict condition for rapid formation of compact star. Duration of most young ULXs is usually short so that observation about these binaries is rare. The age of majority of ULXs is around $150Myr$ which indicates that ULXs are the tail evolution stage of HMXBs (Zuo et al. 2014). In our model, population increase after $200Myr$ is not obvious and beyond our consideration in this Ring galaxies case.

Fig. 3 depicts the numerical distribution of ULX with luminosity greater than $10^{39} erg{\cdot}s^{-1}$. The population of each element of this plot is calculated in the same way with XLF. It is seen that binaries with orbit periods shorter than ten days dominate, which corresponds with previous work (Shao & Li 2015). Obviously, the lower luminous region contains more ULXs, same with the differential XLF. Furthermore, detailed analysis indicated that the mass transfer mechanism of ULXs with shorter orbit periods tends to be RLOF while ULXs with WRL are systems with longer orbit period. The donor stars with WRL are more massive in Star-burst galaxies and shorter periods are unstable factor for constant mass transfer. Fig. 4 is the same with Fig. 3 but for $M_2 - L_X$ plane. Due to larger possibility in IMF, lower massive donor star comprise a large proportion. However, ULXs with WRL also contributes to this plot but mass span is large and distribution of each element is tiny. The observation BH ULX cases are rare, and their orbit parameters are difficult to be determined. Liu et al. (2013) has revealed M101 ULX-1 with a BH and a Wolf-Rayet star and confirmed the orbit period being 8.2 days. Later Titarchuk & Seifina (2016) analysed the spectral of M101 and estimated the BH mass on the order of $10^4 M_\odot$ which is an IMBH. We are unable to predict this BH in mass-orbit plane.

4

APPENDIX

4.1 Wind Accretion Efficiency

In the BHL model, the wind accretion efficiency is around 1.5%, which demands high mass transfer rate to form the ULX. The simulation result of wind Roche lobe overflow in HMXB (El Mellah et al. 2019) was adopted, which indicates the relation between accretion efficiency and feature of binaries. Slow acceleration($\beta = 2$) simulation is more realistic for accretion of ULXs due to its high accretion efficiency. In our model, fraction of wind captured is influenced by filling factor and speed ratio for BH and NS respectively. As only typical mass ratio for BII ($q = 2$) and NS ($q = 15$) was obtained via simulation, we assume a linear interpolation for other mass ratio. The typical fraction of wind captured $\mu_{\rm typical}$ is

$$\mu_{\rm typical} = \frac{q_{\rm typical} - q_{\rm NS}}{q_{\rm BH} - q_{\rm NS}} (\mu_{\rm BH} - \mu_{\rm NS}) + \mu_{\rm NS} \qquad (12)$$

where $q_{\rm typical}$ is the particular mass ratio. For other parameters, Nearest neighbor interpolation was performed for more reliable simulation.

4.2 Failure correction

In our statistical model, the summation of star forming probability ought to be equal to 100%. However, a set of particular situations are unrealistic. As a consequence, correction for SFR was implied.

Assuming that all the initial cases are permitted, the integral of probability is

$$\iiint M_1 \epsilon(m_1) \delta \ln M_1 k_q \delta q \dot{k}_a \delta \ln a = 1 \qquad (13)$$

When binaries failed to be generated in failure cases, the integral decrease. In order to normalize the total probability, a correction constant A was multiplied. $A\Sigma Success = A(1 - \Sigma Failure) = 1$

$$A = \frac{1}{1 - \Sigma Failure} \qquad (14)$$

After we performed the simulation and record the probability of Failure cases, A value was obtained via Eq.14. In our model, $A = 1.03$.

ACKNOWLEDGMENTS

This work is supported by the National Natural Science Foundation of China (grant Nos. 11573021, U1938104, 12003020) and the Fundamental Research Funds for the Central Universities.

REFERENCES

Abate C., Pols O. R., Izzard R. G., Mohamed S. S., de Mink S. E., 2013, A&A , 552, A26
Appleton P., Marston A., 1997, The Astronomical Journal, 113, 201
Bachetti M., Harrison F., Walton D. J., Grefenstette B., Chakrabarty D., Fürst F., Barret D., Beloborodov A., Boggs S., Christensen F. E., et al., 2014, Nature, 514, 202
Baker K., MacLaren S., Glendinning G., Seugling R., Whiting N., Source C., Fooks J., Fournier K., Biener M., Martinez D., Smalyuk V., Dittrich T., Moore A., Guymer T., 2013, in APS Division of Plasma Physics Meeting Abstracts Vol. 2013 of APS Meeting Abstracts, Optimizing 9-25 keV point projection 2D backlighters. p. PO7.009
Belczynski K., Kalogera V., Rasio F. A., Taam R. E., Zezas A., Bulik T., Maccarone T. J., Ivanova N., 2008, The Astrophysical Journal Supplement Series, 174, 223
Belczynski K., Ziolkowski J., 2009, The Astrophysical Journal, 707, 870
Blundell K. M., Bowler M. G., Schmidtobreick L., 2007, Astronomy & Astrophysics, 474, 903
Bondi H., Hoyle F., 1944, Monthly Notices of the Royal Astronomical Society, 104, 273
Edgar R., 2004, New Astronomy Reviews, 48, 843
Eggleton P. P., 1983, apj, 268, 368
El Mellah I., Sundqvist J., Keppens R., 2019, Astronomy & Astrophysics, 622, L3
Fürst F., Walton D., Heida M., Harrison F., Barret D., Brightman M., Fabian A., Middleton M., Pinto C., Rana V., et al., 2018, Astronomy & Astrophysics, 616, A186
Gao Y., Wang Q. D., Appleton P., Lucas R. A., 2003, The Astrophysical Journal Letters, 596, L171
Greene J. E., Strader J., Ho L. C., 2020, Annual Review of Astronomy and Astrophysics, 58, 257
Grimm H.-J., Gilfanov M., Sunyaev R., 2003, Monthly Notices of the Royal Astronomical Society, 339, 793
Hobbs G., Lorimer D., Lyne A., Kramer M., 2005, Monthly Notices of the Royal Astronomical Society, 360, 974
Hurley J. R., Tout C. A., Pols O. R., 2002, Monthly Notices of the Royal Astronomical Society, 329, 897
Jiang Y.-F., Stone J. M., Davis S. W., 2014, The Astrophysical Journal, 796, 106
Kaaret P., Feng H., Roberts T. P., 2017, ARAA , 55, 303
King A., 2008, Monthly Notices of the Royal Astronomical Society: Letters, 385, L113
King A., 2009, Monthly Notices of the Royal Astronomical Society: Letters, 393, L41
King A., Lasota J.-P., 2014, Monthly Notices of the Royal Astronomical Society: Letters, 444, L30
King A., Lasota J.-P., 2016, Monthly Notices of the Royal Astronomical Society: Letters, 458, L10
King A., Lasota J.-P., Kluźniak W., 2017, Monthly Notices of the Royal Astronomical Society: Letters, 468, L59
King A. R., Davies M. B., Ward M. J., Fabbiano G., Elvis M., 2001, The Astrophysical Journal, 552, L109
Kovlakas K., Zezas A., Andrews J. J., Basu-Zych A., Fragos T., Hornschemeier A., Lehmer B., Ptak A., 2020
Kroupa P., Tout C. A., Gilmore G., 1993, Monthly Notices of the Royal Astronomical Society, 262, 545
Kuranov A., Popov S., Postnov K., Volonteri M., Perna R., 2007, Monthly Notices of the Royal Astronomical Society, 377, 835
Lamers H. J., Snow T. P., Lindholm D. M., 1995, The Astrophysical Journal, 455, 269
Lasota J.-P., Vieira R., Sadowski A., Narayan R., Abramowicz M., 2016, Astronomy & Astrophysics, 587, A13
Liu J.-F., Bregman J. N., Bai Y., Justham S., Crowther P., 2013, Nature, 503, 500
Middleton M., Brightman M., Pintore F., Bachetti M., Fabian A., Fuerst F., Walton D., 2019, Monthly Notices of the Royal Astronomical Society, 486, 2
Middleton M. J., King A., 2017, Monthly Notices of the Royal Astronomical Society: Letters, 470, L69
Mineo S., Gilfanov M., Sunyaev R., 2012, Monthly Notices of the Royal Astronomical Society, 419, 2095
Mineo S., Rappaport S., Steinhorn B., Levine A., Gilfanov M., Pooley D., 2013, Astrophysical Journal, 771
Mohamed S., Podsiadlowski P., 2011, in Kerschbaum F., Lebzelter T., Wing R. F., eds, Why Galaxies Care about AGB Stars II: Shining Examples and Common Inhabitants Vol. 445 of Astronomical Society of the Pacific Conference Series, Wind Roche-Lobe Overflow: A New Mass Transfer Mode for Mira-type Binaries. p. 355
Ohsuga K., Mineshige S., 2011, The Astrophysical Journal, 736, 2
Poutanen J., Lipunova G., Fabrika S., Butkevich A. G., Abolmasov P., 2007, Monthly Notices of the Royal Astronomical Society, 377, 1187
Shakura N. I., Sunyaev R. A., 1973, Astronomy and Astrophysics, 24, 337
Shao Y., Li X. D., 2015, Astrophysical Journal, 802
Shao Y., Li X.-D., Dai Z.-G., 2019, ApJ , 886, 118
Swartz D. A., Soria R., Tennant A. F., Yukita M., 2011, Astrophysical Journal, 741
Titarchuk L., Seifina E., 2016, Astronomy & Astrophysics, 585, A94
Wang S., Qiu Y., Liu J., Bregman J. N., 2016, The Astrophysical Journal, 829, 20
Webbink R., 1984, The Astrophysical Journal, 277, 355
Webbink R. F., 2008, in , Short-Period Binary Stars: Observations, Analyses, and Results. Springer, pp 233–257
Wiktorowicz G., Lasota J.-P., Middleton M., Belczynski K., 2019a, The Astrophysical Journal, 875, 53
Wiktorowicz G., Lasota J.-P., Middleton M., Belczynski K., 2019b, The Astrophysical Journal, 875, 53
Wiktorowicz G., Sobolewska M., Lasota J.-P., Belczynski K., 2017, The Astrophysical Journal, 846, 17
Wolter A., Consolandi G., Longhetti M., Landoni M., Bianco A., 2018, Proceedings of the International Astronomical Union, 14, 297–306
Wolter A., Esposito P., Mapelli M., Pizzolato F., Ripamonti E., 2015, Monthly Notices of the Royal Astronomical Society, 448, 781
Wolter A., Fruscione A., Mapelli M., 2018a, The Astro-

physical Journal, 863, 43
Wolter A., Fruscione A., Mapelli M., 2018b, The Astrophysical Journal, 863, 43
Yungelson L., Livio M., Tutukov A., 1997, The Astrophysical Journal, 481, 127
Zuo Z.-Y., Li X.-D., 2014, Monthly Notices of the Royal Astronomical Society, 442, 1980
Zuo Z.-Y., Li X.-D., Gu Q.-S., 2014, Monthly Notices of the Royal Astronomical Society, 437, 1187
Zuo, Zhao-Yu Song, Hao-Tian Xue, Han-Chen 2021, A&A, 649, L2